

Andreas Pein

**Synthesis and Characterization of Materials
for Optoelectronic Devices**

zur Erlangung des akademischen Grades eines Doktors der
technischen Wissenschaften

erreicht an der

Technischen Universität Graz

Betreuer:

Assoc. Prof. DI Dr. Gregor Trimmel

Institut für Chemische Technologie von Materialien
Technische Universität Graz

2011

To my daughter,

Flora

I declare that I have authored this thesis independently, that I have not used other than the declared sources / resources, and that I have explicitly marked all material which has been quoted either literally or by content from the used sources.

Graz, April 12 th , 2011	
-------------------------------------	--

Abstract

The topic of this work is the synthesis and characterization of materials for optoelectronic devices. The emphasis was set to materials which are suitable for the use in hybrid solar cells. The active layer in these cells is based on a mixture of conductive polymers and semiconducting nanoparticles. This combination combines the advantages of organic solar cells with the tunable optoelectronic properties of inorganic nanoparticles.

The first three chapters deal essentially with conducting polymers. The focal points include the synthesis of polymers which increase the miscibility of the inorganic and the organic components, and thus counteract phase separation, which would lead to a deterioration of the achievable performance. Furthermore, polymers with suppressed crystallization tendency were synthesized. The last part is devoted to the effects of metal contamination, caused by the polymerization catalyst, on the efficiency of solar cells.

The main focus of the last two chapters was set on the synthesis of inorganic nanoparticles. The emphasis of the first was placed on a comparison between conventional oil bath heating and microwave heating in the synthesis of CuInS_2 nanoparticles. The last part of this work is concerned with the investigation of a hybrid material, consisting of a polymer with functional groups which are able to coordinate to both, ZnO nanoparticles and a cationic platinum complex. Due to the proximity of the latter materials, an energy transfer from the nanoparticles to the platinum dye is possible. Furthermore, the ability of this combination of materials to act as sensor for copper ions was investigated.

Kurzfassung

Das Thema dieser Arbeit ist die Herstellung und Charakterisierung von Materialien für optoelektronische Bauteile. Der Schwerpunkt liegt auf Materialien die für einen Einsatz in Hybridsolarzellen geeignet sind. Die aktive Schicht in derartigen Zellen besteht aus einer Mischung von leitfähigen Polymeren und anorganischen Nanopartikeln. Diese Kombination von Materialien verbindet die Vorteile von organischen Solarzellen mit den steuerbaren optoelektronischen Eigenschaften der anorganischen Halbleitermaterialien.

Die ersten drei Kapitel beschäftigen sich im Wesentlichen mit leitfähigen Polymeren. Die Themenschwerpunkte liegen dabei auf der Synthese von Polymeren die die Mischbarkeit der organischen und der anorganischen Komponente erhöhen und somit einer Phasenseparation, die eine Beeinträchtigung der erreichbaren Leistung zur Folge hat, entgegenwirken sollen. Weiters wurden gezielt Polymere mit unterdrückter Kristallisationsneigung synthetisiert. Der letzte Teil widmet sich den Auswirkungen von Metallverunreinigungen, verursacht durch den Polymerisationskatalysator, auf die Effizienz von Solarzellen.

Das Hauptaugenmerk der beiden letzten Kapitel richtet sich auf die Herstellung von anorganischen Nanopartikeln. Schwerpunkt des ersten ist ein Vergleich zwischen konventioneller Ölbadheizung und Mikrowellenheizung bei der Synthese von CuInS_2 Nanopartikeln. Der letzte Teil der Arbeit beschäftigt sich mit der Herstellung eines Hybridmaterials. Dieses besteht aus einem Polymer, das über funktionelle Gruppen sowohl ZnO Nanopartikel als auch einen kationischen Platinkomplex bindet. Durch die räumliche Nähe letztgenannter Materialien wird ein Energietransfer von den Nanopartikeln auf den Platinfarbstoff möglich, der Ziel der Untersuchungen ist. Weiters wird diese Materialkombination auf ihre Fähigkeit, als Sensormaterial für Kupferionen zu fungieren, untersucht.

Acknowledgements

The work during my PhD thesis was not only exciting from a scientific point of view but also because of all the interesting people that supported me either way. Therefore it is a pleasure for me to thank those who made this thesis possible. Particularly I wish to thank my supervisor Assoc. Prof. Gregor Trimmel for giving me the opportunity to work in this very interesting and important field of solar cells. I am especially grateful for his faith in my skills and for giving me the opportunity to pursue own ideas. His support and engagement has been very helpful during the whole time. I am grateful to all people at the Institute of Chemistry and Technology of Materials for the very pleasant working atmosphere and assistance. Especially, I would like to thank Dr. Thomas Rath and Dr. Eugen Maier for fruitful discussions and useful suggestions on endless occasions.

As scientific output is in most cases the consequence of team work, collaborations also contributed to a great extent to the success of this work. Therefore, I owe my gratitude to Prof. Robert Saf for performing MS measurements, Dr. Petra Kaschitz for NMR measurements, Ing. Josefine Hobisch for GPC and thermal analysis, and Christoph Kronawetter for logistic support. Moreover, I would like to thank Prof. Kappe and Dr. Mostafa Baghbanzadeh for their contributions in microwave assisted synthesis and Dr. Fabian Niedermair and Assoc.Prof. Christian Slugovc for providing materials and ideas helpful for the success of the last part of the thesis.

Financial support by the Austrian Science Fund (FWF) in the framework of the Austrian Nano-Initiative (Research project cluster – Performance Optimization of Polymer Nanocomposites NANOCOMP – research project: OPTELCOMP, as well as the Christian Doppler Laboratory for Nanocomposite Solar Cells, the Isovoltaic AG, the Polymer Competence Center Leoben, and the Federal Ministry of Economy, Family and Youth are gratefully acknowledged.

Last, but most of all, I owe my deepest gratitude to my family, who supported me from the very beginning. Especially I am grateful to my wife Romana, who was always a fix point of motivation and patience in hard times. Special thanks also go to my daughter Flora, for showing me how joyful and easy life can be.

Table of Contents

1	GENERAL INTRODUCTION AND MOTIVATION	11
1.1	A reason for nanocomposite solar cells.....	12
1.2	Nanocomposite Solar Cells	12
1.2.1	Principle Processes in Nanocomposite Solar Cells.....	13
1.2.2	Characteristic Parameters	17
1.3	Semiconductor Nanoparticles.....	20
1.4	Conjugated Polymers.....	23
1.5	Aim of the thesis.....	26
2	BLOCK-COPOLYMERS FOR THE USE IN HYBRID SOLAR CELLS	28
2.1	Introduction to Polythiophenes.....	30
2.1.1	Synthesis methods.....	31
2.1.1.1	Grignard Metathesis Polymerization (GRIM).....	31
2.1.1.2	McCullough - route	36
2.1.1.3	Rieke - route	37
2.2	Results and Discussion	37
2.2.1	Synthesis of Thiophene Monomers	37
2.2.2	Polymerization via Grignard Metathesis	38
2.2.2.1	Characterization.....	39
2.2.3	Synthesis of block copolymers using vinyl - terminated P3HT	44
2.2.4	Synthesis of block copolymers using allyl - terminated P3HT	46
2.2.5	Comblike block copolymers	50
2.2.5.1	Synthesis and characterization.....	51
2.2.5.2	Photophysical characterization of BC7 and BC8	55
2.3	Experimental.....	56
2.3.1	Materials and Methods.....	56

2.3.2	Syntheses procedures	57
2.3.2.1	Synthesis of the monomer	57
2.3.2.2	Polymerization using GRIM with vinylic end groups.....	58
2.3.2.3	Polymerization using GRIM with allylic end groups.....	60
2.3.2.4	Comblike block copolymers.....	61
3	POLY(9,9-DIOCTYLFLUORENE-CO-BITHIOPHENE) AND DERIVATES	65
3.1	Introduction	65
3.2	Synthesis by Suzuki Polycondensation	68
3.3	Results and Discussion	69
3.3.1	Synthesis	69
3.3.2	Characterization	71
3.3.3	DSC measurements.....	71
3.3.4	Photophysical characterization	73
3.3.5	Experimental.....	76
4	INFLUENCE OF RESIDUAL PALLADIUM IN F8T2.....	78
4.1	Introduction	78
4.1.1	Results and Discussion	81
4.1.1.1	Synthesis and purification	81
4.1.2	Fabrication of solar cells.....	82
4.1.3	Correlation between residual palladium and the trap density.....	87
4.2	Experimental.....	88
4.2.1	Materials	88
4.2.2	Device preparation.....	89
4.2.3	I-V curves	90
5	SYNTHESIS OF CUINS₂ NANOPARTICLES	91
5.1	Introduction	91
5.2	Results and Discussion	94

5.2.1	Study of the nanoparticle formation by WAXS.....	94
5.2.2	CuInS ₂ nanoparticle synthesis at 120°C	96
5.2.3	CuInS ₂ nanoparticle synthesis at 220°C	99
5.2.4	Comparison of oilbath and microwave heating for the CuInS ₂ nanoparticle generation under controlled reaction conditions	102
5.2.5	Experimental Section	107
5.2.5.1	Microwave Instrumentation.....	107
5.2.5.2	Synthesis of CuInS ₂ Nanoparticles.....	107
5.2.5.3	Characterization techniques.....	108
6	ENERGY TRANSFER	111
6.1	Introduction	111
6.2	Results and Discussion	113
6.2.1	Synthesis of the platinum dye.....	113
6.2.2	Synthesis of the Polyelectrolyte.....	113
6.2.3	Synthesis of ZnO nanoparticles	114
6.2.3.1	Characterization of ZnO nanoparticles.....	116
6.2.4	Photophysical characterization	117
6.2.4.1	Combination of platinum dye and block copolymer	117
6.2.4.2	ZnO nanoparticles and polyelectrolyte.....	121
6.2.4.3	ZnO nanoparticles and Pt-dye with copolymer	124
6.2.4.4	Influence of polymer concentration.....	131
6.2.4.5	Influence of KOH	133
6.3	ZnO nanoparticle based sensing of Cu(II)-ions	136
6.4	Experimental.....	142
6.4.1	Synthesis of ZnO nanoparticles	142
6.4.2	Characterization techniques	143
7	SUMMARY.....	144
8	SUMMARY.....	152
8.1	List of Tables	152

8.2	List of Figures.....	152
8.3	List of Publications.....	158
8.4	Curriculum Vitae	162

1 General Introduction and Motivation

The increasing world population as well as the industrialization of threshold countries increase the world's energy demand. This progression over the past years, the actual situation as well as predictions for the future is depicted in Figure 1. A great part of the consumed energy is generated from fossil fuels like oil, gas and coal. In contrast, the energy from renewable resources like solar, wind and geothermal energy play nowadays only a minor role. However, for the future the predictions are pointing towards a higher fraction of energy supplied by these resources.

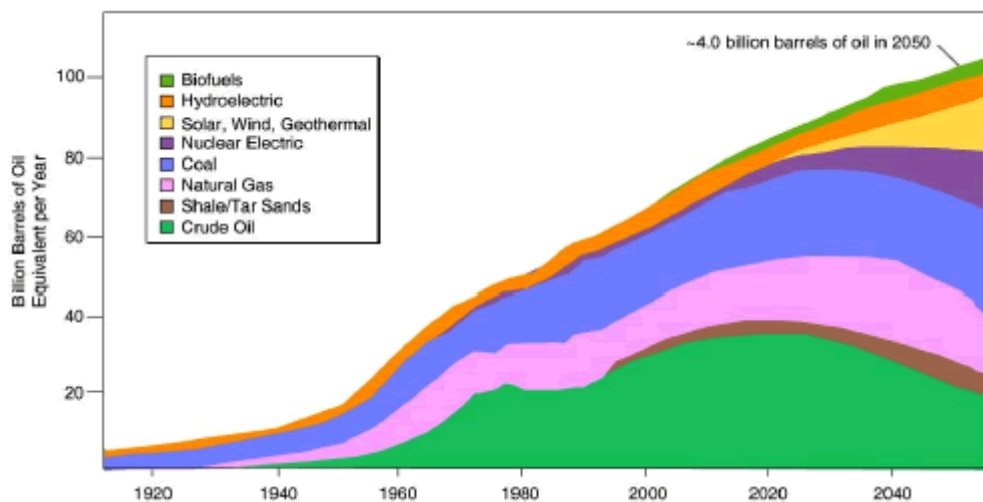


Figure 1. Overview of the world energy demand and prediction for the future.^[1]

This trend can be attributed to the fact, that fossil energy carriers get more and more expensive due to their depletion. Moreover, the releases of environmentally harmful substances like carbon dioxide, which acts as a greenhouse gas makes the establishment of alternatives advantageous. Especially the promotion of photovoltaics is necessary, when keeping in mind that the energy provided by the sun per year is in the order of $3 \cdot 10^{24}$ joules.^[2] This huge amount of energy is sufficient to fulfill the world energy demand for 10.000 years.

¹ Orr, L. Changing the World's Energy Systems, Stanford University Global Climate & Energy Project
² Grätzel, M. *Nature*, **2001**, 414, 338

1.1 *A reason for nanocomposite solar cells*

Currently, the photovoltaic market is dominated by classical silicon based technology. The advantages of this type of solar cells are the high efficiencies and the long-time stability. However, the production involves several expensive processing steps, which make the search for low - cost alternatives necessary.

From this point of view, organic solar cells or hybrid solar cells are very attractive due to the fact that they allow easy and cost-effective production technologies. It is believed that these types of cells can be based on plastic carriers and manufactured by cheap printing and coating techniques.^[3] A typical Si wafer production plant which produces wafers with 30 cm can produce an area of 88.000 m²/year. Compared to that in an average sized printing machine with 1-3 m/s the same area can be produced within hours.^[3] Moreover, as silicon is an indirect semiconductor, the layers have to be thicker than 100 µm in order to absorb efficiently photons. In contrast to that the thickness of organic solar cells is in the order of 200 nanometer or even less. This corresponds to a factor of 500 in the film thickness. From that point of view it is obvious that organic solar cells are economically attractive. Other advantages are the flexible and semitransparent nature of the cells. However, the well-known disadvantages are the comparably low efficiencies and the long-time stability. But nevertheless, by keeping in mind that this is a relative new sector of research and efficiencies of up to 8.13%^[4] have already been reached in organic photovoltaic cells it is appropriate to be optimistic for the future of this emerging technology.

1.2 *Nanocomposite Solar Cells*

In nanocomposite solar cells a donor material, which is typically a conjugated polymer is in intimate contact with an acceptor material. In organic nanocomposite solar cells this acceptor material is in most cases PCBM. The advantages of PCBM are the high mobility, the excellent miscibility with the polymer phase in common organic solvents, the ability to take up multiple negative charges and the ultrafast photoinduced electron transfer from conjugated polymers.^[5] The combination of P3HT and PCBM is probably

³ Brabec, C.J. *Solar Energy Materials & Solar Cells* **2004**, 83, 273

⁴ <http://solar-energy-news-and-views.blogspot.com/2010/07/solarmer-energy-reaches-world-record.html> (6.April 2011)

⁵ Cheng, Y.-J.; Yang, S.-H.; Hsu, C.-S. *Chem.Rev.* **2009**, 109, 5868

the most researched material combination in organic photovoltaics. In hybrid solar cells, PCBM is replaced by inorganic nanoparticles which also contribute to the absorption of light.

1.2.1 Principle Processes in Nanocomposite Solar Cells

The conversion of photons to photocurrent involves several fundamental processes, which will be discussed briefly in the next section. These processes are summarized in Figure 2. The first is the absorption of light to create an exciton. Excitons are electron – hole pairs which are bound together through electrostatic interaction. The incoming photon must have an energy exceeding the band gap of the absorbing material in order to promote one electron from the highest occupied molecular orbital (HOMO) to the lowest unoccupied molecular orbital (LUMO). In hybrid solar cells, which consist of a conductive polymer as the donor material and inorganic nanoparticles as the acceptor material, this process can occur either in the organic or the inorganic phase. This is one of the main advantages of hybrid solar cells because the absorption of the material combination can be chosen in a way that the parts of the solar spectrum with the highest photon flux densities can be covered.

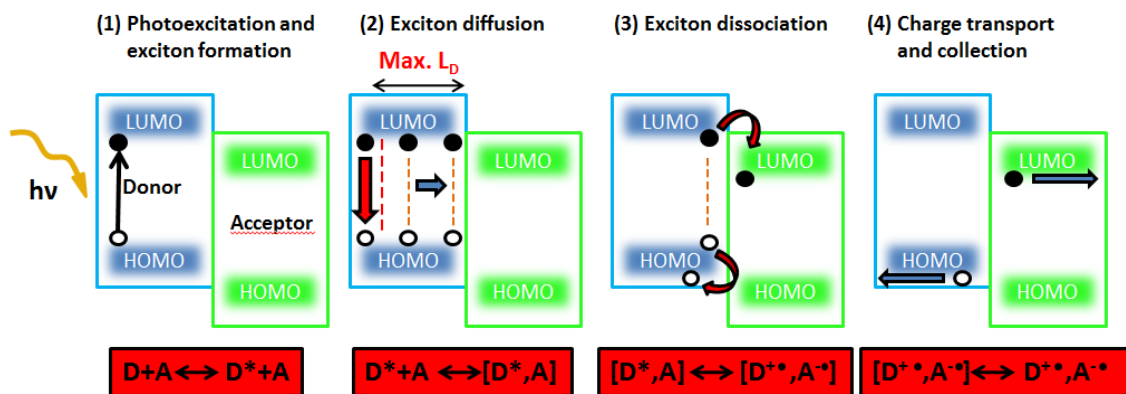


Figure 2. Principle processes involved in the generation of photocurrent.^[5](red blocks: D is the donor material, A is the acceptor material)

The photon flux of the sun under atmospheric conditions in northern Europe (AM 1.5) as a function of the wavelength is depicted in Figure 3. On the right y-axis the integrated photon flux and the corresponding maximum current density in a solar cell,

by assuming 100% conversion, are shown. The highest photon flux is found at 1.77 eV, corresponding to a wavelength of 700 nm.^[6] This implies that materials used for the fabrication of solar cells ideally have a large absorption coefficient in this area. This graph can also be used to assess the current density of absorber materials. For example, poly(3-hexylthiophene), a common used polymer in solar cells, has a band gap of 1.9 eV. This corresponds to a wavelength of 650 nm. The integration of the photon flux from 280 nm to 650 nm shows that this polymer is able to absorb only 22.4% of the total amount of the emitted photons from the sun. In terms of current density the material is limited to 14.3 mA/cm². However, this calculation does not take into account that also the acceptor material can contribute to the absorption of light. The main information provided by Figure 3 is the need for materials which absorb in the region of higher wavelengths, although one has to keep in mind that narrowing of the band gap can result in a reduction of the power conversion efficiency, by a reduction of the open circuit voltage. An optimal band gap of 1.4 eV was predicted by the detailed balance limit, introduced by Shockley and Queisser^[7]. Synthesis strategies for low band-gap polymers will be discussed separately in chapter 1.4.

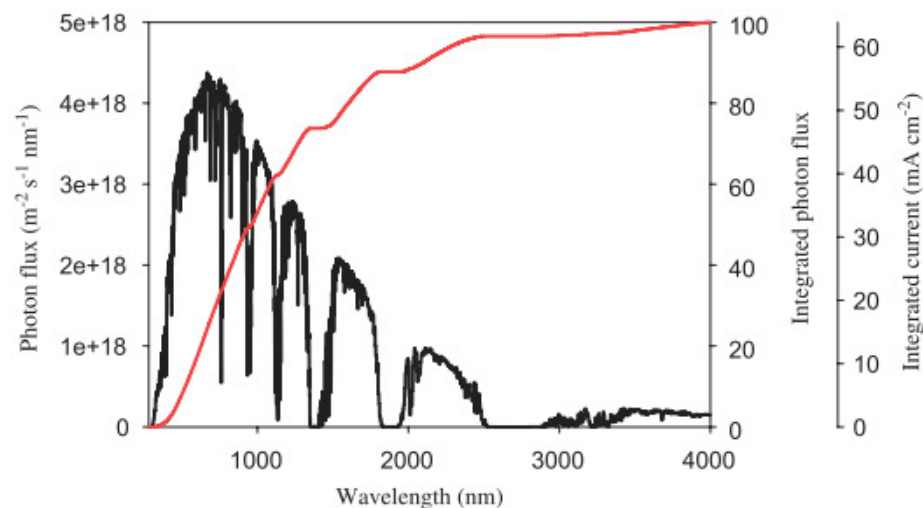


Figure 3. Photon flux of the sun (AM 1.5) as a function of the wavelength. The integrated photon flux is shown on the right y-axis together with the maximum obtainable current densities.^[8]

⁶ Reiss, P.; Couderc, E.; Girolamo, J.; Pron, A. *Nanoscale*, **2011**, 3, 446

⁷ Shockley, W.; Queisser, H.J. *J.Appl.Phys.* **1961**, 32, 510

⁸ Bundgaard, E.; Krebs, F.C. *Solar Energy Materials & Solar Cells* **2007**, 91, 954

The next crucial point concerning the absorption is the thickness of the active layer. Typical values are in the range between 100 and 300 nm. This rather thin active layer has the disadvantage that not all photons are absorbed. However, the formation of thicker active layers can give rise to other problems which are mainly caused by the limited mobility of charge carriers in the active layer. This implies that thicker layers are only useful in the case of materials which provide high mobility values. Otherwise, more photons are absorbed, but the corresponding charge carriers will not reach the electrodes and therefore do not contribute to the current density.

After the creation of excitons by the absorption of light, they have to diffuse to the donor/acceptor interface (Figure 2 (2)). The driving force for the transport of excitons is diffusion in the case that no external field is applied and drift-diffusion by applying an external field. However, excitons have a limited lifetime due to radiative or non-radiative decays. This limited lifetime translates into a certain distance an exciton is able to diffuse before it recombines. Typical values are in the order of some nanometers up to 10 nanometers. These lengths depend strongly on the nature of the polymer. For P3HT as example, the mean exciton diffusion length is greatly influenced by the regioregularity of the connected monomer units. The concept of regioregularity will be separately discussed in chapter 2. P3HT with 92% regioregular couplings leads to diffusion lengths of 2.6-5.3 nm, whereas a degree of regioregularity of 98.5% lead to 8.5 nm.^[9,10] This difference can be explained by a higher degree of crystallinity, achieved with regioregular polymer chains, resulting in lamella-like polymer domains with higher mobility, compared to their amorphous counterpart which are obtained from polymers with poor regioregularity.^[11] However, as was impressively shown by Huang and coworkers, too big polymer domains can have a negative effect on the overall solar cell performance.^[12] This can be attributed to the fact that excitons created in the center of polymer aggregates, which exceed the double size of the exciton diffusion length do not contribute to photocurrent generation due to recombination. The size of the aggregates can be influenced by the annealing temperature, by the used solvent and the method of film formation.

⁹ Kroeze, J.E.; Savenije, T.J.; Vermeulen, M.J.W.; Warmann, J.M. *J.Phys.Chem.B*, **2003**, 107, 7696

¹⁰ Shaw, P.E.; Ruseckas, A.; Samuel, I.D.W.; *Adv.Mater.* **2008**, 20, 3516

¹¹ Hallermann, M.; Kriegl, I.; Da Como, E.; Berger, J.M.; von Hauff, E.; Feldmann, J. *Adv.Funct.Mater.* **2009**, 19, 3662

¹² Huang, J.-H.; Yang, C.-Y.; Ho, Z.-Y.; Kekuda, D.; Wu, M.-C.; Chien, F.-C.; Chen, P.; Chu, C.-W.; Ho, K.-C. *Organic Electronics*, **2009**, 10, 27

The next step in the production of photocurrent is the dissociation of the excitons at the interface (Figure 2 (3)) based on the energetically different LUMO levels of the donor and the acceptor. Most literature reports agree that a minimum offset of 0.3 eV should be provided in order to effectively separate the charges.^[13,14] It is clear that in order to ensure efficient separation of the charges, the contact area of the donor and the acceptor material has to be as big as possible. This is one of the main advantages for the use of nanoparticles which provide a large surface in the organic matrix due to their high surface to volume ratio. Moreover, this point explains the advantage of the bulk heterojunction architecture compared to the bilayer strategy (see Figure 4). To explain shortly, in bilayer solar cells, first a layer of the donor material is deposited on the substrate, followed by a second layer which contains the acceptor material. In this type of cells the contact area is very limited. Moreover, as shown in Figure 4, absorption processes, occurring in a distance from the interface, which exceeds the exciton diffusion length do not contribute to the photocurrent generation.

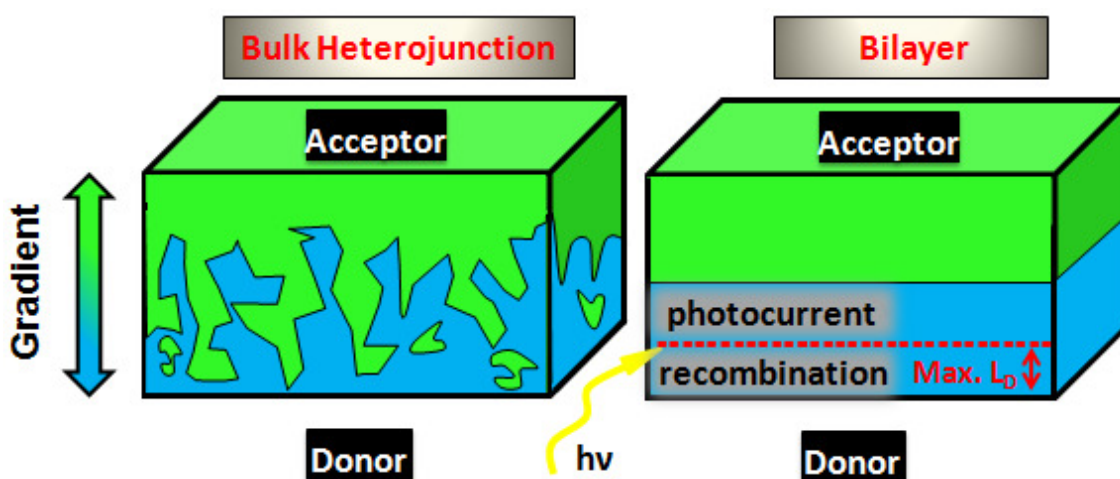


Figure 4. Schematic illustration of bulk heterojunction (showing a gradient) and bilayer architecture.

However, based on the simplified morphology of this type of cells their use is an advantage for theoretical studies. In contrast to that, bulk heterojunction solar cells consist of one active layer, which comprises both types of materials. Therefore an

¹³ Brabec, C.J.; Winder, C.; Sariciftci, N.S.; Hummelen, J.C.; Dhanabalan, A.; van Hal, R.A.; Janssen, R.A.J. *Adv.Funct.Mater.* **2002**, 12, 709

¹⁴ Winder, C.; Matt, G.; Hummelen, J.C.; Janssen, R.A.J.; Sariciftci, N.S.; Brabec, C.J. *Thin Solid Films* **2002**, 403, 373

intimate contact is possible. The drawback of this concept is that by optimization of the production parameters the phase separation of the donor and the acceptor has to be controlled in a way which leads ideally to a bicontinuous network.

Once the charges are separated, they have to be transported to the corresponding electrodes, typically low work function metals like aluminum or calcium. This can only be achieved if continuous pathways are present. This implies that charges which are generated at isolated islands cannot contribute to the photocurrent generation. Moreover, also the recombination of charge carriers can provide a reason for the loss of efficiency. This point will be separately discussed in Chapter 4.

1.2.2 Characteristic Parameters

The characteristic parameters of the solar cell are the short circuit current (I_{SC} , [mA/cm²]), the open circuit voltage (V_{OC} , [V]) the fill factor (FF, [%]) and the power conversion efficiency (PCE, [%]). These parameters can be extracted from current-voltage plots in the dark and under illumination (see Figure 5).

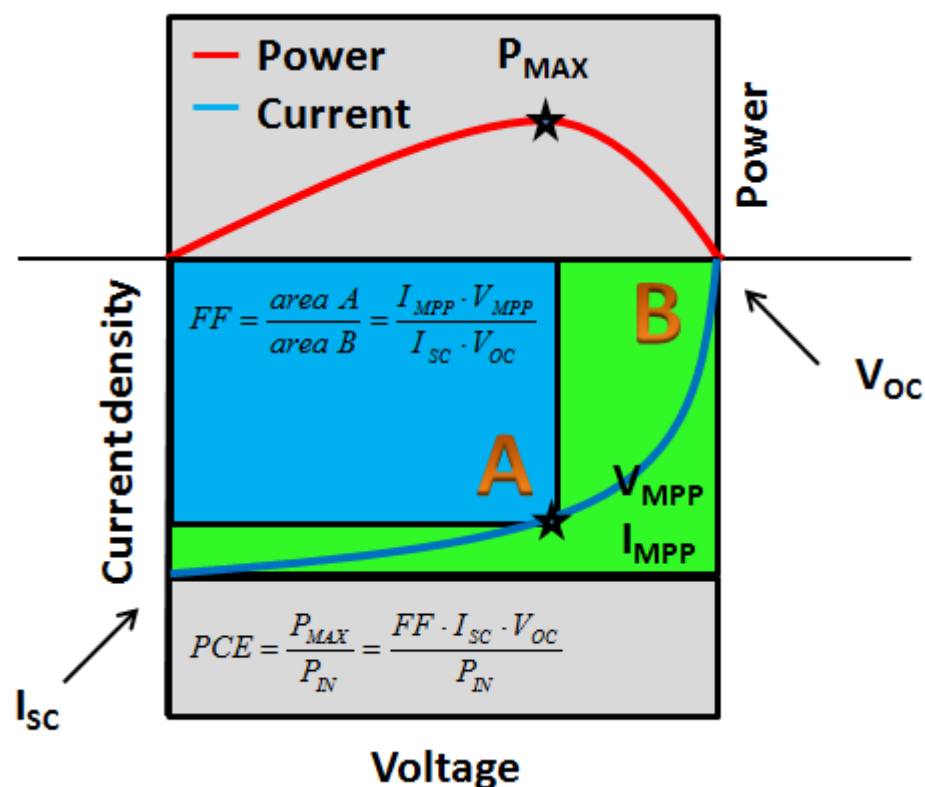


Figure 5. Current – voltage characteristic of a solar cell.^[5]

To measure the I_{SC} of the cell no voltage is applied. This implies that the value can be seen from the intercept of the illuminated curve with the y-axis. As mentioned before, this value is mainly influenced by the absorption properties of the components (mainly governed by the band gap, E_g in Figure 6), the quality of the charge separation and the transport behavior to the electrodes. Concerning the combination of donor and acceptor a sufficient LUMO offset has to be ensured (depicted as E_d in Figure 6). The V_{OC} is measured if no current is flowing through the cell. This value can be seen at the intercept of the illuminated curve with the x-axis. It mainly depends on the energetic difference of the LUMO of the acceptor and the HOMO of the donor (V_{BI} in Figure 6) and is also often called “effective band-gap”.

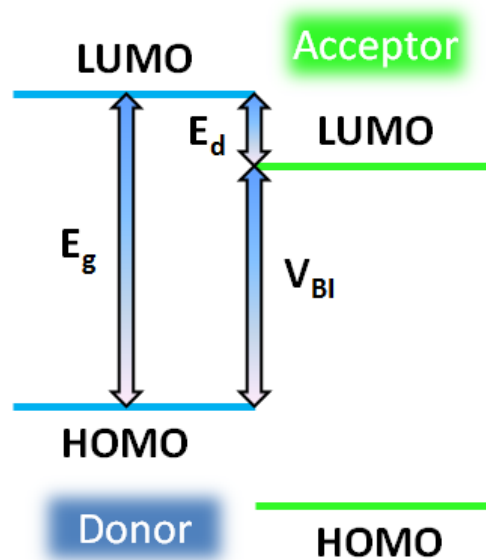


Figure 6. Energy diagram of a donor and acceptor material and the corresponding parameters.

In principle a solar cell can be operated between $V=0$ and $V=V_{OC}$. The corresponding current densities at these levels are $I=I_{SC}$ and $I=0$. As the electrical power is defined as the product of voltage and current, there is a certain point where this product reaches a maximum. This point is called the maximum power point (P_{MAX}), with I_{MPP} and V_{MPP} as the corresponding values of the current density and voltage at this point. Per definition the power output of a solar cell is defined as the power at the maximum power point under an illumination intensity of 100 mW/cm^2 at a temperature of 25°C .^[15]

¹⁵ Köthe, H. K. *Stromversorgung mit Solarzellen* 1993 Franzis-Verlag

The next parameter which is useful to describe the quality of solar cells is the fill factor (FF), which is defined as follows

$$FF = \frac{I_{MPP} \cdot V_{MPP}}{I_{SC} \cdot V_{OC}} \quad (1)$$

In an ideal solar cell this value would approach 100%. This means that P_{MAX} is given by the product of V_{OC} and I_{SC} . In real devices, however, the curve under illumination is not an ideal rectangle but depending on the quality of the investigated cell. This real-life behavior of solar cells can be understood by the equivalent circuit of a cell (Figure 7). In the dark a solar cell exhibits diode characteristics. Under illumination the circuit can be described by a diode with a current source, originating from the produced photocurrent, in parallel with the junction. In real devices this equivalent circuit has to be modified by the implementation of a series resistance (R_S) and a shunt resistance (R_{SH}).

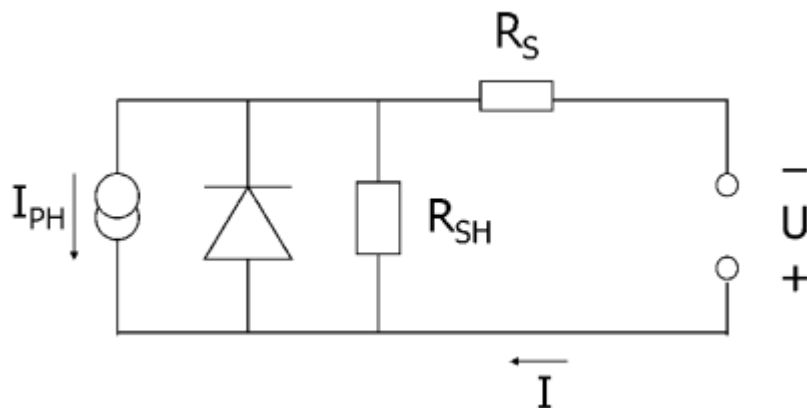


Figure 7. Equivalent circuit of a solar cell.^[16]

This leads to the following formula which describes the I-V characteristics of photovoltaic devices

$$I = I_0 \cdot \left(\exp\left(\frac{e}{nkT}(U - IR_S)\right) - 1 \right) + \frac{U - IR_S}{R_{SH}} - I_{PH} \quad (2)$$

where I_0 is the dark current, e the elementary charge, n the diode ideality factor, k the Boltzmann constant, T the temperature, U the applied voltage, R_S the series resistance, R_{SH} the shunt resistance, and I_{PH} is the photocurrent.^[16] To get high fill factors certain

¹⁶ Hoppe, H.; Sariciftci, N.S. *J.Mater.Res.* **2004**, 19, 1924

conditions have to be fulfilled. Firstly, the shunt resistance has to be very large in order to prevent leakage currents. Secondly, the series resistance is low, in order to get a steep rise in the forward current. The physical meaning of the series resistance is the sum of all sorts of resistances in the cell, beginning from bulk transport resistance, interface transfer and from the transport of currents through the contacts.^[16] The last important parameter of solar cells is the efficiency which is defined as follows

$$\eta = \frac{V_{oc} \cdot I_{sc} \cdot FF}{P_{IN}} \cdot 100\% \quad (3)$$

This parameter describes the productivity of solar cells.

1.3 *Semiconductor Nanoparticles*

Semiconductor nanoparticles are an interesting class of materials. This can be attributed to the fact, that the energy gap which separates the conduction from the valence band is a function of the nanoparticle size, in contrast to their bulk analogues. This effect is also known as the quantum size effect, and applies for nanoparticle sizes smaller than 10 nm. Of course, this is only a general value, and depends on certain material properties. The quantum size effect is interesting because it allows, through a variation of the nanoparticle size a precise tuning of the optical properties. A simple approximation to quantify this effect is the “quantum box”.^[17] The formula predicts a size related contribution to the energy gap:

$$E_g(QD) \approx E_{g,0} + \frac{\hbar^2 \pi^2}{2m_{eh} R^2} \quad (4)$$

In this formula $E_g(QD)$ is the band gap of the quantum dot (other name for nanoparticles in the quantum size effect regime), $E_{g,0}$ is the band gap of the bulk material, \hbar is the reduced Planck constant, $m_{eh} = m_e m_h / (m_e + m_h)$ where m_e and m_h are the effective masses of electrons and holes, respectively, and R is the radius of the spherical particle. This formula predicts a blue shift of the emission with decreasing quantum dot size. Beside this increasing energy gap, the quantum confinement leads to discrete atom-like energy levels. Generally, the boundaries between molecules, quantum dots and the bulk

¹⁷ Klimov, V. *Semiconductor and Metal Nanocrystals*; Marcel Dekker Inc.; New York; 2004

materials are not precisely defined, but as rule of thumb between ~100 and ~10.000 atoms per particle can be assumed as size regime for quantum dots.

A general overview of the used synthesis methods is given in chapter 5.1. In the following paragraph some general remarks concerning the colloidal chemical synthesis are given.

In general, the synthesis of nanoparticles can be divided in two stages. The first is the nucleation of primary crystallites and the second is the growth of the nanoparticles. The kinetics of the nucleation is difficult to study,^[18] whereas several models which describe the growth of nanoparticles exist. One widely accepted model was proposed by La Mer and Dinegar.^[19] According to them two different cases of growth, shown in Figure 8, can be considered. The first uses a high concentration of the monomer species and the second a low monomer concentration. The left side of the curve with high monomer concentration shows a negative growth, which means dissolution of the particles under a certain size. This size is also known as the critical size. This parameter is mainly governed by the concentration of the active monomer in solution and follows the trend that high monomer concentrations lead to small primary crystallites. After the nucleation event, the particles grow fast in the initial stage of the reaction indicated by the steep slope of the red curve in Figure 8. After a certain period of time, a maximum in the growth rate can be observed. This can be attributed mainly to geometric considerations, which means that, with increasing volume of the particles more monomer units have to be incorporated to induce the same increase in radius. These considerations have a dramatic influence on the size distribution of the nanoparticles. As smaller particles grow faster than the bigger ones, a focusing in the size is obtained. With prolonged reaction times the concentration of the active monomer decreases which results in a continuous shift of the critical size towards bigger particles. The consequence of this fact is known as Ostwald ripening. This process can be described as the growth of big nanoparticles at the expense of smaller ones. In terms of size distribution this event has to be prevented because it leads to a broadening. This can be achieved by quenching of the reaction at shorter reaction times or the addition of monomer during the synthesis which keeps the monomer concentration at a high value.

¹⁸ Peng, X.; Wickham, J.; Alivisatos, A.P. *J.Am.Chem.Soc.* **1998**, 120, 5343

¹⁹ La Mer, V.K.; Dinegar, R.H. *J.Am.Chem.Soc.* **1950**, 72, 4847

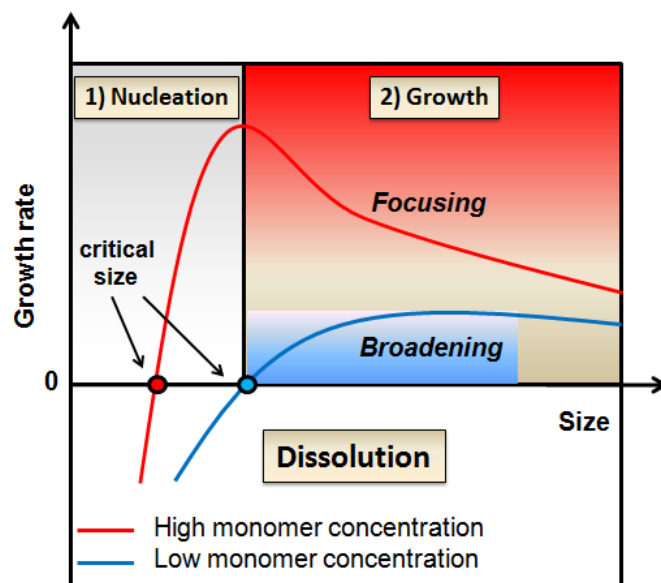


Figure 8. Kinetic considerations during the growth of nanoparticles.^[20]

However, one has to keep in mind that by adding more monomers the concentration of the active species must not reach a certain limit to ensure that a second nucleation burst of particles is avoided. Contrary, low monomer concentrations lead to a broadening of the particle size distribution.

This implies that by assuring a nucleation event occurring only during a short period of time and by using high monomer concentrations it is possible to obtain particles with a narrow size distribution. For the use in hybrid solar cells this is an important issue because it guarantees defined optoelectronic properties.

Due to their high surface to volume ratio, nanocrystalline quantum dots (NQD) are not stable and tend to form aggregates in order to minimize their surface. This would lead to poorly defined materials. To avoid this phenomenon, organic molecules, able to coordinate to the nanoparticle surface, are used during the synthesis. These molecules, also called cappers, consist of two parts. The first one is an electron donor moiety, which is able to coordinate to electron poor metal atoms on the surface and the second part is a long alkyl chain which assures the steric repulsion of two neighboring particles. For the synthesis of nanoparticles in aqueous media the tendency to agglomerate can also be prevented by molecules with ionic groups which lead to a steric repulsion of the particles. Moreover, by the coordination the optical properties of the particles are

²⁰ Yin, Y.; Alivisatos, A.P. *Nature* **2005**, 437, 664

optimized by the surface passivation. The surface of nanoparticles is covered to a certain degree with so called trap states. These are locations on the surface where dangling bonds or other irregularities cause energy levels located between the valence and the conduction band. Trap states lead to poor emission quantum yields due to competing recombination processes. One further important factor which can be controlled by the right choice of the cappers is their ability to influence the nucleation and growth of the particles during the synthesis. In general there are several factors concerning the capper which influence the progression of nanoparticles growth. These are the coordination strength, the ratio of capper to monomer and the steric bulk of the capper. Concerning the coordination strength loosely coordinated molecules ensure high growth rates. However, a certain limit of coordination tendency has to be ensured in order to prevent agglomeration. Higher ratios of capper to monomer lead in general to smaller particles. Cappers with highly steric demanding groups decrease the growth rate of the nanoparticles by decreasing the diffusion of active monomer species to the surface. Up to now no general strategies are known concerning these factors which allow precise use of certain molecules in the synthesis of nanoparticles. This implies that the choice of the right reaction parameters as well as the choice of the reagents is in most cases a question of the operator's know-how.

However, for the incorporation of nanoparticles in solar cells the capping molecules have several disadvantages. General strategies to get rid of the capping sphere are described in chapter 2.

1.4 Conjugated Polymers

Conductive polymers are extensively investigated since the early works of Shirakawa and co-workers in 1977.^[21] They were able to show that by doping of trans-polyacetylene conductivities of up to 10^3 S/cm are possible. Since then many different types of conductive polymers were investigated due to the many advantages of using polymers in electronic devices. They are light weight, flexible, resistant against corrosion processes and offer cheap and easy to handle processing methods.^[22]

²¹ Shirakawa, H.; Louis, E.J.; MacDiarmid, A.G.; Chiang, C.K.; Heeger, A.J. *J.Chem.Soc.Chem.Comm.* **1977**, 578

²² Malhotra, B.D. *Handbook of Polymers in Electronics* **2002**, Rapra Technology Limited, Shawbury

As already mentioned there is still a need for the preparation of low band gap polymers which efficiently harvest photons. In the following section some general strategies in the synthesis of low band gap polymers are explained.

The skeleton of polyaromatic conjugated polymers can be seen as an alternation of double and single bonds. For such a system two resonance structures with nondegenerate energy levels exist. The first is the aromatic resonance structure which is energetically favored. In this structure the electrons are confined to the aromatic units of the polymer. In the second resonance structure the π -electrons are delocalized over the conjugated system. This structure is called the quinoid resonance structure, which is energetically less favored due to the loss of aromatic resonance stabilization energy. By adopting this structure the band gap of the polymer decreases. The ratio of aromatic to quinoid resonance structure can be correlated to the bond length alternation (BLA). BLA is defined as the average of the difference in length between adjacent carbon-carbon bonds in a polyene chain.^[5] Polymers with units which favor the aromatic resonance structure in the ground state have large BLA-values. It is clear that polymers, consisting of units with high aromatic resonance stabilization energy prefer the aromatic form, resulting in large band gaps. This can be clearly seen in polyphenylene which exhibits a band gap of 3.2 eV. Another factor which is responsible for this rather high value is the steric demand of the hydrogen atoms on the aromatic units, causing a twisting of the rings which also leads to an increased band gap. By diluting the aromatic system with double bonds, as in poly(phenylenevinylene) the band gap decreases to a value of 2.4 eV. But in general the use of other aromatic systems with lower resonance stabilization energy, like in thiophenes, is more often applied. This results in a band gap of 1.9 eV in polythiophenes.

The next factor which influences the band gap of a polymer is the planarization of the backbone. The degree of electron delocalization between neighboring aromatic units is dependent on the relative angle between these units. This is due to the fact that the overlap of the p_z orbitals is more effective when they are parallel to each other. The resulting delocalization leads to a decrease in the BLA and a reduction of the band gap. This strategy was confirmed in a series of polymers introduced by Roncali.^[23,24,25] Two

²³ Brisset, H.; Thobie-Gautier, C.; Gorgues, A.; Jubault, M.; Roncali, J. *J. Chem. Soc., Chem. Commun.* **1994**, 1305

²⁴ Orti, E.; Sanchis, M. J.; Viruela, P. M.; Vituela, R. *Synth. Met.* **1999**, 101, 602

²⁵ Roncali, J.; Thobie-Gautier, C. *Adv. Mater.* **1994**, 6, 846.

of these polymers are shown in Figure 9. The polymer on the left side consists of two thiophene rings which are rigidified and bridged by the sp^3 carbon of a ketal group.^[5] This leads to a low band gap of 1.2 eV. The polymer on the right side uses the same strategy with the difference that the planarization is extended over three thiophene units which results in an even lower band gap of 1.1 eV.

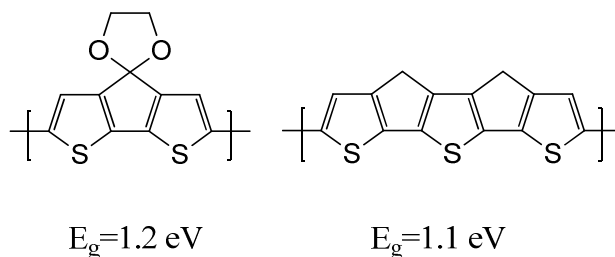


Figure 9. Polymers with increased planarization.^[23,24,25]

The HOMO and LUMO levels can also be shifted by the incorporation of electron donating or withdrawing substituents. In general, the HOMO energy level is raised by electron-donating groups and the LUMO energy level is lowered by electron-withdrawing substituents. A common polymer which uses this effect is poly[3,4.(ethylenedioxy)thiophene] (PEDOT), with a band gap of 1.5 eV. The chemical structure is shown in Figure 10.

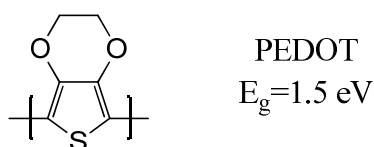


Figure 10. Chemical structure of PEDOT.

The most common method in decreasing the band gap is the intramolecular charge transfer. This strategy will be separately discussed in chapter 3.1.

1.5 Aim of the thesis

This work deals with the synthesis and characterization of materials which can be used in optoelectronic devices.

In chapter 2 block copolymers, designed to improve the interaction of the inorganic and the organic phase in hybrid solar cells, are described. Normally, due to the different solubility of these materials, phase separation occurs on the microscopic level. However, to maximize the current density of photovoltaic devices an interpenetrating network of the donor and the acceptor phase has to be ensured. This aim should be achieved by the use of block copolymers. These consist of two blocks. The first is able to coordinate to the surface of the inorganic nanoparticles and the second consists of a conjugated polymer. In principle, these macromolecules should be able to effectively passivate trap states of nanoparticles which are located on the surface. Moreover the coordination of these polymers should prevent nanoparticles from agglomeration. The electroactive block situated, due to the inherent structure, near the surface of the particles should provide efficient dissociation. So, these molecules are suitable to enhance the miscibility of inorganic nanoparticles with conjugated polymers.

The aim of the work described in chapter 3 deals with the synthesis and characterization of F8T2 and derivatives. The side chains in the derivatives were modified in a way which should reduce the crystallinity of the resulting polymers. This was done to increase the content of the amorphous polymer phase. Although amorphous phases have the disadvantage of low mobility, the continuous path through the active layer is relative independent on the preparation conditions, and the formation of bulky polymer clusters is avoided.

In chapter 4 the purity of polymers, used for the fabrication of solar cells was investigated. While most of the work deals with the intrinsic parameters of polymers, like the molecular weight and the PDI, the attention was focused on the influence of residual palladium, introduced by the catalyst of the polymerization, on the performance of solar cells.

In chapter 5 the synthesis of CuInS₂ nanoparticles, using CuI, InCl₃, and elemental sulfur as precursors and oleylamine as solvent and capping agent, was investigated. The

attention of the work was focused on a comparison of microwave irradiation and classical oilbath heating as heating mechanism of the reaction. This investigation was of special interest because of the numerous advantages of this heating method, like short reaction times and easy controllable heating profiles. Moreover, the influence of microwave irradiation on the final shape and size of nanoparticles is controversially discussed in the literature.

In chapter 6 the interaction of ZnO nanoparticles with an amphiphilic block copolymer, bearing platinum excimers, was investigated. The acid functionalities located on the polymer act here as the functionality which enables simultaneous coordination of the dyes and the particles. The conducted investigations mainly deal with an energy transfer process which takes place due to an overlap of the nanoparticle emission and the absorption of the dyes. A model, describing the overall process was worked out and confirmed by different experiments. The second part deals with possible applications as sensitive material combination regarding the detection of Cu^{2+} ions.

2 Block-Copolymers for the use in hybrid solar cells

Nanocomposites consisting of semiconducting nanoparticles in a matrix of an electroactive polymer gained a lot of interest in recent years due to the promising properties relevant to the production of photovoltaic devices. This material combination offers easy and non-expensive processing methods like spin-coating and doctor blading techniques. The materials are cheap and provide a large variety of possible modifications. One main challenge in producing nanocomposites is the miscibility of the organic and the inorganic phase. The use of nanoparticles with bulky cappers on the surface often leads to a phase separation on the micrometer scale.^[26] This can be attributed to the tendency of nanoparticles with capping molecules like oleic acid, stearic acid and long-chained amines to form densely packed agglomerates.^[27] Additionally the polymers which tend to form semicrystalline domains, means crystalline domains which are separated by amorphous areas, contribute to this problem.^[28] The second big disadvantage, if using nanoparticles with bulky substituents, is the suppressed charge transport between the donor and the acceptor because of the isolating properties of the capping molecule.

Several strategies to overcome these problems have been applied. The first is to replace the bulky substituents by small, labile ligands. This procedure was first introduced by Greenham et al..^[29] Trioctylphosphineoxide (TOPO) ligands were replaced by pyridine. This small molecule is at least partially removed during the film formation. This results in only poor capped nanoparticles which are stabilized by the polymer matrix. The second approach is to use capping molecules which are per se conductive. This strategy can be followed by using oligomers with anchoring groups^[30], suitable for the coordination, but also appropriate functionalized polymers can be used. Regarding functionalized polymers the anchor group can be introduced at the chain end or in the side chains. For high molecular weight polymers the introduction in the side chain is

²⁶ Holder, E.; Tessler, N.; Rogach, A.L. *J.Mater.Chem.* **2008**, 18, 1064

²⁷ Murray, C.B.; Kagan, C.R.; Bawendi, M.G. *Annu.Rev.Mater.Sci.* **2000**, 30, 545

²⁸ Brinkmann, M.; Wittmann, J.C. *Adv.Mater.* **2006**, 18, 860

²⁹ Greenham, N.C.; Peng, X.G.; Alivisatos, A.P. *Phys.Rev.B* **1996**, 54, 17628

³⁰ Aldakov, D.; Querner, C.; Keervella, Y.; Jusselme, R.; Demadrille, R.; Rossitto, E.; Reiss, P.; Pron, A. *Microchim. Acta* **2008**, 160, 335

more suitable as the ratio of end groups to monomers decreases with increasing chain length. This would drastically reduce the number of available anchor functions. Most of the literature reports deal with functionalized polythiophenes as polymer. This is due to the fact that thiophenes offer a rich chemistry which enables different modifications, allowing coordination to nanoparticle surfaces. Examples of end - functionalized polythiophenes include polythiophenes functionalized with thiol^[31], phosphonic acid^[32] and amino^[33] groups. Wang et al. followed an alternative strategy, where the coordination to the particles is provided by groups in the side chains. For this reason they synthesized comb-like, graft copolymers with polythiophene building the main chain and poly(*N,N*-dimethylaminoethyl methacrylate) side chains.^[34] Mixing this polymer with CdSe nanoparticles resulted in an effective nanoscale dispersion of the particles in the polymer matrix. However, one drawback of this approach is that the charge transfer from the polymer to the nanoparticles is highly dependent on the chain length of the side chains. In general, long side chains lead to a too large distance of the particles to the conjugated backbone which results in hindered charge transfer properties.

In this work two alternative strategies were pursued. The first is to synthesize a block copolymer, consisting of a conductive polythiophene block and a second block with anchor groups which lead to an efficient coordination to the surface of nanoparticles.

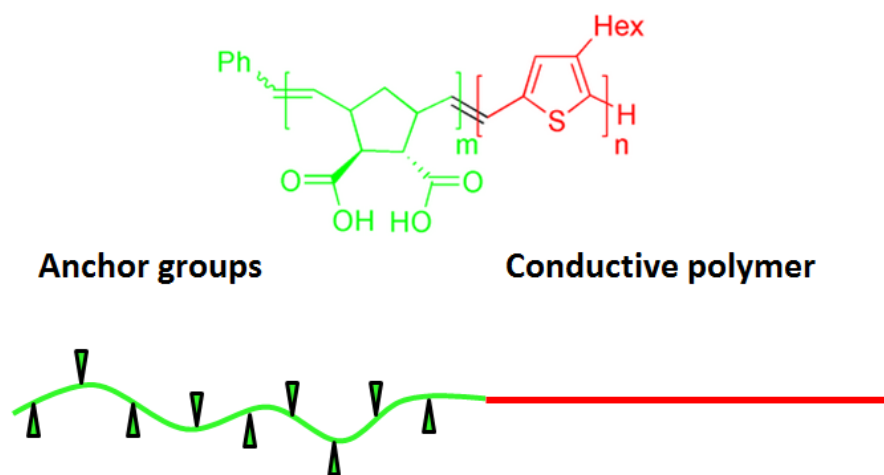


Figure 11. Strategy 1 for the coupling of nanoparticles to a conductive block.

³¹ Sih, B.C.; Wolf, M.O. *J.Phys.Chem.C* **2007**, 111, 17184

³² Milliron, D.J.; Alivisatos, A.P.; Pitois, C.; Edder, C.; Frechet, J.M.J. *Adv.Mater.* **2003**, 15, 58

³³ Liu, J.; Tanaka, T.; Sivula, K.; Alivisatos, A. P.; Frechet, J. M. J. *J. Am. Chem. Soc.* **2004**, 126 (21), 6550–6551.

³⁴ Wang, M.F.; Kumar, S.; Coombs, N.; Scholes, G.D.; Winnik, M.A. *Macromol.Chem.Phys.* **2010**, 211, 393

The second strategy was to synthesize oligothiophenes which were incorporated in the side chain of a polynorbornene block. The copolymerization with a second block, suitable for the coordination to nanoparticles leads to the desired macromolecule.

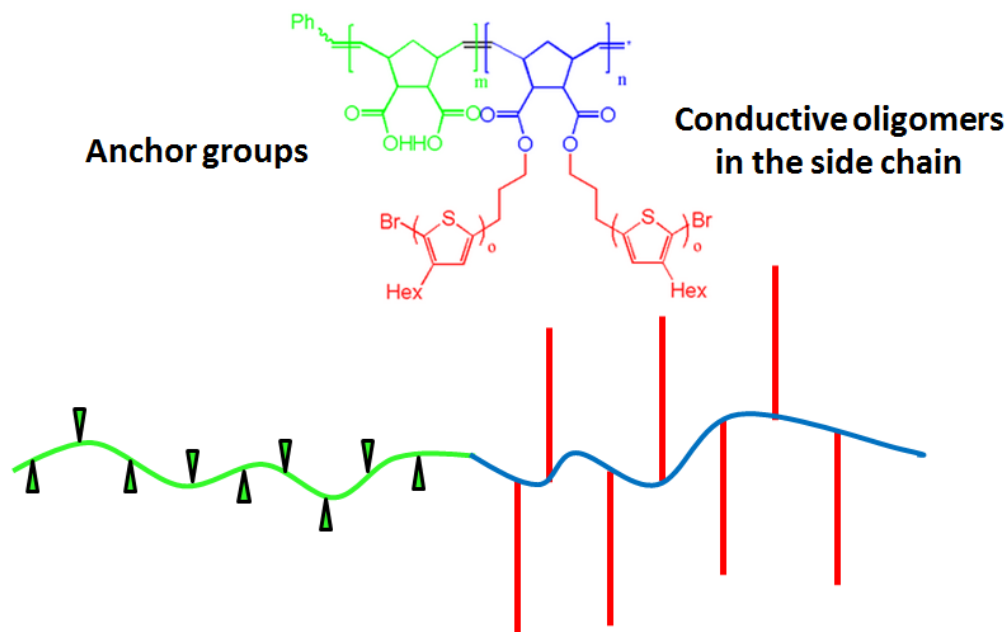


Figure 12. Strategy 2 for the coupling of nanoparticles to a conductive block.

2.1 Introduction to Polythiophenes

Polythiophenes are one of the most researched conductive polymers. The disadvantage of this polymer is the hindered processability due to poor solubility. This drawback can be overcome by introducing alkyl substituents in position 3 of the aromatic ring. These poly-3-alkylthiophenes (P3ATs) are of scientific interest based on the possible applications in various fields including thin film transistors^[35] or photovoltaic cells.^[36] The incorporation of asymmetric substituted monomers into a polymer chain leads to different possible coupling products.

³⁵ Katz, H.E. *J.Mater.Chem.* **1997**, 7, 369

³⁶ Gur, I.; Fromer, N. A.; Alivisatos, A. P. *J.Phys.Chem.B.* **2006**, 110, 25543

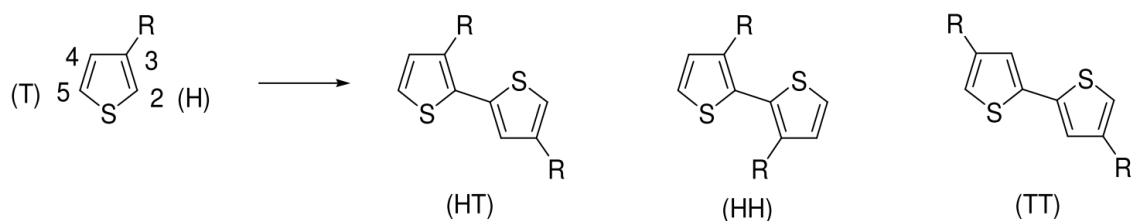


Figure 13. Possible coupling products of substituted thiophene.

As shown in Figure 13 the thiophene monomer with a substituent in position 3 of the aromatic ring can form three different dimers. A bond between the carbon atoms 2 and 5' leads to the HT dimer, 2,2' forms the HH dimer and finally coupling of 5 and 5' leads to the TT dimer. In terms of conductivity HT coupling is superior compared to the others because only in this arrangement of the side chains the twisting of the polymer backbone, caused by the steric hindrance of the side chains, is suppressed. The planar backbone leads to efficient overlap of the π -orbitals and therefore the effective conjugation length of the polymer is increased. The percentage of HT coupling varies strongly with the synthesis method, as discussed in chapter 2.1.1.1. Moreover, only polymers with a high degree of regioregularity are able to crystallize in the solid state. This aspect will be briefly discussed in chapter 2.1.1.1.

2.1.1 Synthesis methods

In the following chapter only the synthesis methods which lead to a high fraction of regular coupling will be discussed. Nevertheless, there are of course other methods like the oxidative polymerization with FeCl_3 ^[37], or the electrochemical synthesis^[38], which lead to irregular coupling of the monomer units.

2.1.1.1 Grignard Metathesis Polymerization (GRIM)

The Grignard Metathesis Polymerization is one of the state of the art synthesis methods for substituted thiophenes and was also used for the preparation of the polymers in this work. Therefore, the fundamental principles will be explained in more detail. There are several advantages of this method compared to other often used procedures, which will be discussed shortly in the next chapter. First of all, GRIM is a living polymerization

³⁷ Sugimoto, R.; Takeda, S.; Gu, H.B.; Yoshino, K. *Chem. Express* **1986**, 1, 635

³⁸ Hotta, S. *Synthetic Metals* **1987**, 22, 103

which proceeds in contrast to most other polycondensation reactions via a chain growth mechanism and not, as was assumed for some time, via step growth mechanism.^[39] One of the main advantages of living polymerizations is that the desired molecular weight can easily be adjusted by the right molar ratio of monomer to catalyst. Controlling the molecular weight distribution of polymers is another crucial point in polymer synthesis and is characterized by the polydispersity index (PDI) of the polymer. In general, living polymerization methods are in terms of low PDI values superior compared to other methods. Of course this statement is also true for the GRIM, with PDIs, typically smaller than 1.5. However, another possibility of improving the molecular weight distribution is the so called solvent-extraction method that was introduced by Trznadel et al.^[40] This method takes advantage of the fact that the solubility of P3HT decreases with increasing molecular weight in solvents of low polarity index. For this reason an easy separation of fractions with different molecular weight can be made by successive Soxhlet extraction of the precipitated polymer with solvents of increasing polarity. In this work this method was applied by using hexane and chloroform as solvents.

Furthermore, since termination reactions are absent, block copolymers can be synthesized just by adding a second comonomer. After the consumption of the first monomer, the absence of termination reactions also allows the controlled introduction of various end groups, as will be discussed in the following chapter.

One further advantage of this method is that cryogenic temperatures are not needed. The reaction proceeds at room temperature or even at slightly elevated temperatures.

As mentioned before, since substituted polythiophenes are mainly important for optoelectronic applications, the conductivity of the polymers is of great interest. By using GRIM head to tail coupling values of >98% are obtained. This does not only increase the effective conjugation length of the polymer chains but also provides the basis for crystalline polymer structures as was shown by McCullough et al. using X-ray studies of thin films.^[41] This high regioregularity yields polymers with conductivity values of around 1000 S/cm (typical values are between 100 and 500 S/cm). Compared to around 20 S/cm, obtained by polymers produced by methods on the basis of a radical mechanism, the advantage of this method is apparent.

³⁹ Sheina, E.E.; Liu, J.; Iovu, M.C.; Laird, D.W.; McCullough, R.D. *Macromolecules* **2004**, *37*, 3526

⁴⁰ Trznadel, M.; Pron, A.; Zagorska, M.; Chrzaszcz, R.; Pielichowski, J.; *Macromolecules* **1998**, *31*, 5051

⁴¹ McCullough, R.D.; Ewbank, P.C., in *Handbook of Conducting Polymers 2nd ed.*, (Eds: Skotheim, T.; Elsenbaumer, R.L., Reynolds, J.R.) Marcel Dekker, New York **1998**

The polymerization procedure involves several steps. First, a reaction with *tert*-BuMgBr in THF (abs.) with 2,5-dibromo-3-alkylthiophene yields the corresponding Grignard compound via metal-halogen exchange. The driving force for this reaction is the better stabilization of the magnesium next to an aromatic ring compared to the aliphatic *tert*-butyl group due to hyperconjugation.

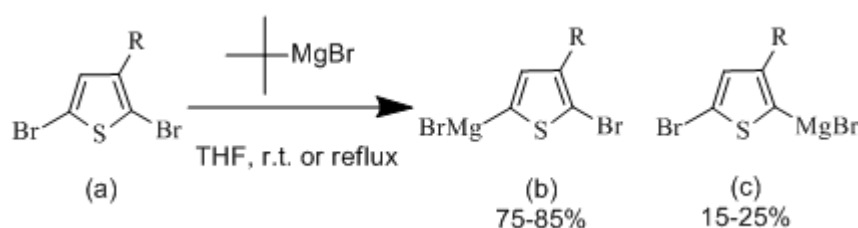


Figure 14. Possible products from the reaction of **a** with the Grignard reagent.

Further incorporation of a second magnesium is highly suppressed based on the electropositive character of the metal.^[42] As will be discussed later it is crucial to use exactly one equivalent of the Grignard species. As shown in Figure 14 this reaction is not regiospecific. But compound **b** is formed in excess due to the bulky *tert*-butyl group which favors position 5 on the aromatic ring based on steric arguments. Polymerization of this mixture with Ni(dppp)Cl₂ leads to polymers with 99% head to tail coupling. Although this fact is not fully understood kinetic and competitive studies showed that a head to head coupling between **b** and **c** is unlikely because this would lead to a twisted, and therefore energetic unfavorable, transition state during the reductive elimination.^[43] So all following coupling reactions are head to tail.

The mechanism of the polymerization is depicted in Figure 15. To start the chain, two mono-Grignard thiophenes react with Ni(dppp)Cl₂ to the corresponding compound **d**. Reductive elimination of the catalyst produces the first couple of thiophenes. These first units are irregularly coupled, namely in tail to tail position. Especially, if low molecular weight polymers are produced, this irregular coupling can be observed in ¹H - NMR spectra as will be discussed later on. This irregularity at the beginning of the growing chain cannot be avoided, but however by approaching the high molecular weight regime the influence of the first unit can be neglected. The bithiophene unit forms an associated

⁴² Knochel, P., Dohle, W., Gommermann, N., Kneisel, F. F., Kopp, F., Korn, T., Sapountzis, I., Vu, V. A. *Angew. Chem.*, **2003**, *115*, 4438-4456

⁴³ Loewe, R. S., Ewbank, P. C., Liu, J., Zhai, L., McCullough, R. D. *Macromolecules*, **2001**, *34*, 4324-4333

pair with the Ni-catalyst (**e+f**) which is of importance because this ensures that each catalyst molecule gives rise to only one growing polymer chain. The oxidative addition in the next step is the beginning of the catalytic cycle, consisting of (1) oxidative addition, (2) metathesis reaction with new, incoming monomer, and finally (3) reductive elimination of the catalyst.^[39]

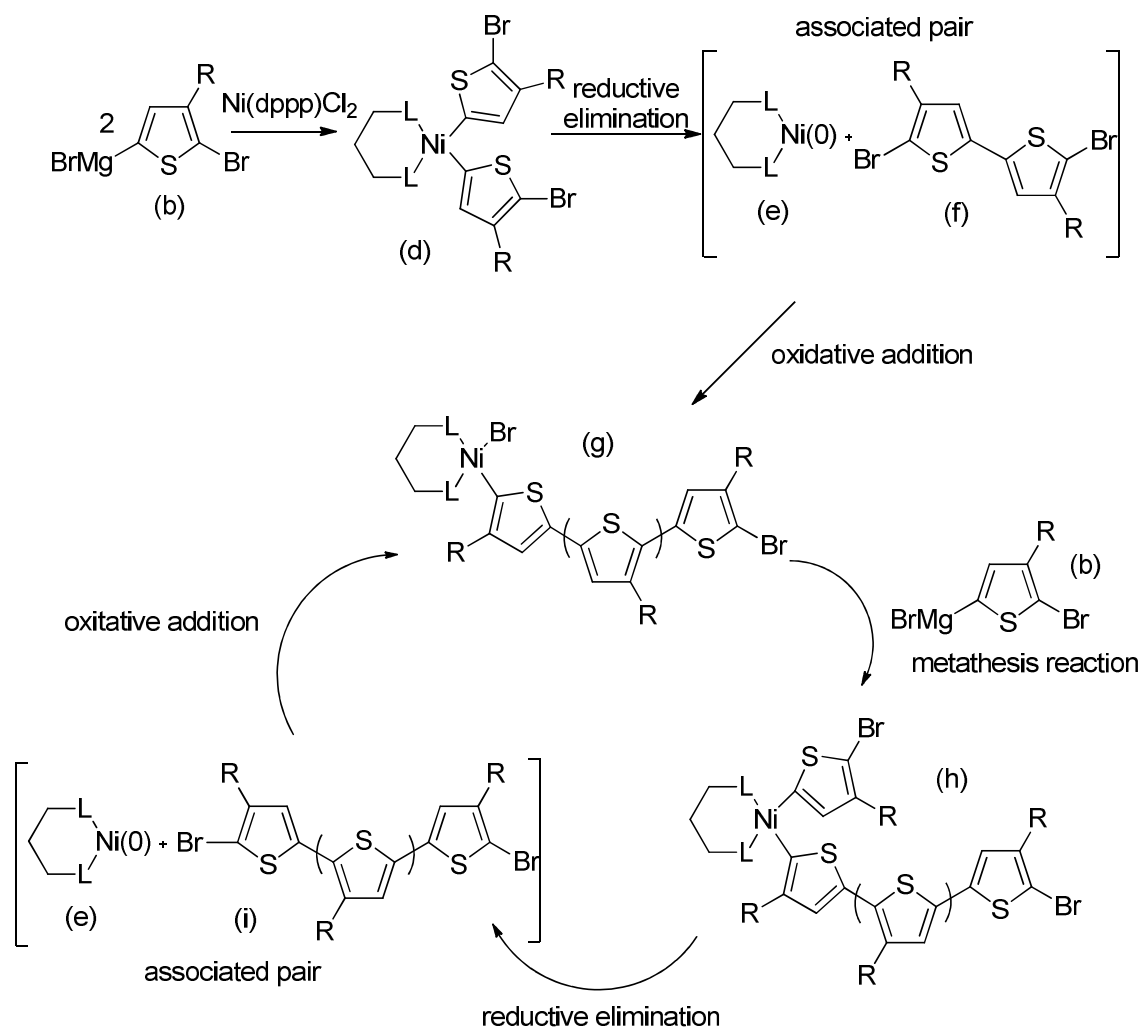


Figure 15. Mechanism of the polymerization.

2.1.1.1.1 Functionalization of the end group

As mentioned before the absence of termination reactions allows the introduction of various end groups on the polymer chain. This is a very interesting topic because end group modification gives rise to many further adjustments. For example end groups can

act as a starting point for the polymerization of a second block by other polymerization methods like atom transfer radical polymerization (ATRP)^[44], reversible addition fragmentation chain transfer polymerization (RAFT)^[45] or nitroxide mediated polymerization (NMP)^[45]. Well defined block copolymers combining the properties of different materials can easily be obtained in this way. Another possible application is the introduction of groups which can specifically react with certain surfaces. The group of Frechet for example modified P3HT with an amine end group which was then used to coordinate to CdSe nanoparticle surfaces. This hybrid material was used to fabricate solar cells with efficiencies of around 1.4%.^[33]

After complete consumption of the monomer, the catalyst is still inserted between the thiophene at the chain end and the bromine atom **j**. The addition of the end-capping Grignard reagent in large excess yields the corresponding polymer **l** with the end group R'.

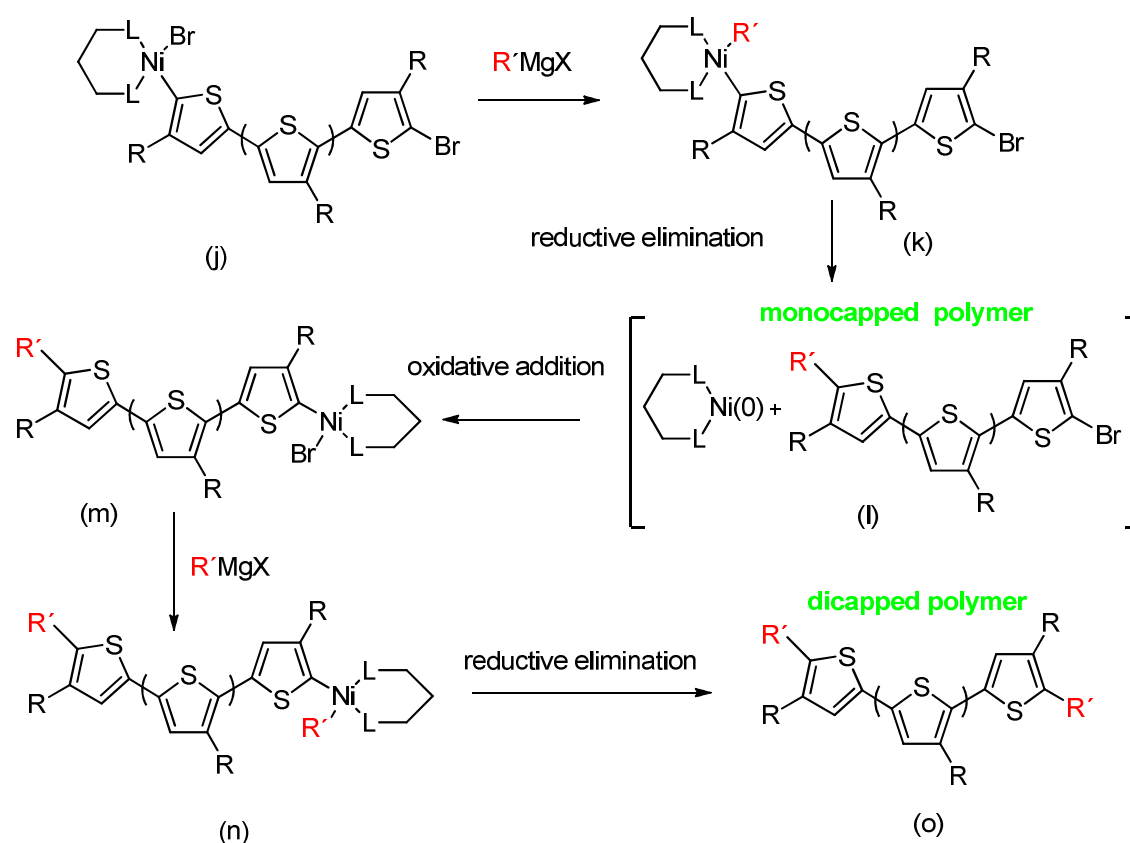


Figure 16. Schematic reaction scheme of the end group-functionalization.

⁴⁴ Liu, J.; Sheina, E.; Kowalewski, T.; McCullough, R.D. *Angew.Chem.Int.Ed.* 2002, 41, 329

⁴⁵ Iovu, M.C.; Craley, R.; Jeffries-EL, M.; Krankowski, A.B.; Zhang, R.; Kowalewski, T.; McCullough, R.D. *Macromolecules* 2007, 40, 4733

Depending on the nature of this end group the reaction stops at this point or goes further to yield a polymer, functionalized at both chain ends. It was observed by McCullough et al.^[46] that end groups containing a π -electron system like alkenes, alkynes or aromatic compounds mainly give the mono-capped compound whereas alkanes give the di-capped polymers. These results were explained by the tendency of Ni(0) compounds to coordinate to electron rich groups. This implies that the catalyst stays coordinated to the first chain end if the end group bears an electron rich moiety. Contrary, using Grignard reagents with saturated compounds make the oxidative addition on the other chain end possible, yielding the di-capped polymers **o**.

2.1.1.2 McCullough - route

In 1992 McCullough and coworkers^[47] were the first who were successful in synthesizing regioregular poly(3-alkylthiophenes). The fundament of their success was the regiospecific formation of (5-bromo-4-hexylthiophen-2-yl)magnesium bromide by a selective lithiation of 2-bromo-3-hexylthiophen in position 5 (see Figure 17).

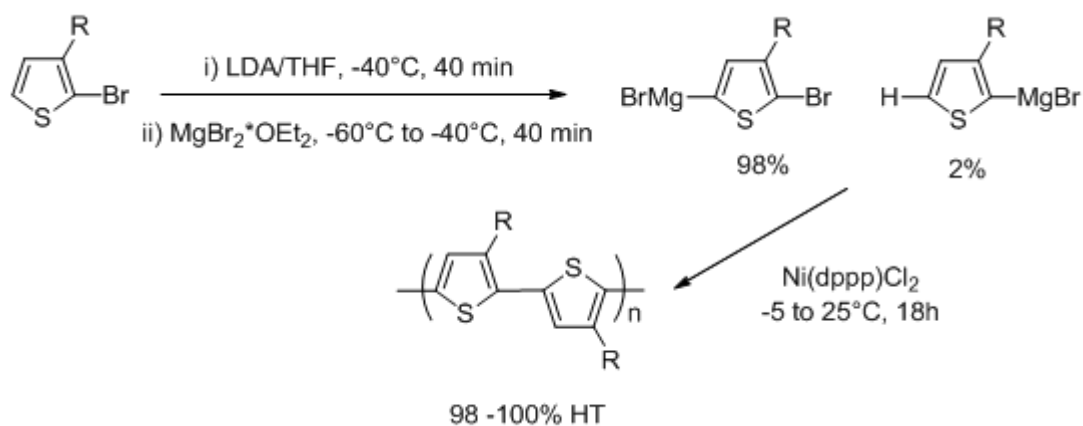


Figure 17. Synthesis of P3AT according to McCullough.

The following transmetalation leads to the desired product with 98% yield. The subsequent polymerization with Ni(dppp)Cl₂ yields P3AT, consisting of 98-100% of regular coupled monomer units.

⁴⁶ Jeffries-EL, M., Sauvé, G., McCullough, R. D. *Advanced Materials*, **2004**, *16*, 1017-1019

⁴⁷ Osaka, I., McCullough, R. D. *Accounts of Chemical Research*, **2008**, *41*, 1202

2.1.1.3 Rieke - route

The polymerization method developed by Rieke and coworkers^[48] uses 2,5-dibromo-3-alkylthiophene as monomer. The oxidative addition of Rieke zinc (Zn^*) affords the desired 2-bromo-5-(bromozincio)-3-alkylthiophene with only minor traces of the second regioisomer. The relative ratio of the two regioisomers strongly depends on the used reaction parameters. In general, temperatures as low as $-78^\circ C$ lead to higher selectivities. Also the length of the alkyl chain plays a role where a trend of increased selectivity with longer alkyl chains was observed.

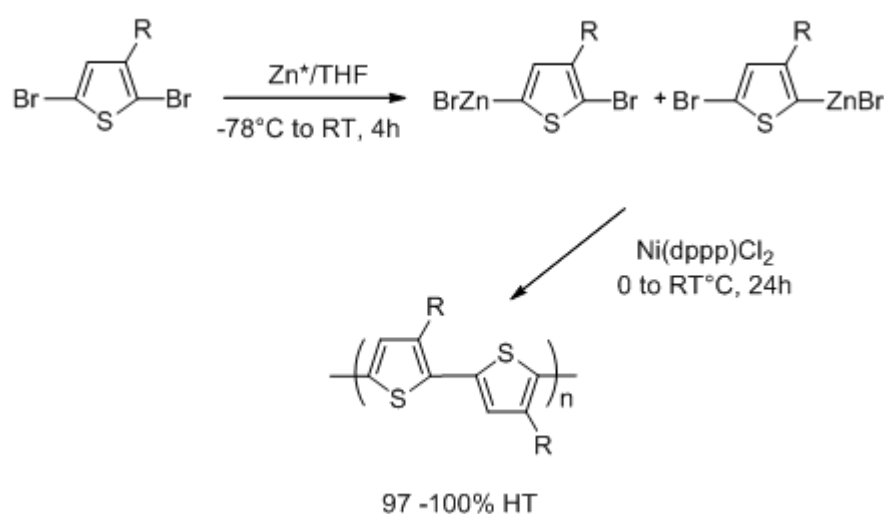


Figure 18. Synthesis of P3HT according to Rieke.

The advantage of this method compared to the McCullough route is that organozinc compounds are known for their high tolerance towards functional groups, opening the possibility of synthesizing polymers with many different functionalities.

2.2 Results and Discussion

2.2.1 Synthesis of Thiophene Monomers

To obtain 2,5-dibromo-3-hexylthiophene (**2**), 3-hexylthiophene (**1**) was brominated with *N*-bromosuccinimide (NBS) according to a literature protocol. To the educt 2 equivalents of NBS were added in small portions at room temperature in absolute THF

⁴⁸ Chen, T.-A.; Wu, X.; Rieke, R.D. *J.Am.Chem.Soc.* **1995**, 117, 233

as solvent. The progress of the reaction was investigated by thin layer chromatography (TLC) with cyclohexane as eluent. The reaction was stirred at room temperature overnight. At this stage the monomer was completely absent but two products were formed, the mono and the dibrominated 3-hexylthiophene. After evaporation of the solvent in vacuum, n-heptane was added to precipitate the excess of NBS. After filtration, evaporation in vacuum yielded a brownish solution which was purified by distillation under vacuum. The yield of the reaction was 84%. The introduction of the two bromine atoms was confirmed by NMR measurements.

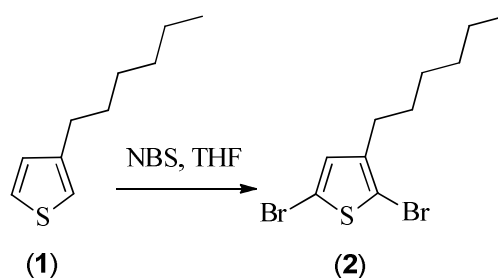


Figure 19. Reaction scheme of the bromination of 3-hexylthiophene.

2.2.2 Polymerization via Grignard Metathesis

The general reaction scheme of the polymerization via GRIM is depicted in Figure 20. As mentioned in chapter 2.1.1.1 the polymerization involves several steps. The first is the addition of *tert*-BuMgBr. The purity of the product is highly dependent on the conditions of this step.

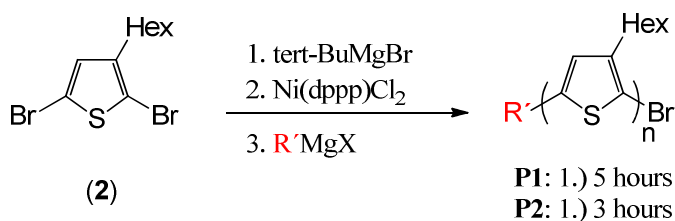


Figure 20. Reaction scheme of the polymerization.

In the first experiments different reaction times with *tert*-BuMgBr, which was added to 2,5-dibromo-3-hexylthiophene (2) in THF (abs.) were applied. For polymer **P1**, 5 hours at 50°C were used and for **P2** only 3 hours. After cooling the reaction mixture to room temperature, the catalyst, dissolved in THF was added. The reaction mixture was then stirred for 10 minutes at room temperature, followed by adding vinylmagnesium

bromide via syringe to the reaction mixture. After stirring for further 2 minutes the reaction mixture was poured into methanol to precipitate the polymer.

2.2.2.1 Characterization

To characterize the two obtained polymers different methods of characterization were used. First, the interpretation of the nuclear magnetic resonance (NMR) spectra will be discussed. In a 100% regioregular P3HT only one aromatic signal, attributable to the proton at position 4 on the aromatic ring centered around 6.98 ppm should be observable. As was explained in chapter 2.1.1.1, 100% regular coupled P3HT cannot be obtained due to the fact that the coupling reaction of the first two monomers is always tail to tail. The chemical shifts corresponding to the various possible couplings in polythiophenes are listed in Table 1.^[49]

Table 1. Chemical shift of the possible coupling products in polythiophenes with chloroform as solvent.

configuration	chemical shift δ [ppm]
HT-HT	6.98
TT-HT	7.00
HT-HH	7.02
TT-HH	7.05

To estimate the regioregularity of the polymer this signals are not the best choice because of the vicinity of the corresponding shifts. The better method to assess the relative ratio of regular to irregular coupling is to take the α -carbon protons on the alkyl chain. The HT coupled α -carbon protons are observable at 2.80 ppm whereas the irregular coupled protons lead to a peak at 2.58 ppm.^[50] A further interesting information from the ^1H spectra is the estimation of the chain length, which can be obtained by the ratio of the vinylic end group protons to the aromatic protons. However, this method is only a rough estimation of the chain length and should only be applied for small molecular weight polymers.

⁴⁹ Mao, H.; Xu, H.; Holdcraft, S. *Macromolecules* **1993**, 26, 1163

⁵⁰ Sato, M.; Morii, H.; *Polym. Commun.* **1991**, 32, 42

An exemplary ^1H - NMR spectrum of the sample **P1** prepared using 1.0 eq of *tert*-BuMgBr is depicted in Figure 21. The used ratio of monomer to catalyst was 30/1 in this case so that an average chain length of 30 monomer units is expected. The aromatic region shows a singlett at 6.98 ppm which can be attributed to the HT-coupled thiophene rings. At 7.00 ppm a small shoulder appears in the peak which belongs to the TT-HT coupled pair at the beginning of the chain. Additionally, some small peaks between 6.95 and 6.82 belonging to less deshielded protons at the beginning and end of the polymer chain.^[51]

The signal from the vinylic end group can be seen with small intensity at 5.12, 5.51 and 6.52 ppm. By comparing the integrals of these protons with the integral of the aromatic protons a chain length of around 40 monomer units is obtained. This value is too high, considering that a ratio of monomer to initiator of 30/1 was used for the synthesis. This discrepancy will be explained by the contribution of other end groups later on.

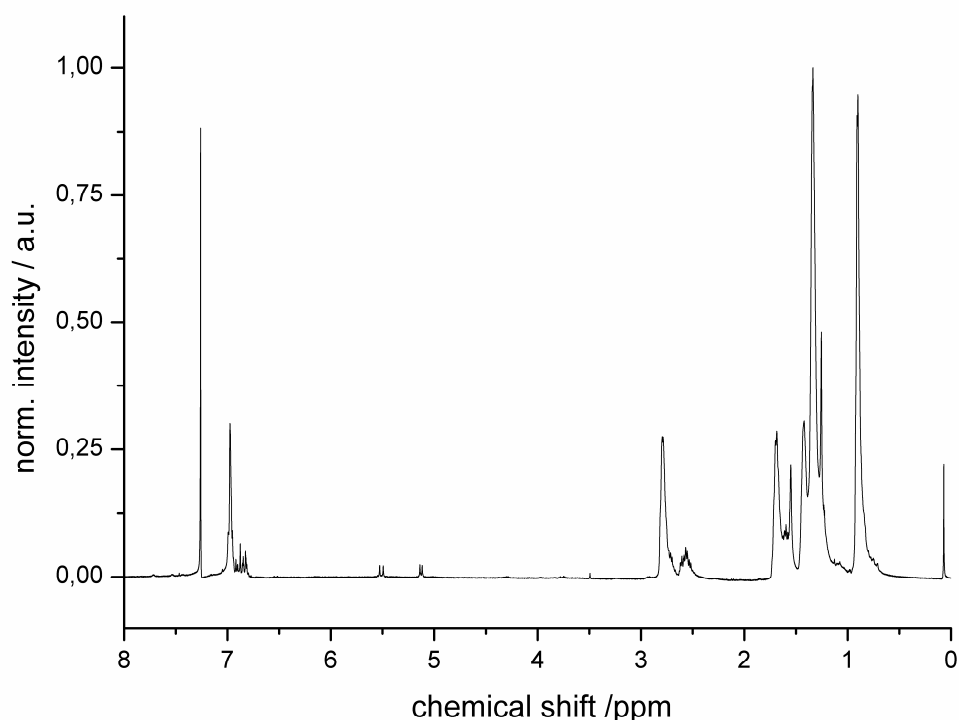


Figure 21. ^1H NMR of poly(3-hexylthiophene).

The α -carbon protons are observable at 2.80 ppm whereas the irregular coupled protons lead to a peak at 2.58 ppm. The relative integral shows that the irregular coupled

⁵¹ Bras, J.; Pepin-Donat, B. *Magn.Reson.Chem.* **2001**, 39, 57

protons contribute with around 8% to the overall signal. This value corresponds quite well to the theoretical value of 6.7%. The β -carbon protons can be found at 1.69 ppm. The other CH_2 - protons yield a broad peak centered around 1.40 ppm and the CH_3 -group leads to a singlett at 0.91 ppm.

By setting the integral of the aromatic thiophene proton to one, polymer **P2** shows a higher integral of the CH_3 - group protons with a value of 4.5 compared to 3.2 in **P1**. Moreover, virtually no signal from the vinylic end group was found. To understand these observations also matrix assisted laser desorption ionization - time of flight mass spectrometry (MALDI-TOF MS) measurements were performed to determine the end group composition. The advantage of this method is its ability to analyze polymers with a minimum of fragmentation in the mass spectrometer.^[52] The results are shown in Figure 22.

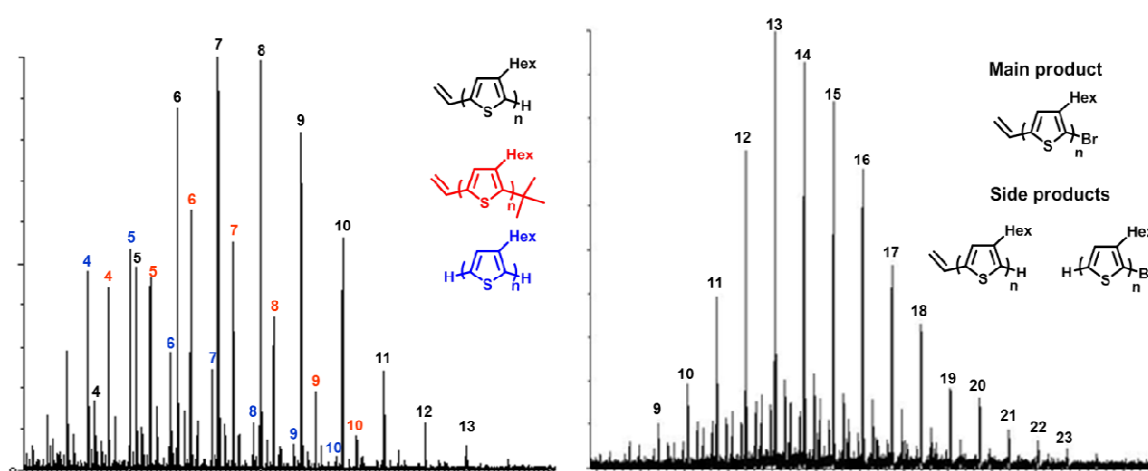


Figure 22. MALDI-TOF results from **P2** (left) and **P1** (right).

The measurements showed that the polymer **P2** consists of three products. The main product is the desired polythiophene with a vinyl end group. But during the synthesis also two side products were formed in significant amounts. The first also bears a vinyl end group but surprisingly a *tert*-butyl-group is attached to the other side. This end group is responsible for the relative high methyl-group integral in the ^1H - NMR spectrum. The second consists of the polythiophene main chain with two hydrogen atoms at the end. A comparison with **P1** shows that in the case of prolonged reaction

⁵² Jeffries-El, M.; Sauve, G.; McCullough, R.D. *Macromolecules*, **2005**, 38, 10346

time with *tert*-BuMgBr mainly the desired product was formed. Only minor traces of side products are observed. In this case the first is like the main product but with hydrogen instead of the bromine at the chain end. This side product is already known from literature.^[52] Miyakoshi et al. attributed this phenomenon to the use of a not stoichiometric use of the Grignard reagent. The second side product bears a hydrogen atom at one chain end and a bromine atom at the second chain end. This side product is responsible for the higher ratio of the aromatic protons to the protons from the end group obtained in the ¹H - NMR spectrum.

A possible explanation for these results is that the prolonged reaction time results in a quantitative consumption of the Grignard reagent. However, shorter reaction times lead to a situation where the *tert*-BuMgBr is still available in the presence of the catalyst. This results in further possible reaction paths, depicted in Figure 23.

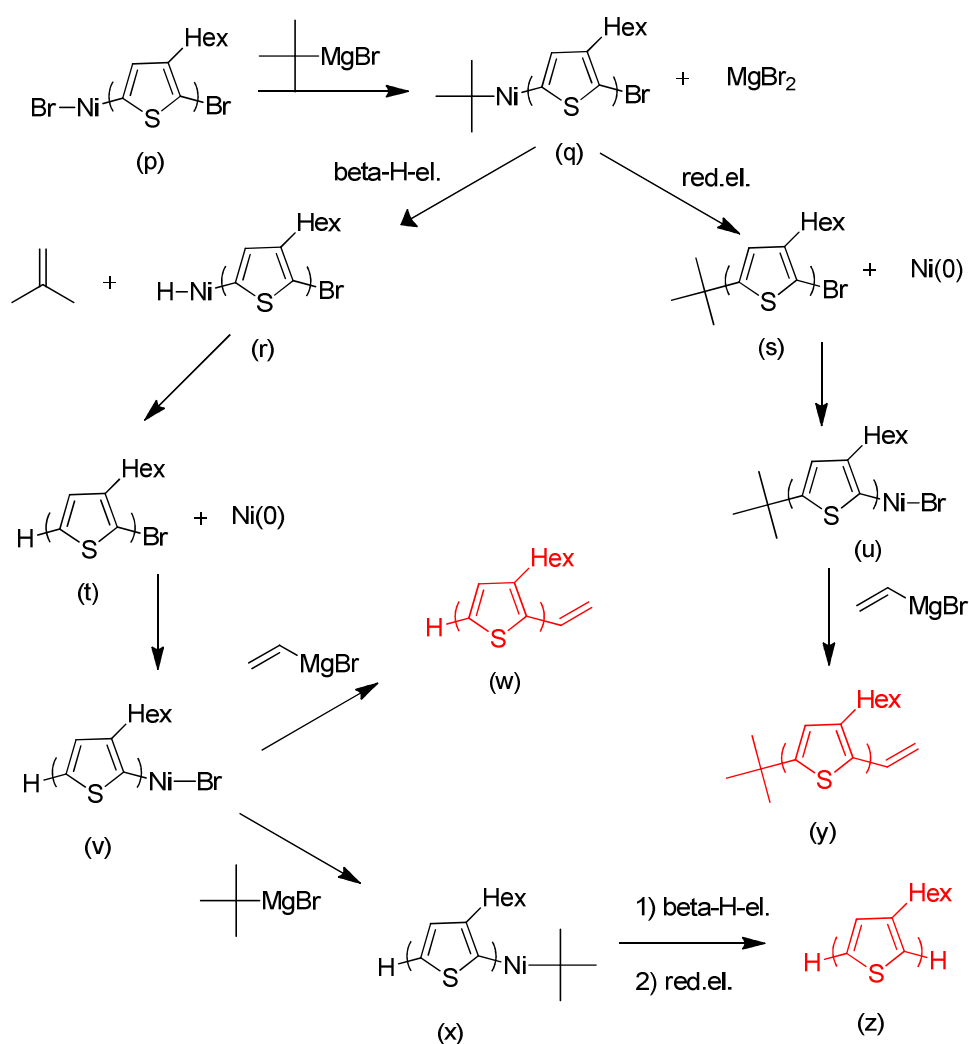


Figure 23. Possible reactions leading to the observed side products.

The active species **p** can react with the still available *tert*-BuMgBr to form the intermediate **q**. This organic nickel species can either undergo a β -H-elimination to form **r** or a reductive elimination to form compound **s**, which still has an active bromine atom which can react with the initiator in an oxidative addition to form **u**. Quenching of the reaction with the vinylic Grignard species yields **y**, which was found in **P2**. Compound **r** can undergo a reductive elimination to produce **t**. Also in this case the active bromine at the other side leads to an oxidative addition of the initiator to yield **v** as intermediate product. Depending on the availability, **v** can react either with the *tert*-butyl – or the vinylic Grignard species to form **x** or **w**. As already mentioned, **w** is a common byproduct using GRIM as polymerization procedure. Compound **x** can undergo a β -H-elimination followed by a reductive elimination of nickel. This yields the polymer **z** with hydrogen atoms at both sides. It has to be noted that the reaction mechanisms explain all observed reaction products. However, the confirmation of the proposed mechanisms would have exceeded the timeline of this work, so that it was not further pursued.

To conclude briefly, it was shown that the polymerization procedure and the obtained products are highly dependent on the reaction conditions. The addition of the *tert*-butyl Grignard reagent has to be in a one to one ratio and furthermore the time of reaction has to be chosen so that complete consumption can be ensured.

For all following polymerization procedures the reaction time for the addition of the Grignard reagent was 5 hours or even over night. Another important point was to show that for end-functionalized polymers the use of MALDI-TOF MS measurements is superior compared to NMR measurements. This is due to the ability of the former method to accurately give insight in the different end groups. In NMR measurements the DP can only be roughly estimated if no significant amounts of other end groups are present. A complementary way to measure the chain length is gel permeation chromatography (GPC). The results for **P1** and **P2** are shown in Table 2.

Table 2. GPC results of **P1** and **P2** with THF as solvent.

	M_n	M_w	PDI	DP
P1	2330	3910	1.68	14
P2 (hexane)	2160	2960	1.37	13
P2 (chloroform)	4230	5100	1.20	25

Polymer **P2** was fractionated making use of a Soxhlet extraction with hexane to collect the oligomers and with chloroform to obtain the high molecular weight fraction. GPC was measured with THF as solvent. It should be noted that GPC is a method which compares the hydrodynamic volume of a polymer standard, used for calibrating the instrument, to the polymer of interest. In most cases the instrument is calibrated with polystyrene standards which exhibit a coil-like structure in solution. Contrarily, polythiophenes are rigid, because of their conjugated backbone. This leads to a stick-like structure in solution. The different behavior of these two classes of polymers leads to a discrepancy in the results.

For example, **P1** has a number weighted distribution of 2330 g/mol, which corresponds to a DP of 14. But comparing this result with the MALDI-TOF MS measurements which showed a maximum signal for a DP of 8 the value is quite too big. The same is true for **P2** which shows a DP of 25 (chloroform fraction) compared to around 13 in the MS measurements. However, for relative considerations of polymers with different chain lengths and because the PDI value can easily be obtained, this method still has some value in assessing the polymer quality. Furthermore, it can be seen from Table 2 that the Soxhlet extraction works in fractionating the polymer in low and higher molecular weight samples. The obtained PDI values are for **P2** with 1.37 and 1.20 in a good range. **P1** has a comparable high PDI of 1.68 which can be explained by the high extent of different occurring side reactions as described previously.

2.2.3 Synthesis of block copolymers using vinyl - terminated P3HT

To study the formation of the block copolymers **P3** was used, which was synthesized with a monomer to initiator ratio of 40/1. The MALDI-TOF MS measurements showed that the average DP is around 21 and the vinylic end group is present. The only formed side product is the polythiophene with hydrogen on the other chain end. **3** was used as sort of model comonomer because it was easy available and appropriate to study the coupling reaction. As catalyst a Grubbs initiator of the third generation was used due to its high reactivity. The solvent of the reaction was dichloromethane (abs.). The reactions were performed either in the glove box under inert atmosphere or under argon using conventional Schlenck-techniques.

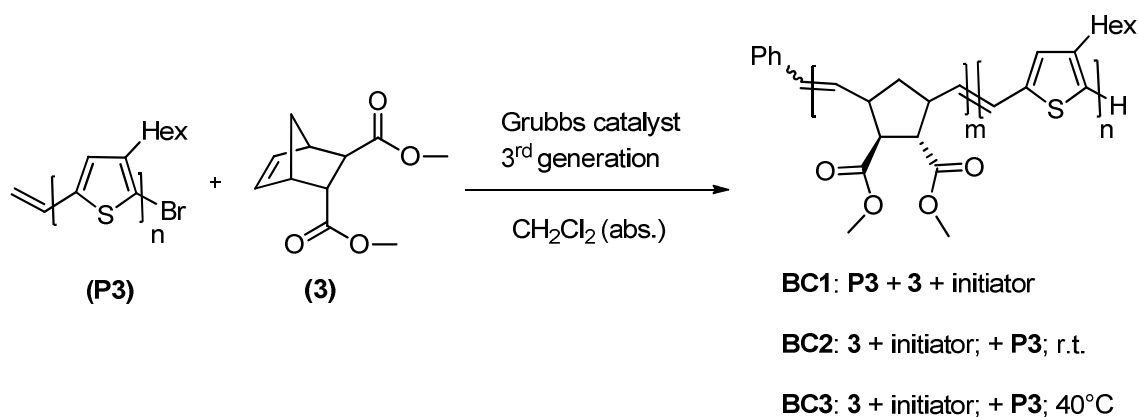


Figure 24. Reaction scheme for the synthesis of the block copolymers **BC1-BC3**.

The reaction was performed in three different ways. In the first type of reaction, **P3** and **3** were mixed and afterwards the initiator was added at room temperature (**BC1**). In the second experiment **3** was first polymerized with the initiator and after complete consumption of the monomer, which was evaluated by thin layer chromatography (TLC), **P3** was added (**BC2**). Afterwards the reaction was stirred at room temperature over night. The third type of reaction was performed in the same way, with the only difference that the reaction mixture was refluxed at 40°C (**BC3**). For all three reaction types **3** was added in an amount which should give a 1/1 block copolymer.

These reactions were characterized by NMR spectroscopy, GPC and finally with MALDI-TOF MS. As expected, the NMR spectra showed that **3** always yielded a polymer, observable by the signal between 5.12 and 5.57 ppm which can be attributed to the olefinic protons. However, the coupling of the polythiophene cannot be accurately demonstrated by NMR studies, due to the small signal of the end group. Complete absence of this signal was observed. However, also other side reactions are suitable to cause this effect. For example the dimerization of the polythiophene or the cleavage of the end groups would give the same result.

The results from the GPC measurements are summarized in Table 3. The formation of a block copolymer should result in higher molecular weights compared to **P3**. But as can be observed from Table 3, **BC1** and **BC2** are in the same range as **P3**. **BC3** has an even lower molecular weight. Through these results also the side reaction of polythiophene dimerization can be excluded, due to the fact that higher molecular weight fractions with about doubled molecular weight are absent.

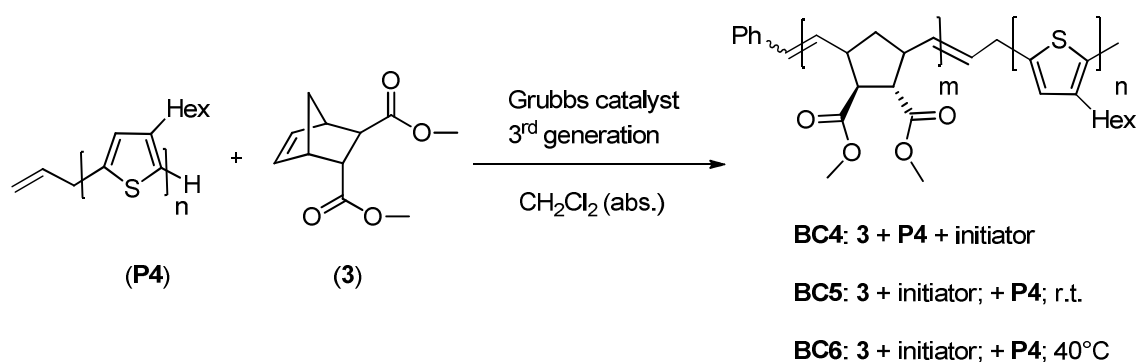
Table 3. GPC results of **P3** and **BC1-BC3**.

	M_n	M_w	PDI
P3	9510	11840	1.25
BC1	9350	12550	1.34
BC2	9000	11750	1.31
BC3	8260	11420	1.38

And finally MALDI-TOF MS measurements showed that no copolymers were formed. The obtained products are a mixture of two homopolymers. For **BC2** some additional peaks were present which could be a hint that some sort of end group modification happened to the polythiophene. But due to the fact that a polymer mixture was investigated, too many peaks were present, making a deeper analysis impossible. Recapitulating, the building of block copolymers containing a thiophene block and a norbornene block was not successful. A possible reason for this could be the steric demand of the Grubbs initiator, which hinders the coordination to the vinylic end group of the polythiophene.

2.2.4 Synthesis of block copolymers using allyl - terminated P3HT

In this set of experiments the same reactions as before were performed, with the only difference of using a polythiophene with an allylic end group. The introduction of the additional methylene group provides more rotational freedom of the end group and increases the distance of the bulky catalyst from the thiophene backbone.

**Figure 25.** Reaction scheme for the synthesis of the block copolymers **BC4-BC6**.

The polythiophene **P4** was synthesized with a ratio of monomer to initiator of 20/1. This was done to ensure that informations about the coupling reaction can also be obtained

by NMR measurements. As depicted in Figure 26 the allylic end group leads to three different peaks in the spectrum.

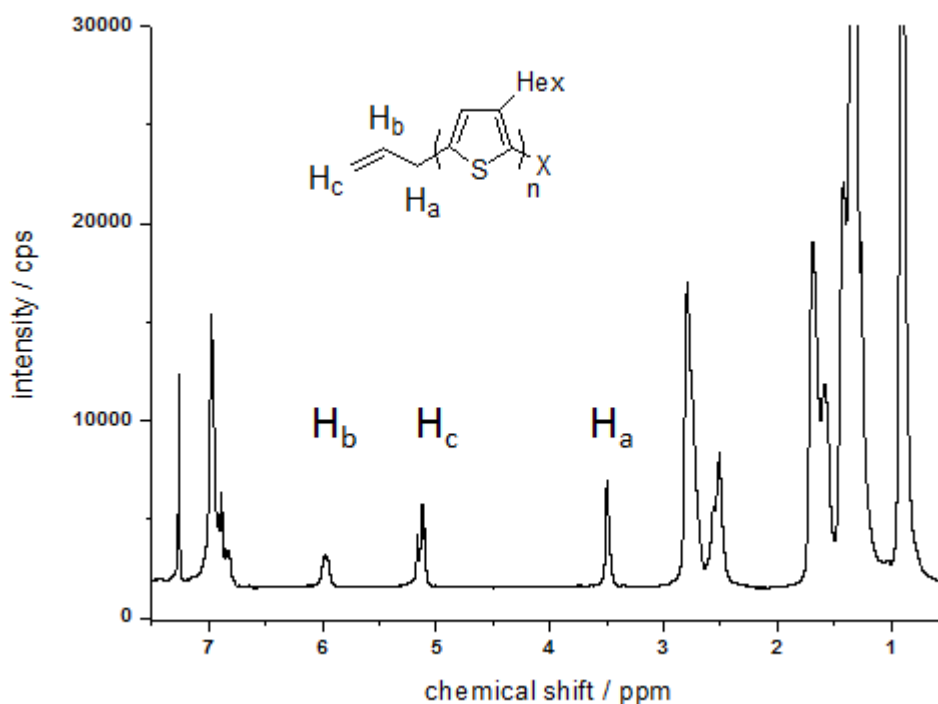


Figure 26. ¹H - NMR spectrum of **P4**.

The H_a – protons next to the aromatic ring lead to a signal at 3.50 ppm. The vinylic protons H_b and H_c can be found at 5.97 and 5.12 ppm. The relative intensities correspond to the theoretical values. By comparing the integrals of the α -carbon protons to the vinylic protons H_c a chain length of 13 monomer units can be estimated. MALDI-TOF MS measurements showed an average chain length of 11 monomer units, due to the formation of the side product with hydrogen on the second chain end.

The analysis of the reaction products of the coupling reaction showed that also in this case the protons of the double bond at the chain end of the polythiophene disappear in the NMR spectrum for all three types of reaction. In **BC6** a small peak at 9.86 ppm aroused which can be attributed to an aldehyde functionality. Additionally, the MALDI-TOF MS measurements showed an end group modification with an aldehyde functionality. An exemplary mass spectrum of **BC6** is depicted in Figure 27. It is worth mentioning that in these spectra no signals from the polynorbornene block can be observed. The reason for this difference, compared to **BC1-BC3** is that smaller blocks were synthesized in this case. This means that the polynorbornene block was too low in

molecular weight for a precipitation in methanol and therefore was successfully removed from the polythiophene block, ensuring a deep analysis by MS.

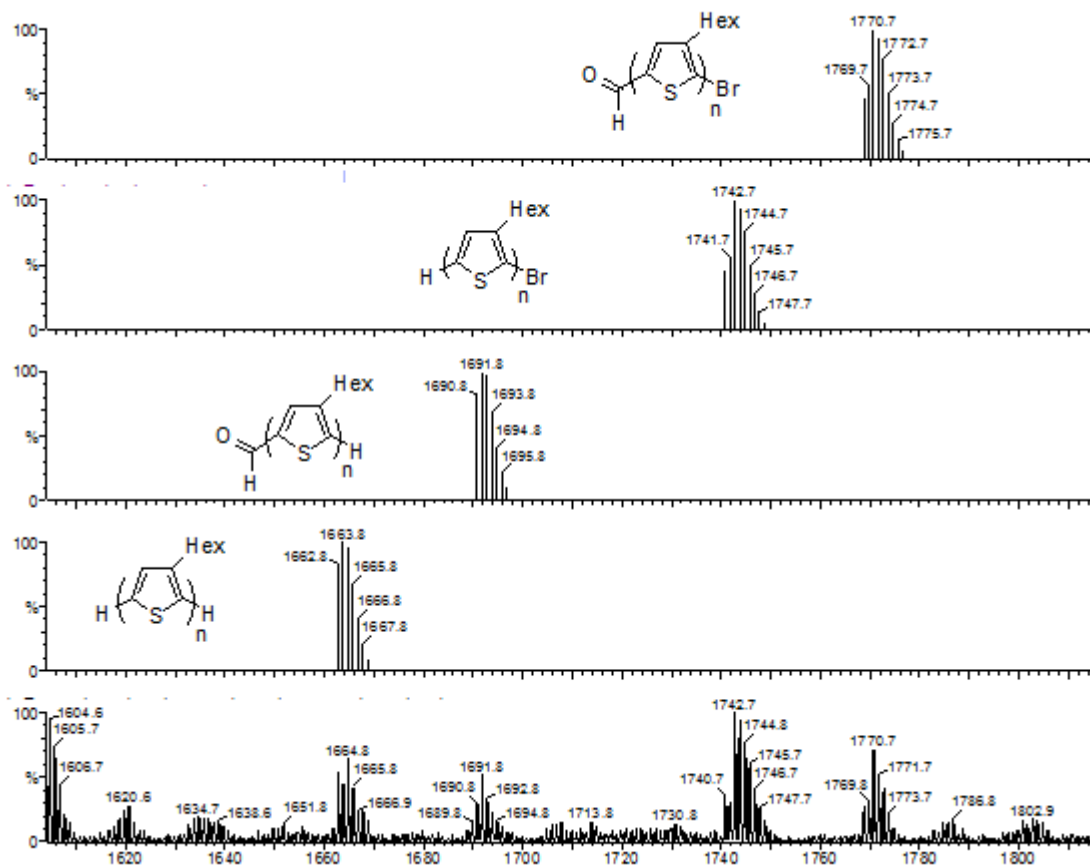


Figure 27. MALDI-TOF MS measurement of **BC6**.

As can be seen the allylic end group of the polythiophene **P4** is nearly completely consumed during the reaction. Only a small signal at 1730.8 m/z is left. The main reaction products are the polythiophenes with bromine or hydrogen on one chain end and hydrogen or an aldehyde functionality on the other chain end (Figure 28).

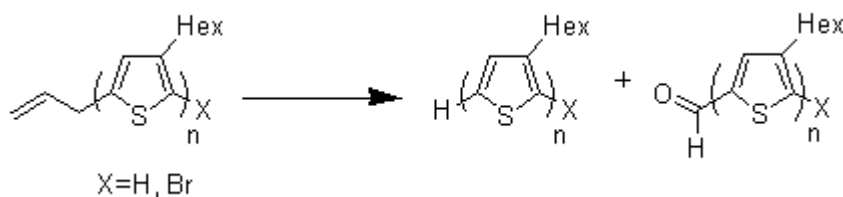


Figure 28. Reaction products.

These products are also formed in **BC4** and **BC5**, although the relative amounts differ. At room temperature the cleavage of the allyl group is dominant, whereas elevated temperatures favor the formation of the aldehyde. One possibility for the formation of the aldehyde end group is depicted in Figure 29.

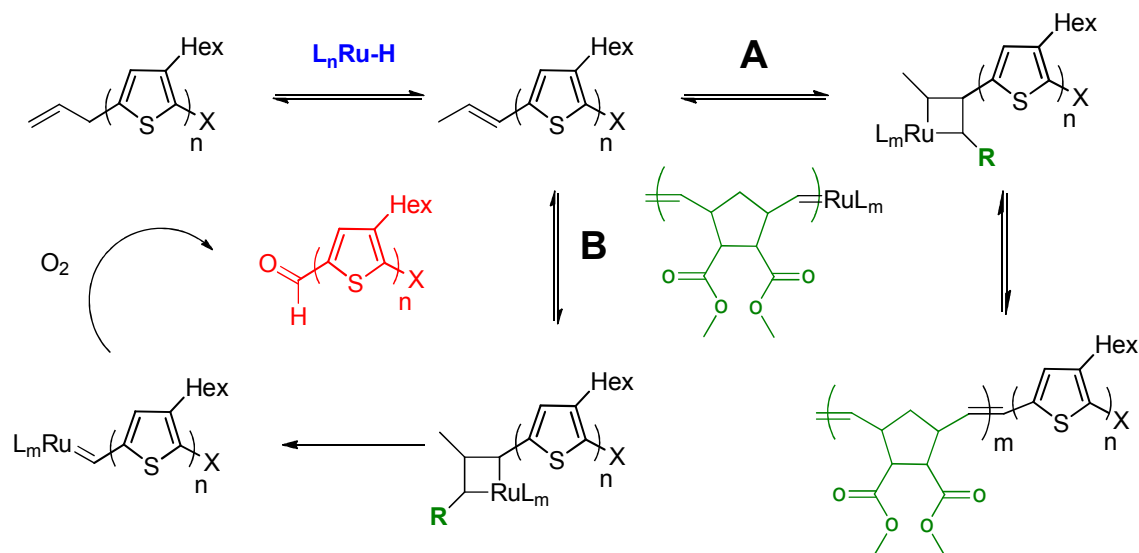


Figure 29. Possible formation mechanism of the aldehyde functionality.

It is already known from literature that Grubbs catalysts can form hydride complexes (L_nRu-H in Figure 29) if primary alcohols and/or water are present in the reaction mixture.^[53] In our reaction system both species could be present in small amounts due to the long reaction time and the fact that the functionalized polythiophene was precipitated in methanol. These hydride species have already been proposed to be the active species in the isomerization of double bonds, which can be seen in some of the reactions using ruthenium metathesis catalysts.^[53,54] In this case this would mean that the double bond at the chain end isomerized to position two. In the next step an unchanged Grubbs catalyst, located at the chain end of the poly(norbornene) can coordinate to this newly formed double bond. This can happen in two possible orientations, which is shown in Figure 29 as path A and path B. For a successive block copolymer formation the two polymer chains have to follow path A, meaning that they rearrange in a way which gives rise to high steric demands, making this orientation unfavorable. Following path B, the polymers are oriented in a way that the chains are

⁵³ Dinger, M.B.; Mol, J.C. *Organometallics*, **2003**, 22, 1089

⁵⁴ Fürstner, A.; Thiel, O.R.; Ackermann, L.; Schanz, H.-J.; Nolan, S.P. *J.Org.Chem.* **2000**, 65, 2204

pointing towards other directions. This favored orientation leads to a binding of the ruthenium initiator to the end group of the polythiophene. The final step of the reaction is the addition of oxygen to the ruthenium - carbon double bond which leads to the final product with aldehyde end groups. This final step was also observed for several occasions in literature reports.^[55] However, currently an explanation about the reaction mechanisms resulting in the cleavage of the end group is cannot be provided.

To sum up, the formation of block copolymers is highly improbable, due to the high steric demand of the intermediate, which leads to the desired coupling product. The sterically more favorable transition state leads to a coupling of the catalyst to the end group of the thiophene. In the presence of oxygen the end group gets converted into an aldehyde functionality. This result, although not helpful for this work, can lead to a new way of functionalizing the end groups of polythiophenes.

2.2.5 Comblike block copolymers

As the formation of block copolymers by direct coupling of the polythiophene block to the polynorbornene by the Grubbs catalyst did not work, an alternative strategy was followed. The synthesis scheme is depicted in Figure 30. Using **4** as educt, another polythiophene with an allylic end group was synthesized (**P5**). In the next step the double bond was converted into an alcoholic functionality through hydroboration yielding compound **P6**. Esterification with *endo, exo*[2.2.1]bicyclo-hept-5-ene-2,3, dicarboxylic acid chloride introduces a polymerizable group, suitable for ring opening metathesis polymerization (ROMP). In the final polymerization step, **5** was used to build up a homopolymer **BC7** and through the polymerization with *endo, exo*[2.2.1]bicyclo-hept-5-ene-2,3-di-*tert*-butyl-dicarboxylate as comonomer a block copolymer **BC8** was synthesized. The method of introducing a functional unit, separated by a spacer, to a norbornene is an often used method. Several reports for the incorporation and subsequent polymerization using ROMP are known from literature.^[56,57]

⁵⁵ Qin, Y.; Hillmyer, M.A. *Macromolecules* **2009**, 42, 6429

⁵⁶ Roh, Y.; Bauld, N.L. *Adv.Synth.Catal.* **2002**, 2,344

⁵⁷ Zaami, N.; Slugovc, C.; Pogantsch, A.; Stelzer, F. *Macromol.Chem. Phys.* **2004**, 205, 523.

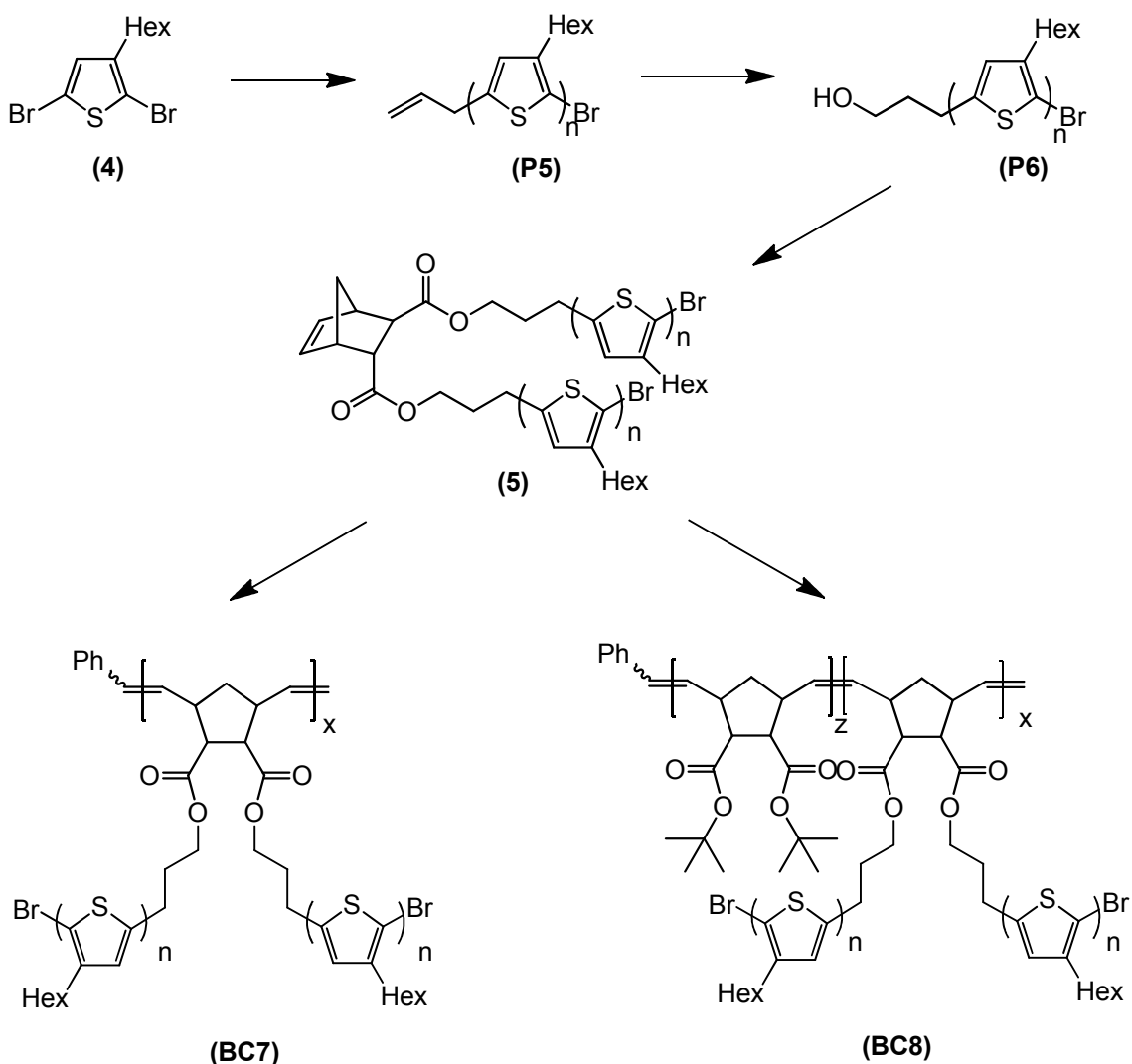


Figure 30. Synthesis of comblike block copolymers.

2.2.5.1 Synthesis and characterization

The allyl-terminated polythiophene **P5** was synthesized, with a monomer to initiator ratio of 15/1 in order to get low molecular weight oligomers, which also allow the investigation of the reaction progress through simple NMR spectra. For the following hydroboration 9-borabicyclo[3.3.1]nonane was used as reagent. The reaction was performed in THF (abs.) at 40°C over night. The progress of the reaction was investigated by TLC. After nearly complete consumption of the educt, NaOH (5M) was added to the reaction mixture. After stirring for further 15 minutes and cooling to room temperature hydrogen peroxide (30%) was added. Then the reaction solution was again stirred at 40°C over night to complete the oxidation. The solvent was evaporated under reduced pressure and after dissolving in dichloromethane inorganic byproducts were

separated by extraction with water. In the next step the organic phase was separated, concentrated and precipitated in MeOH. After filtration and drying, the product was obtained with a yield of 89%. The introduction of the alcoholic function was proved by NMR, MALDI-TOF MS and Fourier Transform Infrared (FTIR) measurements. The NMR spectra showed the absence of the mentioned signals from the allyl-group. Three new signals at 3.75, 2.86 and 1.94 ppm aroused, which can be attributed to H_c, the proton next to -OH, H_a, the proton next to the aromatic ring and H_b, the proton between the two CH₂ - groups. MS measurements showed the successful introduction of the alcoholic functionality as is depicted in Figure 31.

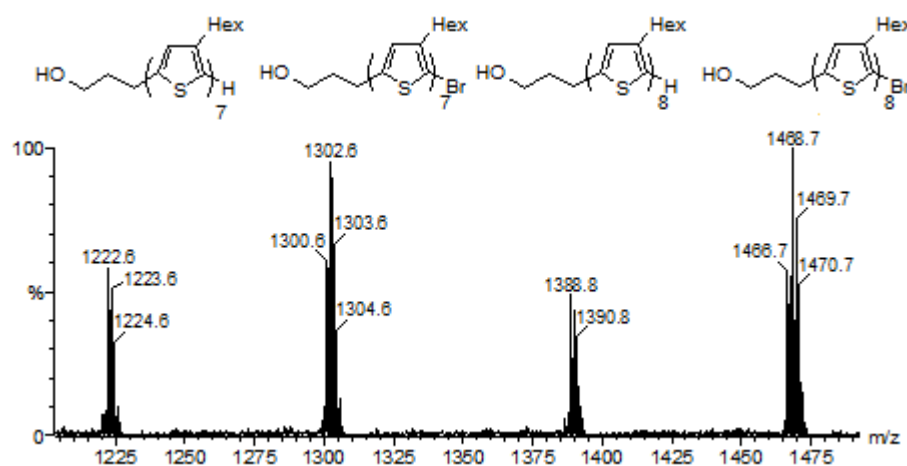


Figure 31. MS results of **P5**.

As can be seen the product is pure and consists only of the desired compound. The second chain end in this polymer is also terminated either by bromine or hydrogen.

The esterification of **P6** with *endo, exo*[2.2.1]bicyclo-hept-5-ene-2,3-dicarboxylic acid chloride was done in the presence of pyridine. As reaction solvent anhydrous dichloromethane was used. The reaction was stirred over night at room temperature. To remove the excess of pyridine the solution was extracted with HCl (5%) and NaHCO₃ (sat.). After that the organic phase was concentrated by solvent evaporation under reduced pressure. The product was purified by column chromatography with a solvent mixture of cyclohexane and ethyl acetate (20/1) as eluent. The yield of the reaction was 63%. The formation of the product was confirmed by NMR. First of all, the characteristic peaks of the norbornene appeared, and secondly, the peak of the protons, initially next to the alcohol functionality shifted from 3.75 to 4.19 ppm.

The reaction sequence described so far was also confirmed by FTIR measurements. The corresponding spectra are summarized in Figure 32. The detailed data are given in the experimental section. Here only the most important changes are described. The hydroxypropyl - terminated P3HT, **P6** shows the typical broad peak around 3400 cm^{-1} corresponding to hydrogen bonds, arising from the alcohol function. This peak disappears after esterification and new peaks at 1733 and 1180 cm^{-1} , corresponding to the introduced ester functionality can be seen.

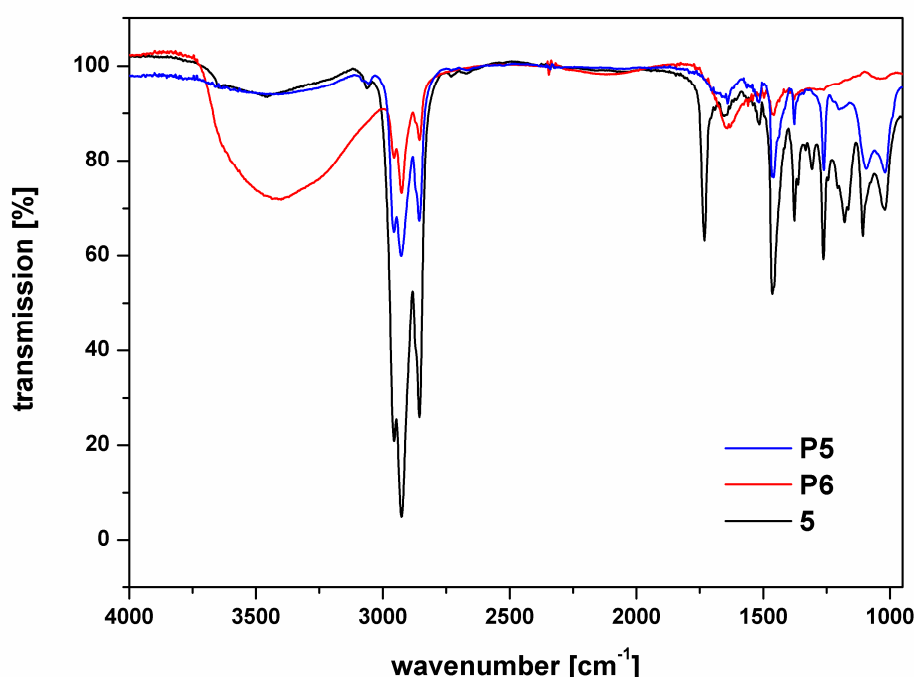


Figure 32. FTIR spectra of **P5**, **P6** and **5**.

For the polymerizations the Grubbs catalyst of the third generation was used. The reactions were performed with anhydrous dichloromethane as solvent. The homopolymer **BC7** was polymerized with a monomer to initiator ratio of 20/1 by stirring the reaction at room temperature over night. Thin layer chromatography showed complete consumption of the monomer. Therefore the reaction was quenched with ethylvinylether. After stirring for further 10 minutes the reaction solution was concentrated by solvent evaporation under reduced pressure. The polymer was precipitated in MeOH which has been cooled to 0°C before use and allowed to settle down over night. The red precipitate was finally dried in vacuum to give the polymer with 76.5% yield. The formation of the polymer was confirmed by NMR measurements.

Due to the formation of the double bonds in the main chain the significant broad peak from 5.57-5.12 ppm can be seen.

The block copolymer **BC8** was synthesized in the same way. The ratio of **M1**/comonomer/initiator was 10/200/1. First, the catalyst was added to the comonomer and after complete consumption, achieved by stirring over night, **M1** was added to the reaction solution. Then the reaction was allowed to further stir at room temperature for 20 hours. Afterwards the reaction was quenched with ethylvinylether. The rest of the work up was performed in the same way as described for the homopolymer. The yield of the reaction was 51%.

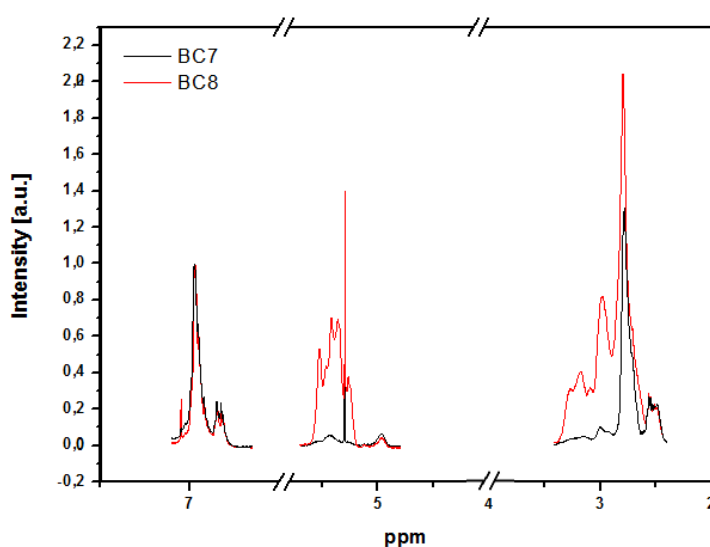


Figure 33. Comparison of characteristic regions from **BC7** and **BC8**.

To confirm the formation of the block copolymer **BC8**, some characteristic NMR regions of both polymers are shown. The spectra were normalized in a way that the integrals of the aromatic proton from the thiophene ring, at 6.98 ppm were equal. Also in this case the significant broad peak from 5.57-5.12 ppm can be seen, indicating the formation of the main chain double bonds. Compared to **BC7**, this peak is more pronounced due to the comonomer contributing to this integral. The last peak at around 3 ppm consists of the α -carbon protons of the hexyl chain next to the thiophene and the signal in the upper region stems from the protons of the cyclopentane ring in the polymer backbone. Once again, for **BC8** this integral is more pronounced. The relative amount of the two different monomers in the polymer was evaluated by integrating the methyl - protons of the norbornene to the aromatic proton of the thiophene in the second

block. The calculation gives a value of around 20/1 which corresponds very well with the used amounts.

Summing up this chapter shortly, the synthesis of block copolymers was successful through the end group modification of polythiophene. Esterification with norbornene derivatives is possible and results in the introduction of a polymerizable group. The electroactive group is in this case in the side chain. By appropriate choice of comonomers, the introduction of a second block, suitable for the coordination to nanoparticle surfaces is possible.

2.2.5.2 Photophysical characterization of BC7 and BC8

Absorption and emission spectra of the two polymers **BC7** and **BC8** were recorded using dichloromethane as solvent. The concentration of **BC7** was $2.13 \cdot 10^{-6}$ g/mL and for **BC8** $5.5 \cdot 10^{-6}$ g/mL. The absorption maximum is centered around 429 nm for both polymers and can be attributed to a $\pi - \pi^*$ - transition of the conjugated backbone of the thiophene block.^[58]

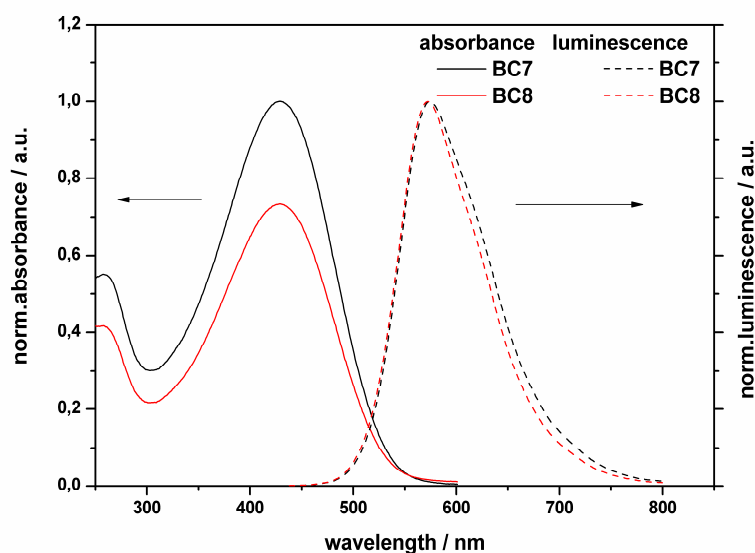


Figure 34. Absorption and emission spectra of **BC7** and **BC8**.

The maximum is 7 nm red - shifted compared to the hydroxypropyl - terminated oligothiophene. This may be explained by the π – stacking of the oligothiophenes in the side chain, leading to a more extended conjugation system. The intensity of this transition is lower for **BC8**. This can be explained by the dilution of the thiophene dyes by the comonomer. The broad and structureless emission of both polymers has its maximum at 572 nm.

2.3 *Experimental*

2.3.1 Materials and Methods

All chemicals were purchased from Sigma Aldrich in the purest available form and used for syntheses without further purification steps. The solvents were purified according to known literature procedures.^[59] The reactions were performed under an inert atmosphere of purified nitrogen or argon using Schlenck techniques unless otherwise stated.

¹H - NMR spectra were recorded on a Varian INOVA 500 MHz Spectrometer at 500 MHz, the corresponding ¹³C - NMR spectra were recorded at 125 MHz. Solvent residual peaks were used for referencing the NMR - spectra to the corresponding values given in literature.^[60] For the multiplicity of the peaks the following nomenclature was used, s for singulett, bs for a broad singulett, d for doublet, dd for dupletic doublet, t for triplett, p for pentett and m for multiplatt. FTIR spectra were measured on a Perkin Elmer Spectrum One IR spectrometer with a DTGS detector. The spectra were obtained from films on KBr or NaCl windows. The intensities were named s for strong, m for medium and w for weak.

The number average molecular weights (M_n), weight average molecular weights (M_w) as well as the polydispersity index (PDI) were determined by gel permeation chromatography with THF as solvent using the following arrangements. THF setup: Merck Hitachi L6000 pump, separation columns of Polymer Standards Service, 8 x 300 mm SDV 5 μ m grade size (106 Å, 104 Å, and 103 Å), combined refractive index –

⁵⁹ Perrin, D. D.; Armarego, W. L. F. *Purification of Laboratory Chemicals*, 3rd ed.; Pergamon: New York, **1988**.

⁶⁰ Gottlieb, H. E., Kotlyar, V., Nudelman, A. *J. Org. Chem.*, **1997**, 62, 7512 - 7515

viscosity detector from the company Viscotec. Polystyrene standards purchased from Polymer Standard Service were used for calibration of the setups.

UV-Visible absorption spectra were recorded on a Cary 50 Bio UV-Visible Spectrophotometer, fluorescence spectra on a Hitachi F-7000 fluorescence spectrometer (www.inula.at) equipped with a red-sensitive photomultiplier R 928 from Hamamatsu (www.hamamatsu.com). The emission spectra were not corrected for the sensitivity of the PMT.^[122]

MALDI-TOF mass spectra were recorded on a Micromass TofSpec 2E. The instrument is equipped with a nitrogen laser (337 nm wavelength, operated at a frequency of 5 Hz), and a time lag focusing unit. Spectra were taken in reflectron mode at an accelerating voltage of +20 kV. Analysis of data was done with MassLynx 3.4 (Micromass, Manchester, UK). Samples were dissolved in THF (1 mg mL⁻¹) with Dithranol as matrix (10 mg mL⁻¹ in THF). Solutions were mixed in the cap of a microtube in the ratio of 1 µL : 10 µL : 0.5 µL. The resulting mixture was spotted onto the target and air dried.^[122]

2.3.2 Syntheses procedures

2.3.2.1 Synthesis of the monomer

2,5-dibromo-3-hexylthiophene (1)

A solution of 3-hexylthiophene (20g, 118.84 mmol) and *N*-bromosuccinimide (52.88 g, 297.09 mmol, 2.5 eq) in THF (abs.) (150 mL) was stirred at room temperature overnight. The reaction progress was monitored by TLC (cyclohexane on silica). After the educt was nearly completely consumed the solvent was removed by rotary evaporation. Then 150 mL heptane were added to precipitate the succinimide. Filtration and removal of the solvent afforded the crude reaction product. Purification was done by distillation under reduced pressure. The product was obtained at a temperature of 87°C with a vacuum of 0.15 mbar (32.575 g, 84%).

¹H - NMR (δ, 20 °C, CDCl₃, 500 MHz): 6.77 (s, 1H, T4), 2.50 (t, 2H, Hex1), 1.54 (p, 2H, Hex2), 1.30 (m, 6H, Hex3-5), 0.89 (t, 3H, Hex6)

¹³C - NMR (δ, 20°C, CDCl₃, 125 MHz): 142.9 (1C, T3), 130.9 (1C, T4), 110.3 (1C, T2), 107.9 (1C, T5), 31.5, 29.5, 29.4, 28.8, 22.6 (5C, Hex1-5), 14.1 (1C, Hex6)

2.3.2.2 Polymerization using GRIM with vinylic end groups

Syntheses of **P1** and **P2**^[52]

2,5-dibromo-3-hexylthiophene (333.35 mg, 1.02 mmol) was dissolved in anhydrous THF (6 mL). *Tert*-BuMgBr (0.5 mL, 1.02 mmol) was added via syringe and the mixture was refluxed for 5 hours in the case of **P1** and for 3 hours in the case of **P2**. After cooling the reaction mixture to room temperature, Ni(dppp)Cl₂ (57.4 mg, 0.104 eq for **P1** and 19.2 mg, 0.034 eq for **P2**), dissolved in THF was added. The reaction mixture was stirred for 10 minutes at room temperature, then vinylmagnesium bromide (0.25 mL, 50 mol% of monomer) was added via syringe to the reaction mixture. After stirring for further 10 minutes the reaction mixture was poured into methanol to precipitate the polymer. **P2** was filtered in to an extraction thimble and was washed by Soxhlet extraction with methanol, hexane and chloroform.

P1: ¹H - NMR (δ, 20 °C, CDCl₃, 500 MHz): 6.98 (s, 1H, T4), 6.52 (m, vinyl), 5.51 (d, J=11Hz, 0.025H, vinyl), 5.12 (d, J=11Hz, 0.025H, vinyl), 2.80 (m, 2.1H, Hex1 (regular)), 2.58 (m, 0.25H, Hex1(irregular)), 1.69 (m, 2H, Hex2), 1.40 (m, 6H, Hex3-5), 0.91 (m, 3H, Hex6)

P2: ¹H - NMR (δ, 20 °C, CDCl₃, 500 MHz): all signals are the same as for **P1**, except the following: 0.91 (m, 4.5H, Hex6)

P1 and **P2**: ¹³C - NMR (δ, 20°C, CDCl₃, 125 MHz): 139.9 (1C, T3), 133.67 (1C, T5), 130.5 (1C, T4), 128.6 (1C, T2), 31.7 (1C, Hex1), 30.5 (1C, Hex2), 29.3 (2C, Hex3-4), 22.7 (1C, Hex5), 14.1 (1C, Hex6)

GPC analysis: **P1**: PDI = 1.68, M_n=2330 g/mol, M_w=3910 g/mol; **P2** (hexane): PDI = 1.37, M_n=2160 g/mol, M_w=2960 g/mol; **P2** (chloroform): PDI = 1.20, M_n=4230 g/mol, M_w=5100 g/mol

MALDI MS (m/z): **P1**: 2268.63 (calcd. 2268.65; DP of 13; Br/vinyl, H/vinyl and H/Br end groups); **P2**: 1356.65 (calcd 1356.68; DP of 8; H/vinyl, tert-Butyl/vinyl, H/H end groups)

Synthesis of **P3**

The synthesis of **P3** is the same as already described for **P1** with the only differences that the reaction with *tert*-BuMgBr was stirred over night and that a monomer to initiator ratio of 40/1 was used.

^1H - NMR (δ , 20 °C, CDCl_3 , 500 MHz): 6.98 (s, 1H, T4), 6.52 (m, vinyl), 5.51 (d, $J=11\text{Hz}$, 0.01H, vinyl), 5.12 (d, $J=11\text{Hz}$, 0.01H, vinyl), 2.80 (m, 1.9H, Hex1 (regular)), 2.58 (m, 0.1H, Hex1(irregular)), 1.69 (m, 2H, Hex2), 1.40 (m, 6H, Hex3-5), 0.91 (m, 3H, Hex6)

^{13}C - NMR (δ , 20°C, CDCl_3 , 125 MHz): 139.9 (1C, T3), 133.67 (1C, T5), 130.5 (1C, T4), 128.6 (1C, T2), 31.7 (1C, Hex1), 30.5 (1C, Hex2), 29.3 (2C, Hex3-4), 22.7 (1C, Hex5), 14.1 (1C, Hex6)

GPC analysis of the chloroform fraction: PDI = 1.25, $M_n=11840$ g/mol, $M_w=11840$ g/mol; MALDI MS (m/z): 3598.47 (calcd. 3598.65; DP of 21; Br/vinyl and H/vinyl end groups)

Syntheses of BC2 and BC3

3 (37.3mg, 0.18 mmol) was dissolved under stirring in anhydrous dichloromethane in the glovebox. Then the Grubbs catalyst (3rd generation) (6mg, 0.0085 mmol) was added, after dissolving it in 0.5 mL anhydrous dichloromethane, via syringe. After complete consumption of the monomer, monitored by TLC, **P3** (100 mg, 0.0085 mmol) was added in one portion. For the preparation of **BC2** the reaction solution was stirred over night at room temperature. **BC3** was prepared in the same way with the only difference that the solution was heated to 40°C.

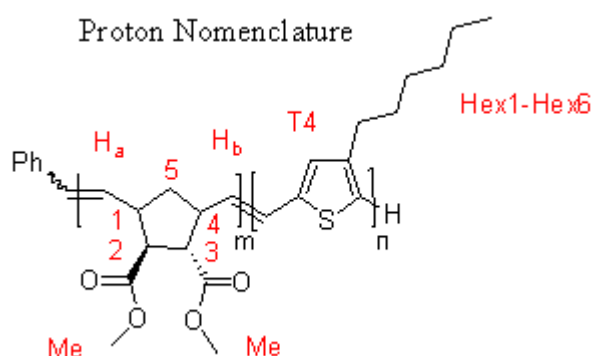
Then the reactions were quenched by the addition of 2 drops ethylvinylether and further stirring for 30 minutes. The obtained reaction solutions were concentrated by solvent evaporation under reduced pressure. Afterwards the polymers were precipitated in cold methanol. Filtration and drying in vacuum afforded the reaction products.

BC2: ^1H - NMR (δ , 20 °C, CDCl_3 , 500 MHz): 6.98 (s, 8H, T4), 5.10-5.55 (m, 2H, H_a , H_b), 3.65 (m, 6H, Me), 3.45-2.40 (m, 22H, 1, 2, 3, 4, Hex1), 1.80-1.01 (m, 106H, 5, Hex2-Hex5), 0.91 (t, 41H, Hex6)

BC3: ^1H - NMR (δ , 20 °C, CDCl_3 ,

500 MHz): 6.98 (s, 2H, T4), 5.10-5.55 (m, 2H, H_a , H_b), 3.65 (m, 6H, Me), 3.45-2.40 (m, 6H, 1, 2, 3, 4, Hex1), 1.80-1.01 (m, 24H, 5, Hex2-Hex5), 0.91 (t, 9H, Hex6)

GPC analysis of **BC2**: PDI = 1.31, $M_n=9000$ g/mol, $M_w=11750$ g/mol; GPC analysis of **BC3**: PDI = 1.38, $M_n=8260$ g/mol, $M_w=11420$ g/mol;



Synthesis of BC1

The synthesis of **BC1** was performed in the same way with the same masses of reagents with the only difference that prior to the addition of the catalyst both monomers were dissolved in anhydrous dichloromethane.

^1H - NMR (δ , 20 °C, CDCl_3 , 500 MHz): 6.98 (s, 3H, T4), 5.10-5.55 (m, 2H, H_a , H_b), 3.65 (m, 6H, Me), 3.45-2.40 (m, 9H, 1, 2, 3, 4, Hex1), 1.80-1.01 (m, 35H, 5, Hex2-Hex5), 0.91 (t, 14H, Hex6); GPC analysis: PDI = 1.34, M_n =9350 g/mol, M_w =12550 g/mol;

2.3.2.3 Polymerization using GRIM with allylic end groups

Synthesis of P4

2,5-dibromo-3-hexylthiophene (750 mg, 2.3 mmol, 20 eq) was dissolved in THF (abs., 15 mL). *Tert*-BuMgBr (1.13 mL, 2.3 mmol, 20 eq) was added via syringe and the mixture was refluxed for 6 hours. After cooling the reaction mixture to room temperature, Ni(dppp)Cl₂ (124.6 mg, 0.115 mmol, 1 eq), dissolved in THF, was added. Then the reaction mixture was stirred for 10 minutes at room temperature, before allylmagnesium bromide (1.12 mL, 50 mol% of monomer) was added via syringe to the reaction mixture. After stirring for further 10 minutes the reaction mixture was then poured into methanol to precipitate the polymer. **P4** was filtered into an extraction thimble and was then purified by Soxhlet extraction with methanol, hexane and chloroform.

^1H - NMR (δ , 20 °C, CDCl_3 , 500 MHz): 6.98 (s, 14H, T4), 5.97 (m, 1H; H_b), 5.12 (ddd, 2H, H_c), 3.50 (d, J =6.3 Hz, 2H, H_a), 2.80 (m, 24H, Hex1 (regular)), 2.58 (m, 4H, Hex1(irregular)), 1.69 (m, 28H, Hex2), 1.40 (m, 84H, Hex3-5), 0.91 (m, 42H, Hex6)

^{13}C - NMR (δ , 20°C, CDCl_3 , 125 MHz): 139.9 (1C, T3), 133.67 (1C, T5), 130.5 (1C, T4), 128.6 (1C, T2), 31.7 (1C, Hex1), 30.5 (1C, Hex2), 29.3 (2C, Hex3-4), 22.7 (1C, Hex5), 14.1 (1C, Hex6)

GPC analysis: PDI = 1.15, M_n =3310 g/mol, M_w =3810 g/mol

MALDI MS (m/z): 1782.86 (calcd. 1782.84; DP of 10; Br/allyl and H/allyl end groups)

Syntheses of BC5 and BC6

P4 (31.5 mg, 0.15 mmol) was dissolved under stirring in anhydrous dichloromethane in the glovebox. Then the Grubbs catalyst (3rd generation) (10.9 mg, 0.015 mmol) was added, after dissolving it in 0.5 mL dichloromethane, via syringe. After complete

consumption of the monomer, monitored by TLC, **3** (50 mg, 0.015 mmol) was added in one portion. For the preparation of **BC5** the reaction solution was stirred over night at room temperature. **BC6** was prepared in the same way with the only difference that the solution was heated to 40°C. Then the reactions were quenched by the addition of 2 drops ethylvinylether and further stirring for 30 minutes. The obtained reaction solutions were concentrated by solvent evaporation under reduced pressure. Afterwards the polymers were precipitated in cold methanol. Filtration and drying in vacuum afforded the reaction products.

BC5: ^1H - NMR (δ , 20°C, CDCl_3 , 500 MHz): 9.86 (s, 0.07H, aldehyde side chain), 6.98 (s, 9H, T4), 5.10-5.55 (m, 0.5H, H_a , H_b), 3.65 (m, 6H, Me), 3.45-2.40 (m, 19H, 1,2,3,4,Hex1), 1.80-1.01 (m, 90H, 5, Hex2-Hex5), 0.91 (t, 33H, Hex6)

BC6: ^1H - NMR (δ , 20°C, CDCl_3 , 500

MHz): 9.86 (s, 0.07H, aldehyde side chain), 6.98 (s, 3H, T4), 5.10-5.55 (m, 2H, H_a , H_b), 3.65 (m, 6H, Me), 3.45-2.40 (m, 8H, 1,2,3,4,Hex1), 1.80-1.01 (m, 33H, 5, Hex2-Hex5), 0.91 (t, 12H, Hex6)

Synthesis of **BC4**

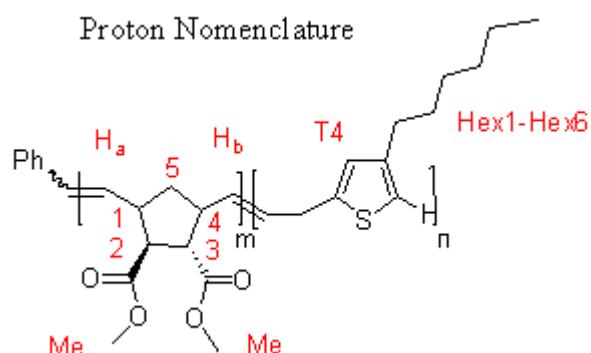
The synthesis of **BC4** was performed in the same way with the only difference that prior to the addition of the catalyst both monomers were dissolved in anhydrous dichloromethane.

^1H - NMR (δ , 20 °C, CDCl_3 , 500 MHz): 6.98 (s, 7H, T4), 5.10-5.55 (m, 1H, H_a , H_b), 3.65 (m, 6H, Me), 3.45-2.40 (m, 16H, 1,2,3,4,Hex1), 1.80-1.01 (m, 76H, 5, Hex2-Hex5), 0.91 (t, 26H, Hex6)

2.3.2.4 Comblike block copolymers

Synthesis of **P5**

2,5-dibromo-3-hexylthiophene (750 mg, 2.3 mmol, 15eq) was dissolved in THF (abs., 15 mL). *Tert*-BuMgBr (1.13 mL, 2.3 mmol, 15eq) was added via syringe and the mixture was refluxed for 6 hours. After cooling the reaction mixture to room



temperature, Ni(dppp)Cl₂ (83.1 mg, 0.153 mmol, 1eq), dissolved in THF, was added. The reaction mixture was stirred for 10 minutes at room temperature, then allylmagnesium bromide (1.12 mL, 50 mol% of monomer) was added via syringe to the reaction mixture. After stirring for further 10 minutes the reaction mixture was poured into methanol to precipitate the polymer. The precipitate was filtered into an extraction thimble and was then washed by Soxhlet extraction with methanol, hexane and chloroform.

¹H - NMR (δ, 20°C, CDCl₃, 500 MHz): 6.98 (s, 8H, T4), 5.97 (m, 1H; H_b), 5.12 (ddd, 2H, H_c), 3.50 (d, J=6.3 Hz, 2H, H_a), 2.80 (m, 16H, Hex1), 1.69 (m, 16H, Hex2), 1.40 (m, 48H, Hex3-5), 0.91 (m, 24H, Hex6)

¹³C - NMR (δ, 20°C, CDCl₃, 125 MHz): 139.9 (1C, T3), 133.67 (1C, T5), 130.5 (1C, T4), 128.6 (1C, T2), 31.7 (1C, Hex1), 30.5 (1C, Hex2), 29.3 (2C, Hex3-4), 22.7 (1C, Hex5), 14.1 (1C, Hex6)

GPC analysis hexane fraction: PDI = 1.46, M_n=1680 g/mol, M_w=2460 g/mol;
chloroform fraction: PDI = 1.19, M_n=5190 g/mol, M_w=6150 g/mol

MALDI MS (m/z): 1118.50 (calcd. 1118.45; DP of 6; Br/allyl and H/allyl and minor traces of allyl/allyl end groups)

FTIR: 3825-3117(w), 2956(s), 2928(s), 2857(s), 1640(w), 1517(w), 1465(m), 1377(m), 1261(m), 1201(w), 1095(m), 1020(m), 915(w), 825(m), 801(m)

Synthesis of P6^[61]

P5 (500 mg, 0.3 mmol) was dissolved in THF (abs., 40 mL) under argon atmosphere. To the reaction solution a 0.5 M solution of 9-BBN (6mL, 3 mmol, 10 eq) in THF (abs.) was added via syringe. The reaction mixture was stirred for 24 hours at 40°C. TLC (Cy/EE=5/1, silica) showed that a lot of educt was still present. Therefore, 5 mL of 9-BBN (2.5 mmol, 8.3 eq) were added and the reaction was allowed to further stir for 24 hours. After most of the starting material was consumed, 3.5 mL NaOH (5M) were added to the reaction mixture. After stirring for further 15 minutes the solution was allowed to cool to room temperature. After that 3.5 mL of hydrogen peroxide (30%) were added and the reaction was stirred at 40°C over night. Then the solvent was removed by rotary evaporation. The crude reaction product was dissolved in dichloromethane (30 mL) and extracted with water several times. The red-colored

⁶¹ Iovu, M.C., Craley, R., Jeffries-EL, M., Krankowski, A.B., Zhang, R., Kowalewski, T., McCullough, R.D. *Macromolecules* **2007**, 40, 4733

organic phase was concentrated by solvent evaporation under reduced pressure. Finally the product was precipitated in cold methanol. Filtration and drying under reduced pressure afforded the product with a yield of 89%.

^1H - NMR (δ , 20 °C, CDCl_3 , 500 MHz): 6.98 (s, 8H, T4), 3.75 (t, $J=6.2$ Hz, 1H; H_c), 2.86 (m, 1H, H_a), 1.94 (m, 1H, H_a), 2.80 (m, 16H, Hex1), 1.94 (m, 1H, H_b), 1.69 (m, 16H, Hex2), 1.40 (m, 48H, Hex3-5), 0.91 (m, 24H, Hex6)

MALDI MS (m/z): 1302.6 (calcd. 1302.5; DP of 7; Br/hydroxypropyl and H/hydroxypropyl)

FTIR: 3825-3004(vs), 2956(s), 2927(s), 2856(s), 1641(s), 1632(w), 1458(m), 1378(m)

Synthesis of 5

P6 (180 mg, 0.15 mmol, 2.1eq) was dissolved in 10 mL of anhydrous dichloromethane under argon atmosphere. Then 30 μL of pyridine (0.3 mmol, 4.5 eq) were added to the reaction solution. After the addition of *endo*, *exo*[2.2.1]bicyclo-hept-5-ene-2,3-dicarboxylic acid chloride (12 μL , 0.07 mmol, 1eq) the reaction was stirred over night at room temperature. TLC (Cy/EE=20/1, silica) showed complete consumption of the educt. The reaction solution was extracted with HCl (5%) and NaHCO_3 (sat.). The combined organic layers were dried over sodium sulfate. Then the solvent was removed under reduced pressure. The crude product was purified by column chromatography (Cy/EE=20/1 on silica) to give the product with 63% yield.

^1H - NMR (δ , 20 °C, CDCl_3 , 500 MHz): 6.98 (s, 18H, T4), 6.30 (dd, $J=5.2$ Hz, $J_2=8.4$ Hz, 1H, bi5), 6.08 (m, 1H, bi6), 4.19 (m, 3H), 3.28 (m, 1H), 3.14 (m, 1H), 2.80 (m, 42H, Hex1) 1.70-0.8 (m, 260H)

FTIR: 3825-3117(w), 3063(w), 2956(s), 2927(s), 2856(s), 1733(m), 1465(m), 1378(m), 1308(w), 1263(m), 1179(m), 1108(m), 1021(m), 826(m), 803(m)

Synthesis of BC7

5 (17 mg, 6.5 μmol) was dissolved in 5 mL of anhydrous dichloromethane in the glove box under nitrogen atmosphere. Then the Grubbs catalyst (3rd generation, 0.25 mg, 0.3 μmol) was dissolved in 1 mL of the same solvent and added in one portion to the reaction solution. The mixture was stirred over night at room temperature. TLC (Cy/EE=20/1, silica) showed complete consumption of the monomer. Therefore the reaction was quenched by the addition of 3 drops ethylvinylether. After further stirring for 10 minutes the solution was concentrated under reduced pressure. Then the concentrated solution was precipitated in MeOH. The polymer was allowed to settle down over night. After filtration and drying under reduced pressure the red polymer was obtained with 76% yield.

¹H - NMR (δ , 20 °C, CDCl₃, 500 MHz): 6.98 (s, 5H, T4), 5.57-5.12 (m, 1H, main chain double bond), 4.12 (m, 1H), 3.47-2.90 (m, 1H, cp1-4), 2.80 (m, 12H, Hex1), 1.96 (m, 2H, cp5), 1.69 (m, 12H, Hex2), 1.48-1.12 (43H, Hex3-5), 0.90 (s, 18H, Hex6)

GPC analysis: PDI = 2.81, M_n =4250 g/mol, M_w =11950 g/mol

Synthesis of BC8

Di-*tert*-butyl bicyclo[2.2.1]hept-5-ene-2,3-dicarboxylate (107.3 mg, 365 μmol , 200 eq) was dissolved in anhydrous dichloromethane in the glove box under nitrogen atmosphere. Then the Grubbs catalyst (3rd generation, 1.32 mg, 1.8 μmol , 1 eq) was dissolved in 1 mL of the same solvent and added in one portion to the reaction solution. After that the reaction solution was stirred over night. The complete consumption of the monomer was shown by TLC (Cy/EE=20/1). In the next step **5** (47.4 mg, 18 μmol , 10 eq) was dissolved in 5 mL dichloromethane and added to the reaction solution in one portion. Then the reaction solution was allowed to further stir at room temperature for 20 hours. Quenching of the reaction was achieved by the addition of 10 drops ethylvinylether and stirring for 45 minutes. Then the solution was concentrated under reduced pressure. Precipitation of the concentrated solution in 150 mL cold MeOH afforded the red polymer with a yield of 51% after filtration and drying under reduced pressure.

¹H - NMR (δ , 20 °C, CDCl₃, 500 MHz): 6.98 (s, 1H, T4), 5.57-5.12 (m, 2H, main chain double bond), 4.12 (m, 1H), 3.30-2.30 (m, 6H, cp1-4, Hex1), 1.85 (m, 1H, cp5), 1.56 (m, 2H, Hex2), 1.35 (s, 18H, *tert*-butyl) 1.29-1.15 (m, 8H, Hex3-5), 0.83 (s, 4H, Hex6)

GPC analysis: PDI = 6.75, M_n =4400 g/mol, M_w =29710 g/mol

3 Poly(9,9-dioctylfluorene-co-bithiophene) and Derivates

3.1 Introduction

Another interesting group of conductive polymers are poly(9,9-dialkylfluorenes). This class of material has been investigated mainly due to the promising photoluminescence properties, high hole mobilities, good film formation properties and chemical stability. This intensive research was mainly governed by the field of organic light emitting materials. Nevertheless the large optical band gap of 3.7 eV, which is too high for efficient solar photon absorption is a disadvantage for the use in solar cells. For this reason several copolymers have been synthesized in the past with the aim of an optimized band gap. One of the main strategies was the incorporation of electron rich monomer units in the main chain. The resulting polymers are also known as donor acceptor polymers. Two of the most prominent examples, poly(9,9-dioctylfluorene-co-bithiophene) (F8T2) and poly(9,9-dioctylfluorene-co-thieno[3,2-b]thiophene) (F8TT) are depicted in Figure 35.

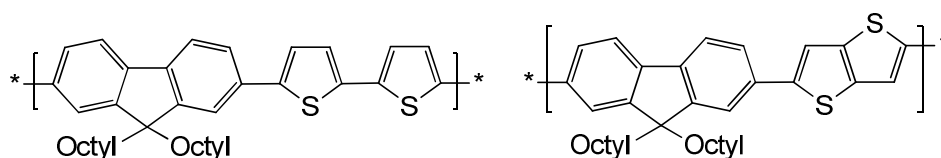


Figure 35. Chemical structures of F8T2 and F8TT.

The fluorene unit itself is electron deficient. This interaction of a donor and an acceptor monomer in the same main chain leads to a reduction in the optical band gap as illustrated in Figure 36. The high lying HOMO of the donor unit and the low lying LUMO of the acceptor unit, in combination with an intramolecular charge transfer, results in the reduced optical band gap.

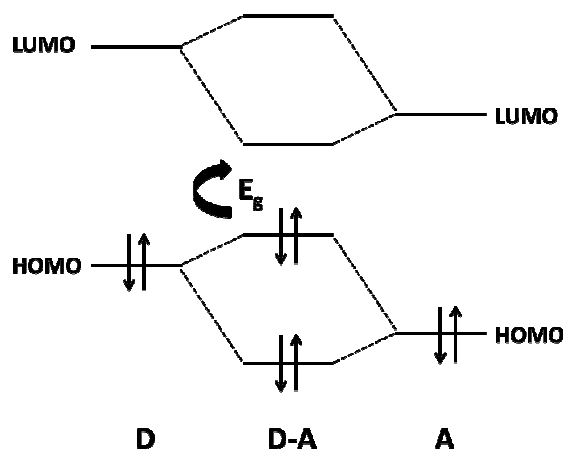


Figure 36. Interaction of front orbitals in donor-acceptor systems.

According to the perturbation theory, the interaction of the two LUMOs and HOMOs leads to the formation of four new orbitals. After redistribution of the electrons these newly hybridized orbitals have a higher lying HOMO and a lower lying LUMO, which results in a reduced band gap, as shown in Table 4.^[62]

Table 4. Comparison of front orbitals and band gaps of poly(9,9-dioctylfluorenes), F8T2 and F8TT.

Polymer	HOMO [eV]	LUMO [eV]	E _g [eV]
polyfluorene	-5.8	-2.12	3.68
F8T2	-5.41	-2.48	2.93
F8TT	-5.38	-2.40	2.98

Especially F8T2 (**P1**) gained a lot of interest in combination with PCBM as the acceptor material in organic solar cells. Kuo-Chuan Ho et al.^[12] showed that the crystallinity of F8T2 is strongly dependent on the applied annealing temperature in this type of cells. This dependence is due to the structure of the polymer which leads to thermotropic liquid crystalline behavior. The crystalline nanodomains of F8T2 are increasing from 30-40 nm by annealing the films at 100°C to 70-80 nm by applying temperatures of 250°C. At 100°C the formation of a bicontinuous network is possible based on the dispersion of the nanodomains in the film, whereas at 250°C rather big clusters of PCBM, surrounded by the polymer are observable.^[62] In terms of device performance

⁶² Lim, E.; Jung, B.; Shim, H.-K. *Macromolecules* **2003**, 36,4288

large polymer domains are disadvantageous because of the higher degree of recombination of excitons within these domains. This finding was also confirmed by current density-voltage plots of devices, annealed at different temperatures which showed lower current densities when elevated temperatures were used. Best device performance was observed at an annealing temperature of 70°C. By applying higher temperatures the voltage as well as the current density decreases.

Having PCBM as acceptor material, rather low annealing temperatures can be used without disadvantages. However, for systems where the acceptor phase is formed in-situ during the annealing step from precursor materials which decompose by applying thermal energy, the use of low temperatures in the annealing step would lead to a poorly defined acceptor phase and as a consequence of that to a poor device performance. Hence another strategy has to be followed to decrease the crystallization tendency for such systems. In general, the crystallinity of a polymer strongly depends on the arrangement of individual polymer chains in the film. Concerning alternating fluorene-bithiophene copolymers it can be governed within certain limits by the sidechains on the fluorene unit. In general, the interpenetration of the sidechains will be hindered if they are branched, which leads to a higher interplanar distance of two neighboring polymer chains.

In this work, this strategy was used in polymer **P2**, where 2-ethylhexyl sidechains were used instead of octylchains (see Figure 37). Another way to increase this distance is to use two fluorene monomers with different sidechains. Due to the polymerization method, a polycondensation, fluorene and bithiophene monomers are alternating incorporated in the main chain. The statistic incorporation of the two different fluorenes breaks the symmetry of the sidechains, which leads to an increase of the interplanar distance. Based on this idea, in polymer **P3** a fluorene with 2-ethylhexyl sidechains and one with octyl sidechains was used. Both strategies are, together with the chemical structures, schematically depicted in Figure 37. All three polymers were synthesized and characterized by differential scanning calorimetry (DSC) to get information about the thermal properties. Additionally, photophysical measurements were performed to investigate the aggregation behavior.

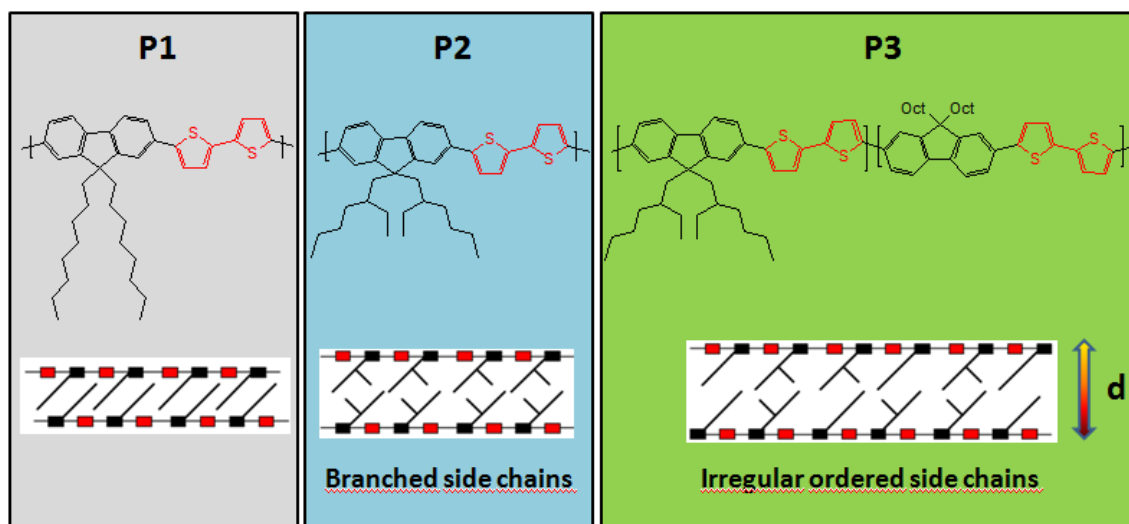


Figure 37. Chemical structures and schematic illustration of the strategies to increase the in-planar distance.

3.2 Synthesis by Suzuki Polycondensation

The Suzuki polycondensation reaction is one of the most researched methods which produce carbon-carbon bonds. This is based on the fact that the reaction proceeds under milder conditions and more efficiently as compared, for example, to Yamamoto coupling.^[63] The early beginnings of this type of reaction date back to 1979^[64] and were honored in 2010 with the Nobel prize. The monomers, used in this reaction, are known to be easy to handle and are stable towards oxygen and moisture, which is another advantage responsible for the popularity of this method. The overall reaction connects monomers with halide groups to monomers bearing an organoboron functionality. The catalytic cycle for the cross coupling reaction, using a palladium catalyst and a base, is depicted in Figure 38.

⁶³ Yamamoto, T.; Hayashi, Y.; Yamamoto, Y. *Bull.Chem.Soc.Jpn.* **1978**, 51, 2091

⁶⁴ Miyaura, N.; Yamada, K.; Suzuki, A. *Tetrahedron Lett.* **1979**, 3437

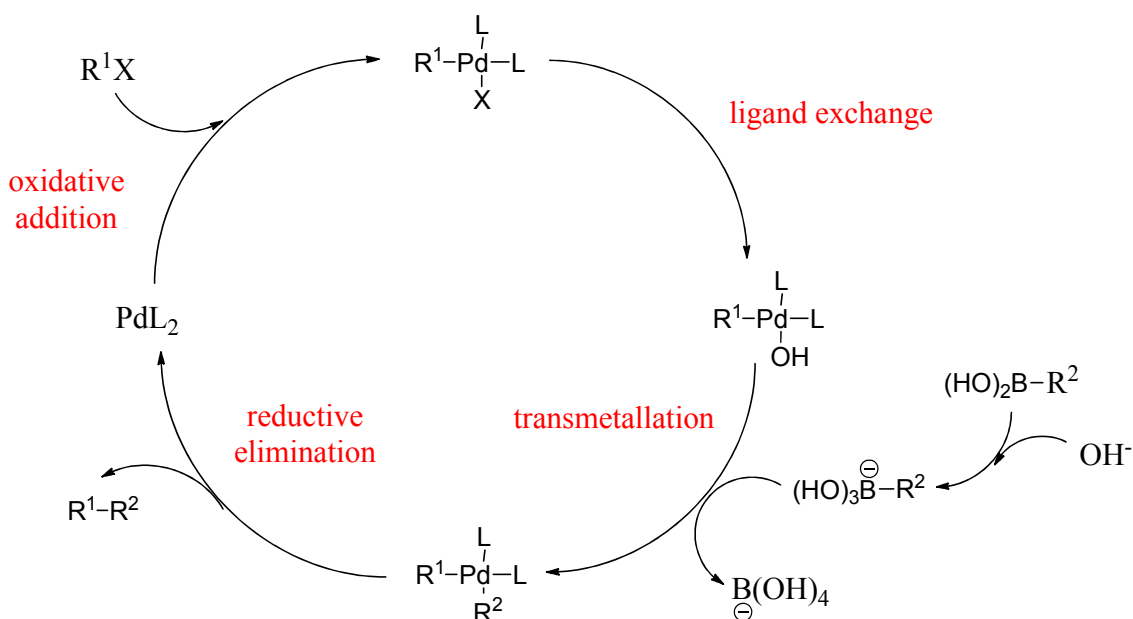


Figure 38. Schematic representation of the catalytic cycle involved in Suzuki-type reactions.

The main steps in the catalytic cycle are the oxidative addition, transmetalation followed by a reductive elimination to recover the active palladium species again. The role of the base in the reaction is mainly to accelerate the reaction by the formation of a negatively charged boron compound with increased nucleophilic character.^[65]

3.3 Results and Discussion

3.3.1 Synthesis

The synthesis schemes of the polymers **P1-P3**, using Suzuki polycondensation, are depicted in Figure 39 and Figure 40.

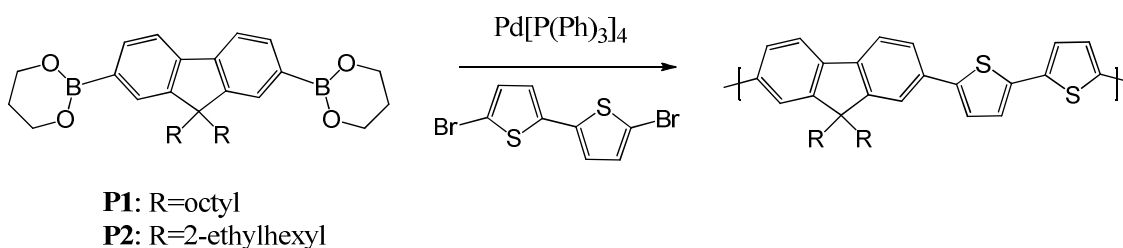


Figure 39. Synthesis scheme for polymers **P1** and **P2**.

⁶⁵ Suzuki, A. *Chemical Communications*, **2005**, 38, 4759

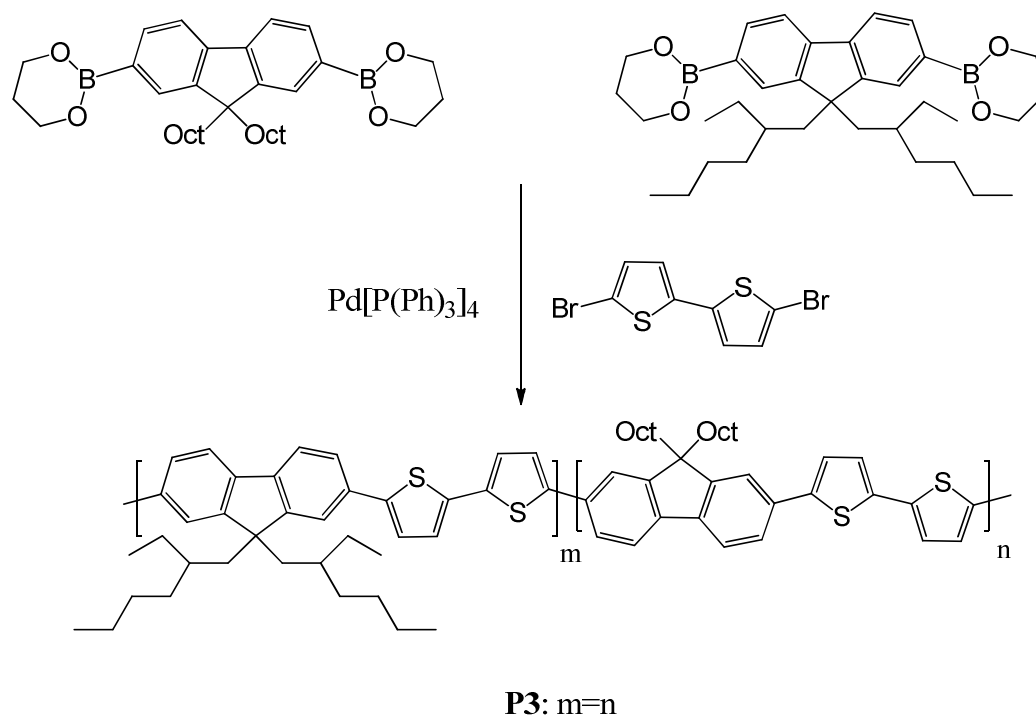


Figure 40. Synthesis scheme for polymer **P3**.

For the polymerization the monomers were dissolved in anhydrous toluene. Then the phase transfer catalyst, *N*-Methyl-*N,N*-dioctyloctan-1-ammonium chloride (Aliquat 336) was added. The role of this reagent is to ensure the transfer of hydroxide ions from the water phase to the organic phase, which ensures enhanced reactivity in the transmetalation, as was already mentioned in Chapter 6.3. This was followed by deaeration for 40 minutes by purging with argon. Meanwhile a solution of sodium carbonate (2M) was prepared and also deaerated for 30 minutes. In the next step tetrakis(triphenylphosphine)-palladium was added to the combined solution. The reaction mixture was vigorously stirred at 90°C for 48 hours. To provide defined end groups 0.05 eq of the corresponding monomer, bearing the boronic ester group and 0.1 eq of bromobenzene were added. After stirring further 2 hours, the polymers were precipitated in MeOH. Filtration afforded the crude product which was dissolved in chloroform and extracted three times with water to remove the alkali components. The organic phase was dried over sodium sulfate, and after removing the solvent by rotary evaporation, the product was once again dissolved in a small volume of chloroform. Then the polymers were precipitated in MeOH, collected by filtration and dried under reduced pressure. Finally the polymers were purified by Soxhlet extraction in acetone for 1 day to remove low molecular weight oligomers.

These polymers were characterized by NMR and GPC. In order to investigate the crystallization behavior, differential scanning calorimetry (DSC) measurements were made in addition to the photophysical characterization of the polymers in solution and in thin films.

3.3.2 Characterization

The ^1H - NMR spectra of the obtained polymers do not differ significantly. The peaks of the polymers are identical to the ones already known from literature.^[66] In general, the information content of these polymers concerning their NMR spectra is relative low. The GPC data are listed in the Table below.

Table 5. GPC data of the polymers **P1-P3** in THF as solvent.

	P1	P2	P3
M_n [g/mol]	29700	13300	10850
M_w [g/mol]	140700	23400	32250
PDI	4.73	1.77	2.97

As can be seen from the data, **P1** has compared to **P2** and **P3** a higher molecular weight. Also the PDI of **P1** differs significantly from the two other polymers.

3.3.3 DSC measurements

In order to investigate the thermal properties of the polymers **P1-P3**, DSC measurements were performed. The heating curve of the third heating run, performed with a scan rate of 40°C/min, for polymer **P1** is shown in Figure 41.

In accordance with the literature^[67] different phase transitions, observable through a release or intake of thermal energy, were observed. The polymer undergoes a glass transition at a temperature of 110°C, which is followed by a cold crystallization at a temperature of 159°C. In the higher temperature range two transitions, typical for liquid crystalline polymers can be observed. The first occurs at a temperature of 249°C and can be attributed to a transition from the solid state to the mesophase. The transition to

⁶⁶ Lim, E.; Jung, B.; Shim, H.-K. *Macromolecules* **2003**, *36*, 4288-4293.

⁶⁷ Kinder, L.; Kanicki, J., Petroff, P. *Synthetic Metals* **2004**, *146*, 181

the isotropic phase occurs at a temperature of 323°C. These results confirm the assumption that F8T2 shows liquid crystalline behavior.

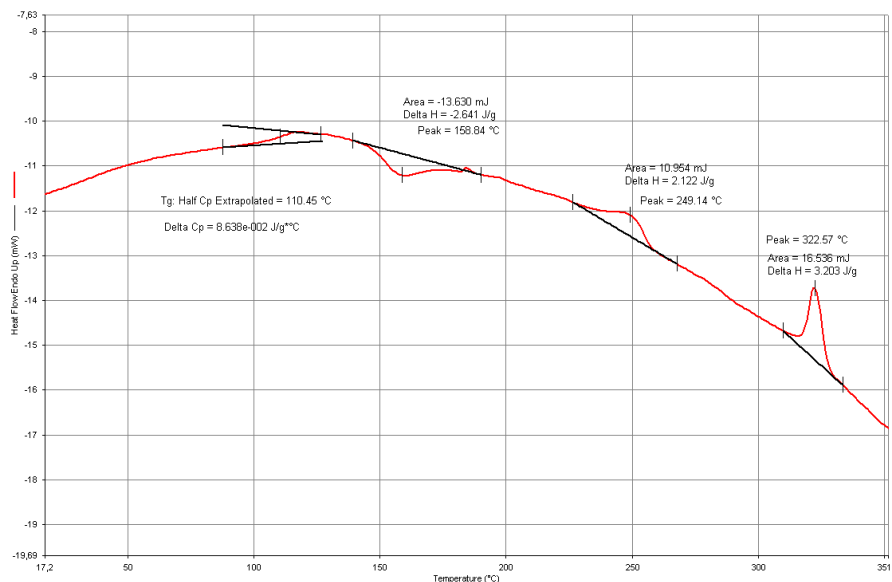


Figure 41. DSC curve of **P1**.

In Figure 42 the DSC curve for **P2** is depicted which was obtained by using the same scan rate. Contrary to **P1**, this polymer does not undergo such a complex melting behavior. The only observable signal is the glass transition, occurring at a temperature of 113°C. This means that the introduction of the branched alkyl chains effectively reduces the ability of the polymer to crystallize.

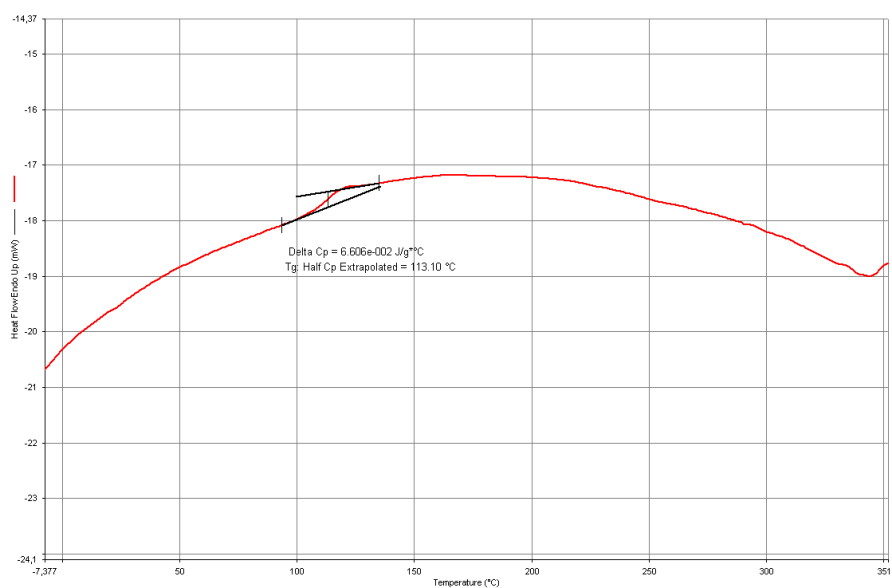


Figure 42. DSC curve of **P2**.

Polymer **P3**, depicted in Figure 43, shows complex melting behavior in the temperature range between 300°C and 350°C, in addition to the glass transition which occurs at a temperature of 111°C.

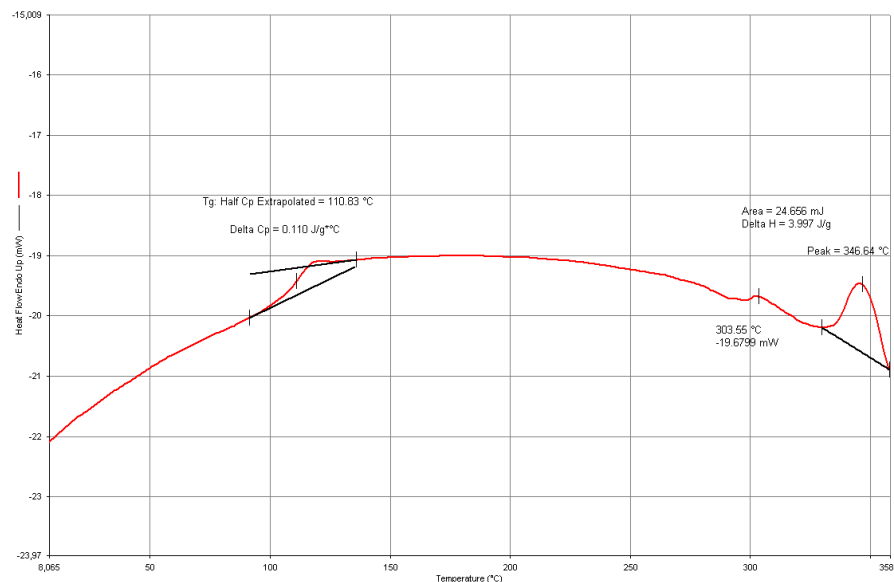


Figure 43. DSC curve of **P3**.

Two endotherm peaks can be observed. The first one occurs at a temperature of 303°C and the second one, more pronounced than the first, occurs at 347°C. Currently, this difference cannot be explained. But according to literature^[67] the existence of two melting peaks can also be observed in polymers with complex melting behavior. However, to study this effect in more detail, polarized optical microscopy would be beneficial. Concluding these measurements, a clear change in the crystallization behavior can be confirmed for both investigated strategies.

3.3.4 Photophysical characterization

Another possibility to evaluate the tendency of aggregation of conductive polymers is to compare the absorption spectra in solution and in thin films.^[68] In general, polymer molecules which tend to agglomerate exhibit absorption spectra which do not differ significantly in solution and in films. This can be explained by intermolecular π -stacking, already occurring in solution. This is in contrast to polymers with bulky side

⁶⁸ Setayesh, S.; Grimsdale, A.C.; Weil, T.; Enkelmann, V.; Müllen, K.; Meghdadi, F.; List, E.J.W.; Leising, G. *J.Am.Chem.Soc.* **2001**, 123, 946

chains (**P2**) or irregular ordered substituents (**P3**).^[68] The absorption spectra of the polymers **P1-P3** are depicted in Figure 44.

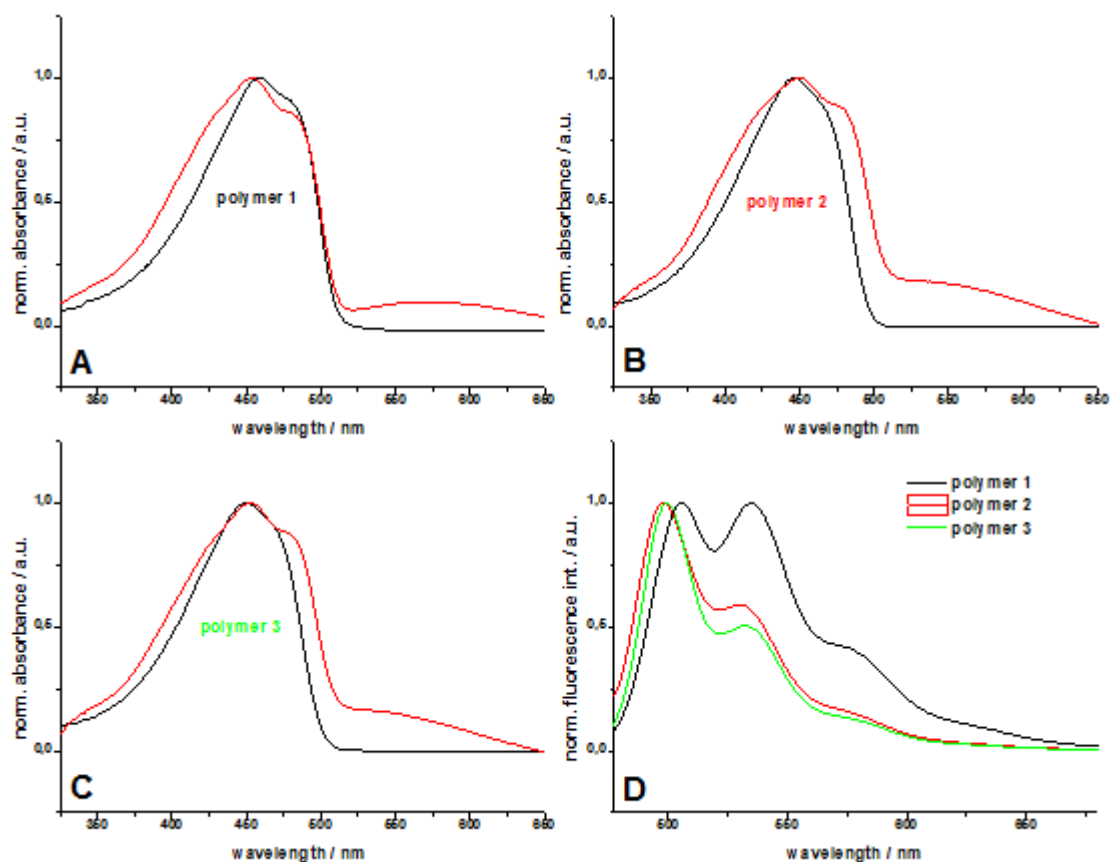


Figure 44. Summary of absorption spectra in chloroform solution ($c = 0.008$ mg/mL; black lines) and of films cast from chloroform solution ($c = 7$ mg/mL; red lines) of **P1** (A), **P2** (B) and **P3** (C); D: emission spectra of the polymers in chloroform solutions ($c = 0.004$ mg/mL; $\lambda_{\text{ex}} = 450$ nm).

As expected, the onset of the absorption spectra of the films from polymers **P2** and **P3** is red-shifted compared to their solution spectra, which indicates that π -stacking only occurs in the films. Compared to these polymers, the onset of polymer **P1** remains unchanged. The absorption maxima in solution and in the films are depicted in Table 6. The data show a clear red shift of 13 nm of **P1** in the absorption maximum, in comparison to **P2**. The maximum of **P2** and **P3** is centered at 446 and 449 nm, whereas the maximum of **P1** is at 459 nm. In addition, also the shoulder in the absorption, which can be attributed to a poorly resolved vibronic peak is at 481 nm for polymer **P1** and therefore 14 nm red shifted compared to polymer **P2**. However, the corresponding film spectra exhibit peak maxima which are only slightly shifted. This indicates that all three

polymers tend to intermolecular aggregation in the solid state. The bathochromic shifted, broad and structureless absorption peaks, observable for all three polymers can be attributed to interference fringes of the thin films.^[69] This assumption was confirmed by the casting of thinner films, which showed a shift of this peak. In Figure 44 (D) the emission spectra of the polymers in solution are depicted. Also the emission of polymer **P3** is compared to the two other polymers redshifted. The corresponding emission maxima of the different vibronic peaks are listed in Table 6. One other interesting point concerning the emission spectra is the relative intensity of the transition from the excited state to different vibrational levels of the ground state. As can be seen the 0-0 transition of the polymers **P2** and **P3** is compared to the 0-1 and 0-2 transition dominant. In contrast to these, polymer **P1** exhibits an emission with equal intensity of the 0-0 and the 0-1 transition. This difference can be explained by the higher molecular weight of polymer **P1**. The number of possible vibrational modes is proportional to the chain length of the polymer.^[70] This higher vibrational degree of freedom leads to a stronger shifting of the excited state of a molecule compared to its ground state.^[71] As a consequence, higher vibrational transitions become more probable.

To sum up, the comparison of the absorption spectra obtained from solutions and from thin films is an excellent method in evaluating the tendency of polymers to agglomerate. It was demonstrated that this tendency can be reduced, through the introduction of distortions in the side chain

Table 6. Summary of the absorption and emission data of the polymers **P1-P3**.

Polymer	CHCl ₃ -solution	films cast from CHCl ₃	Emission		
	Abs, λ_{MAX} (shoulder)	Abs, λ_{MAX} (shoulder)	0-0	0-1	0-2
	[nm]	[nm]	λ_{MAX} [nm]		
1	459 (481)	454 (481)	505	535	575
2	446 (467)	449 (478)	498	530	---
3	449	452 (479)	499	532	---

⁶⁹ Ziegler, E.; Pein, A.; Fischereder, A.; Trimmel, G. *Monatsh.Chem.* **2011**, 142, 193

⁷⁰ Grey, J.K.; Kim, D.Y.; Donley, C.L.; Miller, W.L.; Kim, J.S.; Silva, C.; Friend, R.H.; Barbara, P.F. *J.Phys.Chem.B* **2006**, 110, 18898

⁷¹ Ariu, M.; Sims, M.; Rahn, M.D.; Hill, A.M.F.; Lidzey, D.G. *Physical Review B* **2003**, 67, 195333

3.3.5 Experimental

Typical Synthesis Procedure (P1)

For the polymerization the monomers, 2-(2-(1,3,2-dioxaborinan-2-yl)-9,9-dioctyl-9H-fluoren-7-yl)-1,3,2-dioxaborinane (750 mg, 1.35 mmol) and 2-bromo-5-(5-bromothiophen-2-yl)thiophene (435.3 mg, 1.35 mmol) were dissolved in 30 mL of anhydrous toluene. Then 50 μ L of the phase transfer catalyst, Aliquat 336 were added, followed by deaeration for 40 minutes by purging with argon. Meanwhile 6 mL of sodium carbonate (2M) were prepared which were deaerated for 30 minutes. In the next step tetrakis(triphenylphosphine)-palladium (15.53 mg, 1 mol%) was added to the combined solutions. The reaction mixtures were vigorously stirred at 90°C for 48 hours. To provide defined end groups the fluorene monomer (37.5 mg, 0.05 eq), and bromobenzene (20 μ L, 0.1 eq) were added. After stirring for further 2 hours, the polymer was precipitated in MeOH. Filtration afforded the crude products which were dissolved in chloroform and extracted three times with water to remove the alkali components. The organic phase was dried over sodium sulfate and after removing the solvent by rotary evaporation the product was once again dissolved in a small volume of chloroform. Afterwards the polymer was precipitated in MeOH, collected by filtration and dried under reduced pressure. Finally, the polymers were further purified by Soxhlet extraction in acetone for 1 day to remove low molecular weight oligomers.

^1H - NMR (δ , 20 °C, CDCl_3 , 500 MHz): 7.65-6.80 (m, 10H), 2.02 (br, 4H), 1.06 (br, 20H), 0.80 (m, 10H)

GPC analysis: PDI = 4.73, M_n =29700 g/mol, M_w =140700 g/mol

The synthesis of **P2** followed the synthesis procedure described for **P1**. Although the absolute masses were different, the same ratios of monomers and solvents were used. **P3** was also synthesized following the described procedure. However, for this polymer the ratio of the two fluorene derivates and the bithiophene moiety was 1/1/2.

P2

^1H - NMR (δ , 20 °C, CDCl_3 , 500 MHz): 7.65-6.79 (m, 10H), 2.02 (br, 4H), 1.06 (br, 20H), 0.80 (m, 11H)

GPC analysis: PDI = 1.77, M_n =13300 g/mol, M_w =23400 g/mol

P3

¹H - NMR (δ , 20 °C, CDCl₃, 500 MHz): 7.66-6.80 (m, 10H), 2.02 (br, 4H), 1.06 (br, 19H), 0.80 (m, 10H)

GPC analysis: PDI = 2.97, M_n =10850 g/mol, M_w =32250 g/mol

DSC measurements were made with a Perkin Elmer Pyris Diamond Differential Scanning Calorimeter equipped with a Perkin Elmer CCA7 cooling system using liquid nitrogen.^[122] A nitrogen flow of 20 mL min⁻¹ and a heating rate of 40°C/minute were used. The described transitions were taken from the third heating run.

The rest of the instrumentation for the different characterization methods was applied as described in Chapter 2.3.1.

4 Influence of residual Palladium in F8T2

Commonly, for the polymerization of F8T2 and its derivatives Suzuki-type polycondensation, using Pd-catalysts, is used. Depending on the applied work up and purification of the resulting polymers residual palladium is left in the materials. According to Björklund et al.^[72] palladium and other impurities, present in the used polymers can act as charge-trapping sites. They investigated in their work the influence of palladium and other metal impurities in polymers on the performance of field-effect transistors. However, to the best of my knowledge a similar study with hybrid solar cells has never been conducted before.

Therefore, F8T2 was synthesized, and after the standard work up of the polymer, one fraction was exposed to a metal scavenger which effectively reduces the content of palladium in the sample. These two polymers, together with a commercially available one were used in the production of organic solar cells. To simplify the work, PCBM was used as acceptor phase due to the known fact that the electron transport in this type of material is trap-free and because of the availability of literature dealing with optimizing this system.^[73] The overall performance of the obtained devices will be discussed and moreover, corresponding plots of the open circuit voltage versus the light intensity were made and are used to investigate the relative trap density.

4.1 Introduction

The principle processes involved in the production of current in hybrid solar cells were already discussed in the introduction of this work (chapter 1). The steps which are necessary to produce free charge carriers and the competing processes are depicted in Figure 45.

⁷² Björklund, N.; Lill, J.-O.; Rajender, J.; Österbacka, R.; Tierney, S.; Heeney, M.; McCulloch, I.; Cölle, M. *Organic Electronics* **2009**, 10, 215

⁷³ Huang, J.-H.; Ho, Z.-Y.; Kekuda, D.; Chang, Y.; Chu, C.-W.; Ho, K.-C. *Nanotechnology* **2009**, 20, 025202

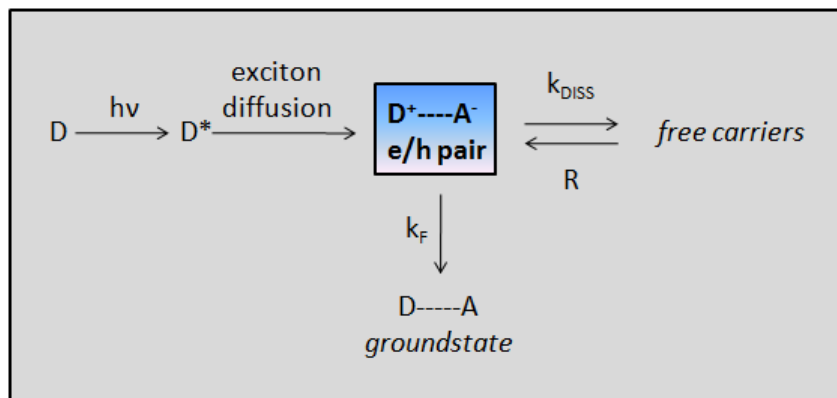


Figure 45. Schematic summary of the processes, involved in the formation of free charge carriers.

In general, an electron transfer process between the donor and the acceptor phase leads to an electron-hole pair, also called exciton. The exciton can either dissociate into free carriers^[74] or decay to its ground state. The competing mechanism of the dissociation process is bimolecular Langevin recombination, producing excitons from free carriers. The Langevin recombination rate is given by

$$R = \gamma(np - n_i p_i) \quad (5)$$

with n (p) is the free electron (hole) density, n_i (p_i) is the intrinsic electron (hole) density, and γ is the Langevin recombination constant.^[75] This recombination is governed by the sum of the electron and hole mobility. Taking into account that in the case of a blend material only the mobility of the slowest carrier dominates the recombination, the constant γ is given by

$$\gamma = \frac{q}{\epsilon} \min(\mu_n, \mu_p) \quad (6)$$

where q is the elementary charge, ϵ is the dielectric constant and $\mu_{n(p)}$ is the mobility of the electrons (holes).^[74] It has been shown and experimentally confirmed for MDMO-PPV/PCBM solar cells that a linear dependence between the V_{OC} and the light intensity exists, exhibiting a slope S of (kT/q) , under the prerequisite that Langevin

⁷⁴ Mandoc, M.M.; Kooistra, F.B.; Hummelen, J.C.; Boer, B.; Blom, P.W.M. *Appl.Phys.Lett.* **2007**, 91, 263505

⁷⁵ Langevin, P. *Ann.Chim.Phys.* **1903**, 28, 433

recombination is the only loss mechanism.^[76] In this case, the open circuit voltage of the solar cell is given by

$$V_{OC} = \frac{E_{gap}}{q} - \frac{kT}{q} \ln \left[\frac{(1-P)\gamma N_c^2}{PG} \right] \quad (7)$$

where E_{gap} is the energy difference between the highest occupied molecular orbital (HOMO) of the electron donor and the lowest unoccupied molecular orbital (LUMO) of the electron acceptor, q is the elementary charge, k the Boltzmann constant, T the temperature, P is the dissociation probability of the electron – hole pairs into free carriers, γ the recombination constant, N_c the density of states in the conduction band, and G is the generation rate of electron – hole pairs. G is the only term directly proportional with the light intensity.^[74]

However, all-polymer solar cells, using another conductive polymer as acceptor material showed a much steeper slope in the plots of V_{OC} versus light intensity.^[77] This has been explained by the existence of traps, present in the acceptor polymer. These traps make a recombination of trapped electrons in the acceptor material with holes present in the donor also possible. This recombination process does not occur in their PCBM counterpart, a material which shows trap-free electron transport.^[73]

In the presence of electron traps, the dissociation of the excitons at the interface gives rise to the formation of free charge carriers, with the difference that in this situation a part of the electrons will be trapped. For those electrons which are trapped close to the interface, recombination with holes occurs with a certain probability so that both carriers are lost. The mathematical description of this process is given by the Shockley-Read-Hall (SRH) equation^[74, 78, 79] giving the trap-assisted recombination rate:

$$R = \frac{C_n C_p N_t (pn - p_1 n_1)}{(C_n (n + n_1) + C_p (p + p_1))} \quad (8)$$

⁷⁶ Koster, L.J.A.; Mihailetschi, V.D.; Ramaker, R.; Blom, P.W.M. *Appl.Phys.Lett.* **2005**, 86, 123509

⁷⁷ Mandoc, M.M.; Veurman, W.; Koster, L.J.A.; Boer, B.; Blom, P.W.M. *Adv.Funct.Mater.* **2007**, 17, 2167

⁷⁸ Shockley, W.; Read, W.T. *Phys.Rev.* **1952**, 87, 835

⁷⁹ Hall, R.N. *Phys.Rev.* **1952**, 87, 387

where C_n and C_p are the capture coefficients of electrons and holes, respectively, N_t is the density of electron traps, n and p are the electron density in the conduction band and the hole density in the valence band, and $p_1 n_1 = N_c N_v \exp[-(E_c - E_v)/kT] = n_i^2$, with n_i the intrinsic carrier concentration in the sample.^[74] This means that in the case of trap-assisted recombination the overall recombination rate is increased by a further contribution of the trap-assisted recombination rate, which increases the slope of linear dependence between V_{OC} and the light intensity.

The decrease of the V_{OC} for trap-limited transport in the acceptor phase of solar cells is a direct result of the fact that the presence of electrons in trap levels below the LUMO of the PCBM leads to a lowering of the electron quasi-Fermi level.^[74] But not only the open circuit voltage is negatively affected by this phenomenon. Also the fill factor, and, by the additional loss of free charge carriers, the current density decrease.^[80]

4.1.1 Results and Discussion

4.1.1.1 Synthesis and purification

The synthesis of the polymer was performed in the same way as described in the previous chapter. Also in this case, the resulting polymer **P4** was characterized by NMR-spectroscopy and GPC. The only difference, compared to the polymers of the previous section is that a part of the polymer was treated with N, N, N'-trimethylethane-1,2-diamine immobilized on polystyrene (see Figure 46) to remove residual palladium giving **P5**.

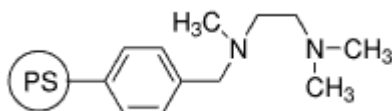


Figure 46. Schematic illustration of the palladium scavenger.

The typical procedure involves the dissolution of the polymer in anhydrous toluene followed by the addition of the palladium scavenger. Slow agitation (<100 rpm on magnetic stirrer) is enough for the polymer to adsorb residual palladium. Therefore,

⁸⁰ Koster, L.J.A.; Mihailetschi, V.D.; Blom, P.W.M. *Appl.Phys.Lett.* **2006**, 88, 052104

there was little attrition of the polymer beads in the experiment.^[81] The solution was allowed to stir at 70°C for 45 hours. After filtration the solvent was concentrated by rotary evaporation. The polymer was obtained after precipitation in MeOH, filtration, and drying under reduced pressure with a yield of 74%. The number average molecular weight, obtained by GPC analysis was 58500 g/mol. The palladium metal content of all three polymers, **P4**, **P5**, and the commercial one, **P6**, was analyzed with inductive-coupled plasma optical emission spectrometry (ICP-OES). The results are summarized in Table 7. As can be seen the cleaning procedure effectively decreases the palladium content to about one third of its initial value from 1200 µg/g to 400 µg/g. The high content of palladium in the commercial polymer was with 5600 µg/g quite surprising and confirms the need for an adequate quality control of the materials used in solar cell production.

Table 7. Pd-content of the polymers **P4-P6**.

	P4	P5	P6
Pd-content [µg/g]	1200	400	5600

4.1.2 Fabrication of solar cells

The F8T2/PCBM nanocomposite solar cells were prepared as schematically depicted in Figure 47.

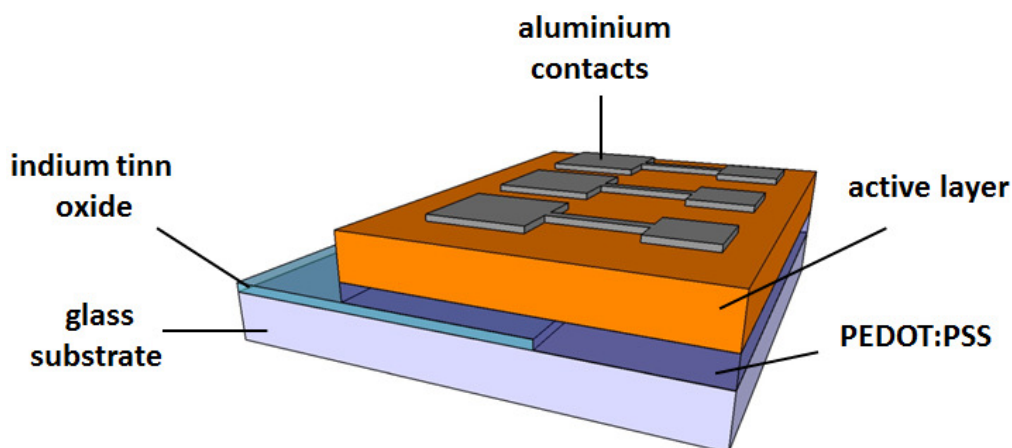


Figure 47. Schematic illustration of the prepared hybrid solar cells.

⁸¹ Urawa, Y.; Miyazawa, M.; Ozeki, N.; Ogura, K. *Organic Process Research & Development* **2003**, 7, 191

For the first optimization experiments the commercial polymer **P6** was used. The ITO covered glass substrates were coated by spin coating with PEDOT:PSS as hole conducting layer and to smooth the roughness of the ITO surface. For the first cells this additional hole conducting layer was omitted. The next layer is the active layer consisting of the mixture of F8T2 and PCBM which was stirred over night. The structures of the used materials are depicted in Figure 48. The focus of the optimization for these first substrates was put on the concentration of this layer. The best values for the ratio of donor to acceptor is already known from literature to be 1/1.^[73] The used concentrations varied between 4 and 10 mg/ml with chloroform as solvent. Two substrates of each concentration were prepared by spin coating. One substrate of each concentration was annealed on a hot plate under inert atmosphere in the glove box at a temperature of 70°C. According to the literature,^[73] this temperature turned out to be optimal. The others were used as spun. The final step in the production was the vapor deposition of alumina electrodes through shadow masks in a resistive heated vacuum chamber. The results of these first cells are summarized in Table 8.

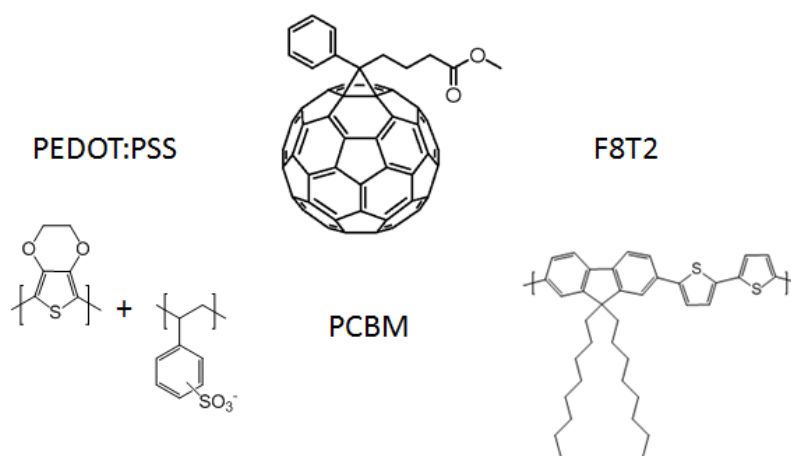


Figure 48. Overview of the used materials.

As can be clearly seen, in contrast to the literature in our case the cell performance of the as spun cells is superior compared to the annealed cells. The temperature mainly reduces the current density. The concentration of 5 mg/mL turned out to be the one which produced the highest PCE-values. However, compared to the literature with a V_{OC} of 0.93, I_{SC} of 1.89 and a FF of 50% the obtained values are rather low.

Table 8. Solar cell parameters.

c [mg/mL]	25°C				70°C			
	V_{oc} [V]	I_{sc} [mA/cm ²]	FF [%]	PCE [%]	V_{oc} [V]	I_{sc} [mA/cm ²]	FF [%]	PCE [%]
10	0.52	0.30	32.3	0.05	0.40	0.26	27.3	0.03
8	0.60	0.84	34.1	0.17	0.52	0.91	29.2	0.14
6	0.60	1.15	32.8	0.23	0.50	0.85	30.8	0.13
5	0.58	1.32	32.6	0.25	0.60	0.56	33.2	0.11
4	0.44	1.13	34.6	0.17	0.46	0.82	32.3	0.12

Therefore, in the next step a concentration of 4.5 mg/mL was used with an additional PEDOT:PSS layer. The rest of the substrate preparation was as described before, with the only difference that the annealing temperature was raised to 130°C.

The solar cell parameters of the prepared substrates are listed in Table 9. In this case all three contacts of one substrate are shown, indicating the reproducibility of the used system. As can be seen, as cast cells are superior compared to the annealed cells. Main factors which reduced the PCE values in the annealed cells are the reduced current density and the fill factor. The reason for this dramatic decrease in the device performance is the phase separation, which can occur if annealing temperatures, higher than the glass transition temperature of the polymer, are used, and the increased surface roughness.^[73]

Table 9. Solar cell parameters of cells with PEDOT/PSS intermediate layer.

25°C				130°C			
V_{oc} [V]	I_{sc} [mA/cm ²]	FF [%]	Eff. [%]	V_{oc} [V]	I_{sc} [mA/cm ²]	FF [%]	Eff. [%]
0.87	5.70	30.8	1.53	0.84	1.10	14.0	0.13
0.87	5.72	30.9	1.54	0.84	1.03	14.4	0.12
0.87	5.55	30.7	1.48	0.83	0.94	14.5	0.11

In the next step identical cells with the three different polymers, **P4**, **P5**, and **P6** were fabricated, with the only difference that the combined solutions with polymer and fullerene were stirred for only 150 minutes, in contrast to overnight stirred solutions which were used in the previous experiments. Each polymer was used in three different concentrations. This was done to investigate if the optimized concentration which was evaluated by using **P6** is also valid for **P4** and **P5** or if, owing to the different molecular weight of these polymers another concentration is beneficial. Moreover, as annealing proved to be inadequate to increase the performance, a thermal treatment was omitted in

the fabrication of the next devices. The results of the experiments are summarized in Table 10. For a better survey the polymers are listed with decreasing Pd-content. For each polymer and concentration three cells are listed with the corresponding mean of the measurements.

Table 10. Comparison of solar cell parameters for the different polymers.

Polymer	conc. mg/mL	Voc V	average	Isc mA/cm ²	average	FF %	average	PCE %	average
P6 5600ppm Pd	6.5	0.778		1.81		33.6		0.47	
		0.757	0.76	1.33	1.429	33.5	33.4	0.34	0.37
		0.746		1.14		33.1		0.28	
	5.5	0.735		1.83		35.0		0.47	
		0.704	0.721	1.55	1.673	35.7	34.7	0.39	0.42
		0.725		1.64		33.6		0.40	
	4.5	0.746		2.12		36.8		0.58	
		0.704	0.721	2.04	2.055	35.8	36.3	0.52	0.54
		0.714		2.01		36.4		0.52	
P4 1200ppm Pd	6.5	0.915		1.20		24.7		0.27	
		0.894	0.894	1.08	1.116	24.4	24.5	0.24	0.25
		0.873		1.06		24.3		0.23	
	5.5	0.883		1.30		23.1		0.27	
		0.862	0.83	1.11	1.137	22.6	23.8	0.22	0.23
		0.746		1.00		25.8		0.19	
	4.5	0.936		1.71		22.0		0.35	
		0.915	0.915	1.45	1.448	23.0	23.1	0.31	0.31
		0.894		1.18		24.3		0.26	
P5 400ppm Pd	6.5	0.925		1.25		28.6		0.33	
		0.936	0.933	1.17	1.169	26.5	27.0	0.29	0.30
		0.936		1.09		25.9		0.26	
	5.5	0.947		2.06		27.9		0.55	
		0.915	0.933	1.81	1.814	27.1	27.8	0.45	0.47
		0.936		1.57		28.3		0.42	
	4.5	0.947		2.14		29.9		0.61	
		0.947	0.943	1.98	1.931	27.8	28.3	0.52	0.52
		0.936		1.67		27.1		0.42	

As can be seen for **P6**, the obtained values do not reach the efficiencies as in the previous experiments. One reason for this fact could be the change in the stirring time of the polymer which was reduced from overnight stirred to 150 minutes. There are some literature reports which showed the beneficial effect of prolonged stirring times in this type of system.^[73] Another factor, which possibly influenced the performance negatively is the air humidity which was 42% in this case, compared to 35% in the aforementioned solar cells. It was shown at our institute on several occasions that the cell performance is drastically affected by this parameter. However, by comparing the open circuit voltage of the different polymers it can be clearly seen that the polymers with lower overall palladium content achieve higher values. The maximum Voc with a value

of 0.943 V is reached with polymer **P5** with a metal loading of 400 ppm. At the same concentration **P6** gives only moderate 0.721 V. Polymer **P4** with 1200 ppm palladium is with 0.915 V in between these two extremes. Another statement concerning the open circuit voltage is, that, as expected, it is relative independent of the concentration of the active solution. This is in contrast to the current densities which show a clear improvement by using lower polymer concentrations. In this case a serious comparison should only be made between **P4** and **P5** due to the fact that this parameter is also strongly influenced by the molecular weight of the polymers which gives rise to different morphology of the film.^[82] As **P4** and **P5** have the same molecular weight with about 56.000 g/mol and **P6** is with 20.000 g/mol much shorter, it has to be discussed separately. **P6** is, independent of the concentration, always the polymer with the highest current densities with a maximum of about 2 mA/cm² at 4.5 mg/mL. By comparing **P4** and **P5** the expected trend that the palladium metal negatively influences the current density by trapping of charge carriers followed by enhanced recombination can be confirmed. Independent of the used concentration **P5** always reaches higher values. Also the highest measured current density of all cells with a value of 2.139 mA/cm² can be attributed to this polymer. By the same argument the fill factor, mainly influenced by the ratio of the mobility of the donor and the acceptor phase and the dominant morphology, should only be compared with polymers of the same chain length, leading to a separate discussion of **P6** again. Also in this case the fill factor of **P6** is compared to the other two polymers superior with values between 33 and 36%. A possible explanation could be the fact that higher molecular weights in the conductive polymer can lead to a reduced amount of molecular ordering within the polymer domains ultimately limiting the mobility.^[83] As a consequence, this reduced mobility can lead to an unbalanced charge transport in the cells, giving rise to so called space charges, which limit the fill factor to a value of at most 42%.^[84] The high molecular weight polymers **P4** and **P5** have fill factors of about 24 and 28% respectively, limiting the overall solar cell performance significantly. However, this fact may be corrected for these polymers by a suitable annealing step which increases the ordering of the polymer chains that gives rise to enhanced mobility values. To sum up the discussion of these experiments,

⁸² Schilinsky, P.; Asawapirom, U.; Scherf, U.; Biele, M.; Brabec, C.J. *Chem.Mater.* **2005**, *17*, 2175

⁸³ Kline, R.J.; McGehee, M.D.; Kadnikova, E.N.; Liu, J.; Frechet, J.M.J.; Toney, M.F. *Macromolecules* **2005**, *38*, 3312

⁸⁴ Blom, P.W.M.; Mihailtchi, V.D.; Koster, L.J.A.; Markov, D.E. *Advanced Materials*, **2007**, *19*, 1551

P6 is compared to **P4** and **P5** superior in overall solar cell performance. This is mainly caused by the higher current densities and fill factors, probably attributable to the higher mobility. The open circuit voltage, however, follows the expected trend that increasing amounts of residual palladium lead to a lowering of the electron quasi-Fermi level and, as a consequence of that, the effective band gap, given by the energy difference of the HOMO of the polymer and the LUMO of the acceptor phase, decreases. Considering only **P4** and **P5**, also the expected trend in the current density and the fill factor, concerning the palladium content, can be confirmed.

4.1.3 Correlation between residual palladium and the trap density

In the following experiments from each polymer two devices with different concentrations (6.5 and 4.5 mg/mL) were used for the determination of the open circuit voltage at different light intensities. The corresponding plots are depicted in Figure 49 together with the corresponding linear fits.

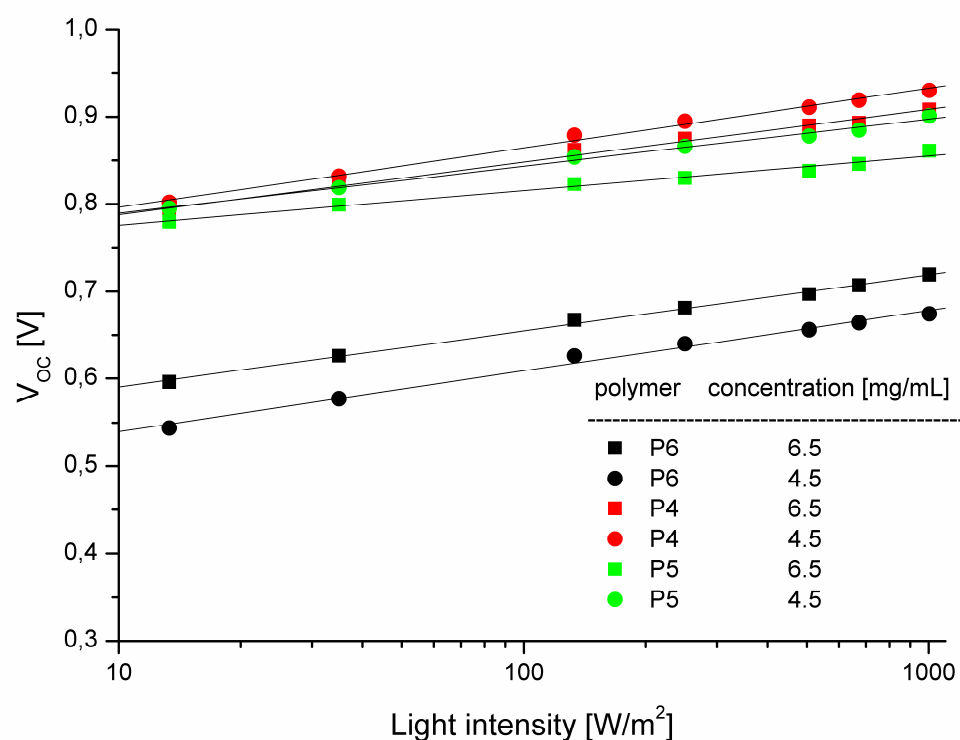


Figure 49. Plots of light intensity versus open circuit voltage of the polymers **P4** (red), **P5** (green) and **P6** (black) together with the corresponding linear fits (black lines).

The corresponding R^2 -values (quality parameter of a linear fit) are listed together with the obtained slopes in Table 11. The obtained slopes are of course no absolute values but manifolds of (kT/q) , according to equation 4.

Table 11. Obtained slopes from the measurements.

polymer	concentration [mg/mL]	Pd-content [ppm]	R^2 -value	slope
P6	6.5	5600	0.998	2.50
	4.5		0.995	2.69
P4	6.5	1200	0.996	2.35
	4.5		0.997	2.65
P5	6.5	400	0.991	1.54
	4.5		0.997	2.10

As already discussed in the introduction of this chapter, the values of the slopes are proportional to the trap densities in the devices. As can be clearly seen from the data, the slopes are related to the respective palladium content, achieving a value of 2.50 for **P6** with a concentration of 6.5 mg/mL and the highest palladium content, 2.35 for **P4** at the same concentration and finally 1.54 for **P5**. This trend also holds for the cells prepared with a concentration of 4.5 mg/mL. Another point of interest is the fact that for all cases the cells prepared at the lower concentration give higher values of the slope. A possible explanation for this effect is that by using lower concentrations of the solutions the resulting film thickness is lower. As a consequence the average light intensity per volume of the active layer is higher which could enhance the investigated effect.^[6] Another hint for the correctness of this speculation is the fact that the difference between the high and the low concentration increases with decreasing palladium content.

4.2 Experimental

4.2.1 Materials

P6, PEDOT/PSS and PCBM were purchased in the purest available form and used without further purification steps. **P4** was prepared in analogy to the polymers of chapter 3.3.5. **P5** was obtained from a purification procedure of **P4** using N,N,N'-trimethylethane-1,2-diamine immobilized on polystyrene as metal scavenger. In detail

600 mg of the polymer were dissolved in 200 mL of anhydrous toluene and then 1.2 g of the scavenger were added at a temperature of 70°C with a stirring speed of 100 rpm. The solution was stirred for 45 hours. Filtration of the resulting solution followed by a partial removal of the solvent under reduced pressure yielded 100 mL of the purified polymer solution which was precipitated in 1000 mL of MeOH. The precipitate was then filtered and dried under vacuum to give the polymer with reduced palladium content with a yield of 74%.

P4

¹H - NMR (δ , 20 °C, CDCl₃, 500 MHz): 7.65-6.79 (m, 10H), 2.02 (br, 4H), 1.07 (br, 20H), 0.80 (m, 11H)

GPC analysis: PDI = 4.99, M_n=58500 g/mol, M_w=292000 g/mol

P5

¹H - NMR (δ , 20 °C, CDCl₃, 500 MHz): 7.65-6.79 (m, 10H), 2.02 (br, 4H), 1.07 (br, 20H), 0.80 (m, 11H)

GPC analysis: PDI = 5.41, M_n=55800 g/mol, M_w=302000 g/mol

P6

GPC analysis: PDI = 2.96, M_n=20100 g/mol, M_w=59400 g/mol

4.2.2 Device preparation

The first step of the preparation was the etching of a part of the indium tin oxide (ITO) from the glass substrates. This was done to prevent shorts which may be caused by contacting the Al-electrode during the measurement of the cells. In the next step the substrates were cleaned by washing in water for 15 minutes in an ultrasonic bath at 40°C, followed by the same washing procedure in isopropanol. Some of the substrates were covered with a PEDOT/PSS layer. This was done by spin coating in two steps on a CT62 Spincoater produced by the company Karl Suss Technique. For the first step a velocity of 2500 rpm was applied for 3s, followed by a drying step with 3500 rpm for 30 s. Drying of this layer was achieved by heating to 100°C in vacuum for 25 minutes. The active layer was also deposited by spin coating with a velocity of 600 rpm for 60 seconds. Annealing was done on a hot plate under inert atmosphere in the glove box. The aluminium electrodes were evaporated through shadow masks with the coating unit MED 010 using a top down approach with tungsten coils.

4.2.3 I-V curves

The current density-voltage plots of the obtained solar cells were measured in N₂ atmosphere in the glove box using a Keithley 2400 source meter. The illumination was provided by a halogen lamp of adjustable light intensity which was set to the preferred values by adjusting with a photodiode.

5 Synthesis of CuInS₂ Nanoparticles

Reproduced in parts with permission from Pein, A.; Baghbanzadeh, M.; Rath, T.; Haas, W.; Maier, E.; Amenitsch, H.; Hofer, F.; Kappe, O.C.; Trimmel, G. *Inorg.Chem.* **2011**, 50, 193. Copyright 2011 American Chemical Society

5.1 Introduction

Copper indium disulfide, CuInS₂, like CuInSe₂, and CuIn_xGa_ySe₂ (CIGS) a member of the I-III-VI semiconductor family, is an interesting alternative for silicon based photovoltaic/solar cell materials. CuInS₂ exhibits a suitable direct bandgap of 1.5 eV, a high absorption coefficient and its applicability in solar cells has already been demonstrated.^[85,86] Today, there is a growing interest to find low cost routes for the production of solar cell materials. Solvent based routes leading to stable CuInS₂ nanoparticle dispersions are very attractive as they avoid energy intensive vacuum techniques for the production of the active material. The dispersion can be used like an “ink” and thus be applied in a broad variety of printing and coating production processes which are, in addition easily scalable towards high production speed and large areas. Different synthetic methods have been investigated for the preparation of CuInS₂ nanoparticles. Besides solid state reactions^[87], various solution based routes, e.g. hot injection methods,^[88] solvothermal routes,^[89] as well as single-source precursor methods^[90] have been applied. In particular, colloidal synthesis routes using suitable capping agents,^[91] have been heavily investigated in recent years. Recently, the popular oleylamine route originally published for binary metal sulfide nanoparticles by Joo et

⁸⁵ Nanu, M.; Schoonman, J.; Goossens, A. *Nano Lett.* **2005**, 5, 1716.

⁸⁶ Scheer, R.; Walter, T.; Schock, H. W.; Fearheiley, M. L.; Lewerenz, H. J. *Appl. Phys. Lett.* **1993**, 63, 3294.

⁸⁷ Carmalt C. J.; Morrison D. E.; Parkin I. P. *J. Mater. Chem.* **1998**, 8, 2209.

⁸⁸ Pan, D. C.; An, L. J.; Sun, Z. M.; Hou, W.; Yang, Y.; Yang, Z. Z.; Lu, Y. F. *J. Am. Chem. Soc.* **2008**, 130, 5620.

⁸⁹ (a) Jiang, Y.; Wu, Y.; Mo, X.; Yu, W. C.; Xie, Y.; Qian, Y. T. *Inorg. Chem.* **2000**, 39, 2964. (b) Yu, C.; Yu, J. C.; Wen, H.; Zhang, C. *Mater. Lett.* **2009**, 63, 1984.

⁹⁰ (a) Castro, S. L.; Bailey, S. G.; Banger, K. K.; Hepp, A. F. *Chem. Mater.* **2003**, 15, 3142. (b) Batabyal, S. K.; Tian, L.; Venkatram, N.; Ji, W.; Vittal, J. J. *J. Phys. Chem C.* **2009**, 113, 15037.

⁹¹ (a) Courtel, F.M.; Paynter, R.W.; Marsan, B.; Morin, *Chem. Mater.* **2009**, 21, 3752. (b) Czekelius, C.; Hilgendorff, M.; Spanhel, L.; Bedja, I.; Lerch, M.; Müller, G.; Bloeck, U.; Su, D.-S.; Giersig, M., *Adv. Mater.* **1999**, 11, 643. (c) Zhong, H.; Zhou, Y.; Ye, M.; He, Y.; Ye, J.; He, C.; Yang, C.; Li, Y. *Chem. Mater.* **2008**, 20, 6434.

al.^[92] has been applied for CuInS₂ nanocrystal preparation.^[93] Changing the reaction condition by using other amines, mixtures with co-ligands or using other sulfur sources strongly influences the crystal phase, growth, and morphology of the obtained CuInS₂ nanocrystals.^[94] There are also two very recent reports using microwave heating for the preparation of CuInS₂ nanoparticles, one method using a single source precursor,^[95] and another procedure utilizing an aqueous based synthesis protocol.^[96] However, to our knowledge, there is no study on microwave-assisted routes to CuInS₂ using the oleylamine route.

In the past two decades, the use of microwave energy to heat chemical reactions has attracted a considerable amount of attention, due to its many successful applications in organic/peptide synthesis, polymer chemistry, material sciences, nanotechnology and biochemical processes.^[97,98] First reports using microwave-assisted methods in nanoparticle synthesis date back to the mid 1990's^[99] and from then on all known types of nanoscale materials, ranging from metals to oxides, chalcogenides and phosphates were successfully prepared using microwave technology.^[100] The motivation for the use of microwave energy has mainly been to design faster, cleaner, and economically more viable methods of synthesis. If efficient agitation can be ensured,^[101] and the

-
- ⁹² (a) Joo, J.; Na, H. B.; Yu, T.; Yu, J. H.; Kim, Y. W.; Wu, F.; Zhang, J. Z.; Hyeon, T. *J. Am. Chem. Soc.* **2003**, *125*, 11100. (b) Kwon, G.; Hyeon, T. *Acc. Chem. Res.* **2008**, *41*, 1696.
- ⁹³ Panthani, M. G.; Akhavan, V.; Goodfellow, B.; Schmidtke, J. P.; Dunn, L.; Dodabalapur, A.; Barbara, P. F.; Korgel, B. A. *J. Am. Chem. Soc.* **2008**, *130*, 16770.
- ⁹⁴ (a) Nose, K.; Soma, Y.; Omata, T.; Otsuka-Yao-Matsuo, S. *Chem. Mater.* **2009**, *21*, 2607. (b) Koo, B.; Patel, R. N.; Korgel, B. A. *Chem. Mater.* **2009**, *21*, 1962. (c) Xie, R.; Rutherford, M.; Peng, X. *J. Am. Chem. Soc.* **2009**, *131*, 5691. (d) Norako, M. E.; Franzman, M. A.; Brutchey, R. L. *Chem. Mater.* **2009**, *21*, 4299.
- ⁹⁵ Sun, C.; Gardner, J. S.; Shurdha, E.; Margulieux, K. R.; Westover, R. D.; Lau, L.; Long, G.; Bajracharya, C.; Wang, C.; Thurber, A.; Punnoose, A.; Rodriguez, R. G.; Pak, J. J. *J. Nanomater.* **2009**, Article ID 748567, 7 pages.
- ⁹⁶ Bensebaa, F.; Durand, C.; Aouadou, A.; Scoles, L.; Du, X.; Wang, D.; Le Page, Y. *J. Nanopart. Res.* **2010**, *12*, 1897.
- ⁹⁷ For a recent review with >900 references and a tabular survey of ca. 200 microwave chemistry review articles, books and book chapters, see: Kappe, C. O.; Dallinger, D. *Mol. Diversity* **2009**, *13*, 71.
- ⁹⁸ For recent books, see: (a) Loupy, A. *Microwaves in Organic Synthesis*, 2nd ed.; Wiley-VCH: Weinheim, 2006. (b) Kappe, C. O.; Stadler, A. *Microwaves in Organic and Medicinal Chemistry*; Wiley-VCH: Weinheim, 2005. (c) Bogdal, D.; Prociak, A. *Microwave-Enhanced Polymer Chemistry and Technology*; Blackwell Publishing: Oxford, 2007. (d) Lill, J. R. *Microwave Assisted Proteomics*; RSC Publishing: Cambridge, 2009.
- ⁹⁹ (a) Komarneni, S.; Katsuki, H. *J. Am. Ceram. Soc.* **1998**, *81*, 3041. (b) Hu, M. Z.-C.; Harris, M. T.; Byers, C. H. *J. Colloid Interface Sci.* **1998**, *198*, 87. (c) Spatz, J.; Mössmer, S.; Möller, M.; Kocher, M.; Neher, D.; Wegner, G. *Adv. Mater.* **1998**, *10*, 473.
- ¹⁰⁰ (a) Bilecka, I.; Niederberger, M. *Nanoscale* **2010**, *2*, 1358. (b) Polshettiwar, V.; Nadagouda, M. N.; Varma, R. S. *Aust. J. Chem.* **2009**, *62*, 16.
- ¹⁰¹ Herrero, M. A.; Kremsner, J. M.; Kappe, C. O. *J. Org. Chem.* **2008**, *73*, 36.

temperature is monitored/controlled by fast-responding internal probes,^[101,102] rapid “in core” volumetric heating without significant temperature gradients will occur. The very rapid heating and sometimes extreme temperatures observable in microwave chemistry generally lead to faster processes and transformations which require several hours when performed in a solvent at reflux temperature in an oil bath, however may reach completion in a few minutes or even seconds using superheated solvents in a sealed vessel, autoclave-type, microwave reactor.^[103,104] These unique features explain the growing popularity of this non-classical heating method in many different fields of chemistry, including the generation of inorganic nanocrystals.^[100,105-109] Regardless of the large published body of work in this field, there is still considerable controversy on the exact reasons why microwave irradiation is able to improve the synthesis of nanoparticles.^[100] Based on the characteristics of the microwave dielectric heating phenomena^[98,18] in many of the published cases the reasons for the observed enhancements and altered nanoparticle properties comparing microwave and conventional heating are probably due to purely thermal/kinetic effects, resulting from the higher bulk reaction temperatures and more rapid heating rates that can be attained in a microwave irradiation experiment.^[105] However since the early days of utilizing microwave irradiation for nanoparticle generation,^[99] the observed rate accelerations, and the often different shape and size of the derived nanoparticles have led to speculations on the involvement of so-called “specific” microwave effects such as superheating,^[106] selective heating,^[107] or wall effect minimization.^[108] Some authors have also suggested that so-called “nonthermal” microwave effects play a role in nanoparticle generation.^[109] Unfortunately, while in organic or polymer chemistry the microwave dependent effects can be specifically discussed in terms of the reaction

¹⁰² Obermayer, D.; Kappe, C. O. *Org. Biomol. Chem.* **2010**, *8*, 114.

¹⁰³ For a more detailed description of these processes, see: (a) Gabriel, C.; Gabriel, S.; Grant, E. H.; Halstead, B. S.; Mingos, D. M. P. *Chem. Soc. Rev.* **1998**, *27*, 213. (b) Mingos, D. M. P.; Baghurst, D. R. *Chem. Soc. Rev.* **1991**, *20*, 1.

¹⁰⁴ Damm, M.; Glasnov, T. N.; Kappe, C. O. *Org. Process Res. Develop.* **2010**, *14*, 215.

¹⁰⁵ (a) Komarneni, S.; *Curr. Sci.* **2003**, *85*, 1730. (b) He, Y.; Lu, H.-T.; Sai, L.-M.; Lai, W.-Y.; Fan, Q.-L.; Wang, L.-H.; Huang, W. *J. Phys. Chem. B* **2006**, *110*, 13352. (c) R. Pana, Y. Wu, Q. Wang, Y. Hong, *Chem. Eng. J.* **2009**, *153*, 206. (d) Yu, W.; Tu, W.; Liu, H. *Langmuir* **1999**, *15*, 6. (e) Bilecka, I.; Elser, P.; Niederberger, M. *ACS Nano* **2009**, *3*, 467.

¹⁰⁶ Pol, V. G.; Langzam, Y.; Zaban, A. *Langmuir* **2007**, *23*, 11211.

¹⁰⁷ (a) Washington II, A. L.; Strouse, G. F. *Chem. Mater.* **2009**, *21*, 2770. (b) Washington II, A. L.; Strouse, G. F. *Chem. Mater.* **2009**, *21*, 3586. (c) Hu, X.; Gong, J.; Zhang, L.; Yu, J. C. *Adv. Mater.* **2008**, *20*, 4845.

¹⁰⁸ Hu, X.; Yu, J. C.; Gong, J. *J. Phys. Chem. C* **2007**, *111*, 11180.

¹⁰⁹ M. Tsuji, M. Hashimoto, Y. Nishizawa, M. Kubokawa, T. Tsuji, *Chem. Eur. J.* **2005**, *11*, 440.

trajectory,^[110] the lack of an in-depth mechanistic picture for nanoparticle formation (nucleation and growth) makes the determination of the exact influence of microwave irradiation on the intermediates and transition states for nanoparticle formation more difficult.

In this manuscript we investigate the synthesis of CuInS₂ nanoparticles using CuI, InCl₃, and elemental sulfur as precursors and oleylamine as solvent and capping agent. Thereby, we first study the onset of nanoparticles formation at low temperatures by an *in situ* X-ray study using Synchrotron irradiation. The second issue focuses on the comparison of synthesis procedures using a conventional oil bath and microwave heating at different temperatures. Finally, carefully executed control experiments are undertaken to separate putative “specific” or “nonthermal” microwave effects from thermal effects during the CuInS₂ nanoparticle synthesis.

5.2 Results and Discussion

In this study, we investigate the formation of CuInS₂ nanoparticles by a modified synthesis protocol using oleylamine as capping agent as well as solvent. In contrast to the method by Panthani et al., no additional solvent like chlorobenzene was used.^[93] For the synthesis a solution of the metal compounds (CuI, InCl₃) was prepared by heating to 170°C for 30 min in oleylamine. Separately, elemental sulfur was also dissolved in oleylamine at 130°C. After cooling down, both solutions were combined and are subjected to different heating procedures as described in detail below.

5.2.1 Study of the nanoparticle formation by WAXS

Reaction temperatures used in the oleylamine route are usually in the range of 200 °C and above, sometimes using even autoclave conditions. To determine the lowest possible temperature for the formation of the particles we investigated the reaction by a wide angle X-ray scattering (WAXS) set-up using Synchrotron irradiation to obtain a high time resolution. A part of the reaction mixture was continuously pumped through a capillary directly placed in the X-ray beam. The evolution of the most intensive

¹¹⁰ For leading reviews, see: (a) Perreux, L.; Loupy, A. *Tetrahedron* **2001**, *57*, 9199. (b) Perreux, L.; Loupy, A. in *Microwaves in Organic Synthesis*, 2nd ed. (Ed. A. Loupy), Wiley-VCH: Weinheim, 2006, chapter 4, pp 134-218. (c) De La Hoz, A.; Diaz-Ortiz, A.; Moreno, A. *Chem. Soc. Rev.* **2005**, *34*, 164. (d) De La Hoz, A.; Diaz-Ortiz, A.; Moreno, A. in *Microwaves in Organic Synthesis*, 2nd ed. (Ed. A. Loupy), Wiley-VCH: Weinheim, 2006, chapter 5, pp 219-277.

reflection of CuInS₂ at 28.1° was followed during heating the solutions from room temperature up to 170 °C using a conventional oil bath.

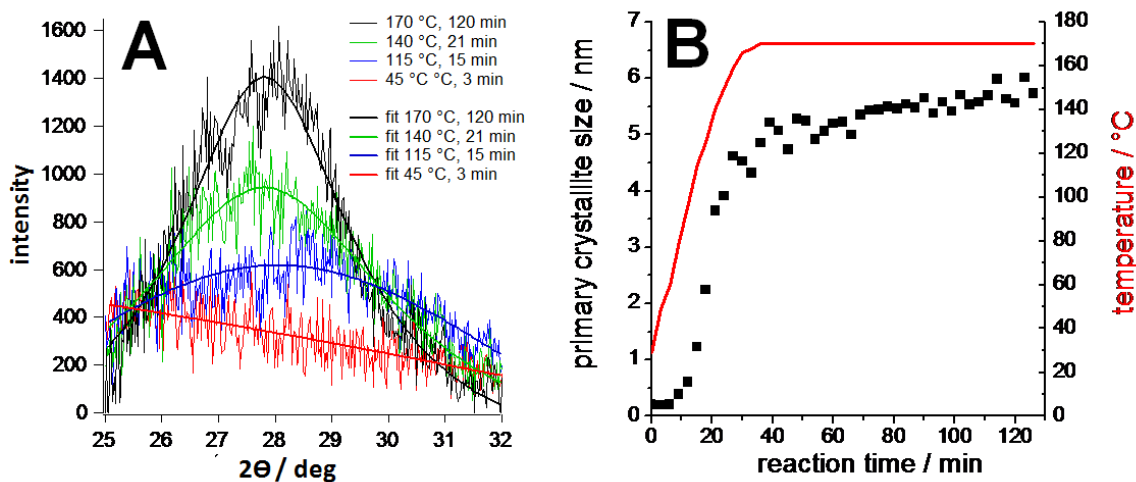


Figure 50. Wide angle X-ray scattering curves and corresponding Lorentz fits at selected temperatures (A) and primary crystallite size and temperature versus reaction time (B).

The results of the experiment are summarized in Figure 1. For better visibility selected experimental data and the corresponding Lorentz fits are depicted in Figure 1(A). The formation of the particles starts already at temperatures around 115 to 120°C, indicated by the rise of the (112) reflection at 28.1°. Using these fits, the primary crystallite sizes were estimated by the Scherrer equation and are plotted as a function of the reaction time, as presented in Figure 1(B). After 15 min - corresponding to a reaction temperature of 115°C - the primary crystallite size starts to increase very rapidly. After 36 min the growth rate flattens out which can be attributed to (1) a geometric factor, which means that with increasing size more monomer has to reach the particle surface to induce the same increase in particle size and (2) the decrease in educt concentration. The WAXS analysis shows that a temperature of only 120°C should be sufficient for the formation of CuInS₂ nanoparticles, which is 120°C below the value of a literature protocol using oleylamine reported by the group of Korgel.^[111]

¹¹¹ Koo, P.; Patel, R. N.; Korgel, B. A.; *Chem. Mater.* **2009**, *21*, 1962.

5.2.2 CuInS₂ nanoparticle synthesis at 120°C

In order to analyze the generation of CuInS₂ nanoparticles in a preparative way, the combined reaction mixture was heated up from room temperature to the comparatively low reaction temperature of 120 °C. Samples of the reaction solution were taken after 15 and 60 min, but also after an extended reaction time of 20 h. The time includes the heating ramp of ~15 min, thus the 15 min sample is taken immediately after the reaction mixture has reached the target temperature of 120 °C. The nanoparticles were separated from the reaction mixture by precipitation in cold methanol and subsequent centrifugation.

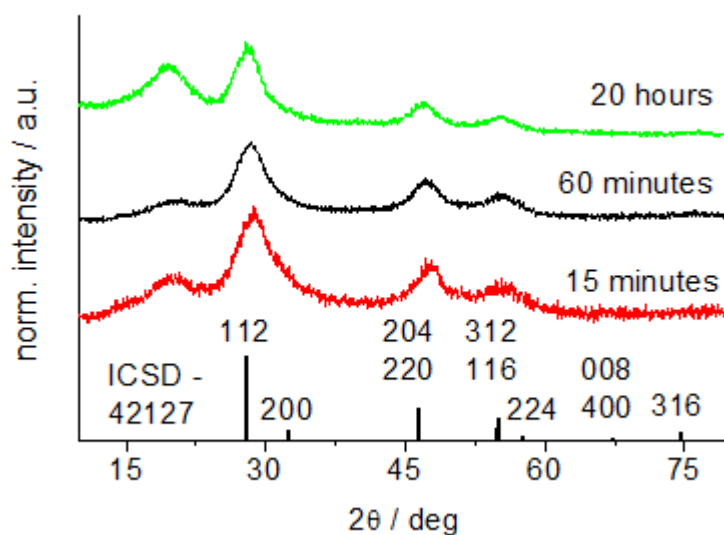


Figure 51. XRD-patterns of particles prepared at 120°C after different heating times (curves are shifted vertically for better visibility). The peaks are in good agreement with the reference file for chalcopyrite type CuInS₂ (ICSD – 42127– sharp lines at the bottom).

The corresponding XRD-patterns of these samples are compared with the reference data for CuInS₂ (ICSD – 42127) in Figure 51. The most prominent chalcopyrite reflections of CuInS₂ (Miller indexes are shown together with the reference data) are present, although the signals are noisy and broad, indicating the reduced crystallite size. Using the Scherrer equation, a primary crystallite size of 2.3 nm was calculated for nanoparticles obtained after a reaction time of 15 min. After 60 min, the particles reach a size of 2.6 nm and finally 3.7 nm after 20 h. However, the Scherrer equation can only give a rough estimation, especially for particles in the low nm range, but it gives an overall trend for particle size evolution. The peak around $2\theta = 18^\circ$ can be attributed to

the capping molecule, oleylamine (see supporting information). Interestingly, this peak is less pronounced for the first two samples (15 min, 60 min). Exactly these two samples are not soluble in nonpolar solvents, whereas the third sample and all samples prepared at 220 °C are rapidly soluble in solvents like hexane, chloroform, and dichloromethane. At the moment we have no explanation for this phenomenon, but the lower intensity of the XRD-peak at $2\theta = 18^\circ$ is an indication that less copper is retained after the work up and therefore a higher tendency of these particles to agglomerate is expected.

In Figure 52(A), the TEM image of the sample prepared at 120 °C for 20 h shows nanoparticles with a diameter between 2 and 4 nm. In addition, some larger agglomerates between 5 and 10 nm are visible.

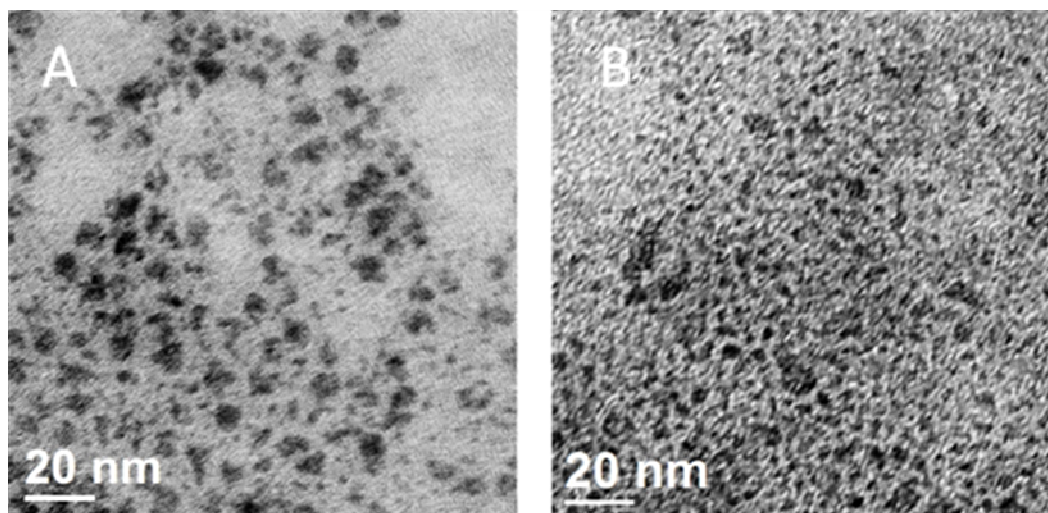


Figure 52. TEM image of CuInS₂ nanoparticles (A) prepared at 120 °C using conventional heating for 20 h and (B) microwave irradiation for 60 min.

To investigate possible differences between the classical oil bath synthesis and an alternative heating mechanism by microwave irradiation, the nanoparticle synthesis was also performed in a dedicated microwave reactor at 120 °C. It should be emphasized, however, that in these preliminary experiments the heating profiles seen in the oilbath experiments were mimicked in the microwave runs by simply adjusting the instrument power, and not by an adequate algorithm that involves feedback from an internal temperature probe (see below). In addition, other important processing factors such as reaction volume, vessel geometry and stirring speed were all different (see Experimental Section for details). Importantly, the temperature measurements for both sets of experiments were different, since for the oilbath runs a traditional glass

thermometer monitoring the reaction mixture temperature was used, while in the microwave experiments an external IR sensor reading the surface temperature of the Pyrex reaction vessels was employed. Reaction times refer to overall reaction time involving ramp time (time needed to reach the target temperature) and hold time (time for which the sample is held at target temperature). The corresponding heating profiles are depicted in Figure 53. Reaction times of 15 and 60 min were applied.

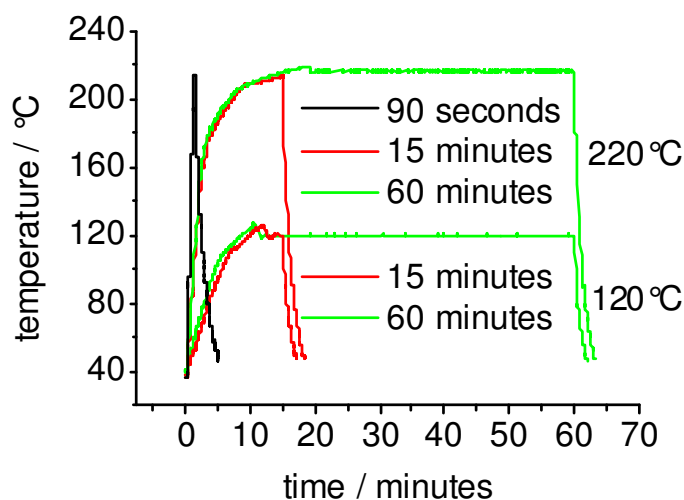


Figure 53. Heating profile of the microwave experiments at 120 °C and at 220 °C.

Figure 54 shows the XRD patterns of the samples synthesized under microwave conditions at 120°C. In both cases CuInS₂ nanoparticles of chalcopyrite structure are obtained. According to the Scherrer equation, the particles have an average primary crystallite size of 1.8 nm after 15 min and 2.5 nm after 60 min, thus the particle sizes are comparable with those obtained using the oil bath (2.3 nm, 15 min; 2.6 nm, 60 min). In addition, these particles contain a significant amount of organic copper (peak around $2\theta = 18^\circ$) and both the samples are soluble in organic nonpolar solvents. The peak around $2\theta = 15^\circ$ in the 60 min sample can be attributed to a small quantity of unidentified impurities.

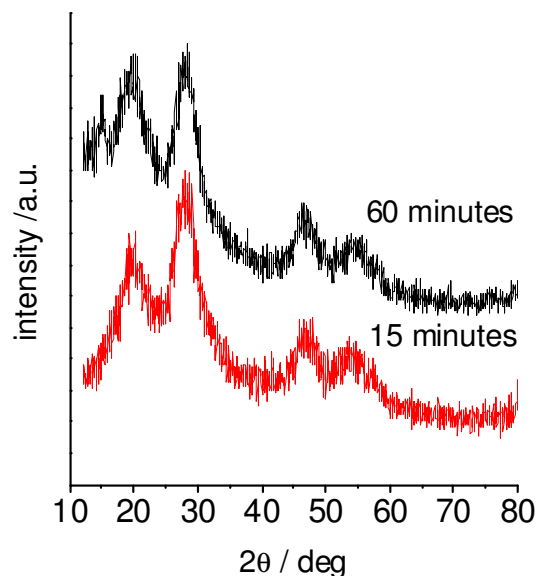


Figure 54. XRD patterns of CuInS₂ nanoparticles prepared using microwave heating at 120°C times (curves are shifted vertically for better visibility).

Figure 52(B) shows the TEM image of the particles prepared using microwave heating after a reaction time of 60 min. The particle size is around 3 nm but also in this case the size distribution is quite broad.

The TEM images as well as the XRD data clearly show that CuInS₂ nanoparticles are already formed at 120 °C using both heating methods, at much lower temperatures as usually employed for this synthesis protocol. However, the particles are rather small in size, the size distribution is broad, and the particles are irregular in shape. In order to improve the particle quality, in the next step we investigated both synthesis methods at 220 °C, a temperature which can be obtained with conventional oil bath as well as by microwave heating.

5.2.3 CuInS₂ nanoparticle synthesis at 220°C

Figure 55 shows the XRD – patterns of nanoparticles prepared with oil bath heating after 15, 40 and 80 min at a temperature of 220 °C. An increase of particle size can be observed from the increase of reflections with longer reaction times. In addition, some minor intensity reflections ($2\theta = 57.7^\circ$ and 77.1°) are now clearly visible. The primary crystallite sizes, estimated from the Scherrer-equation, reach a size of 5.7 nm after 15 min, after 40 min 9.4 nm and finally after 80 min the size is around 12.1 nm.

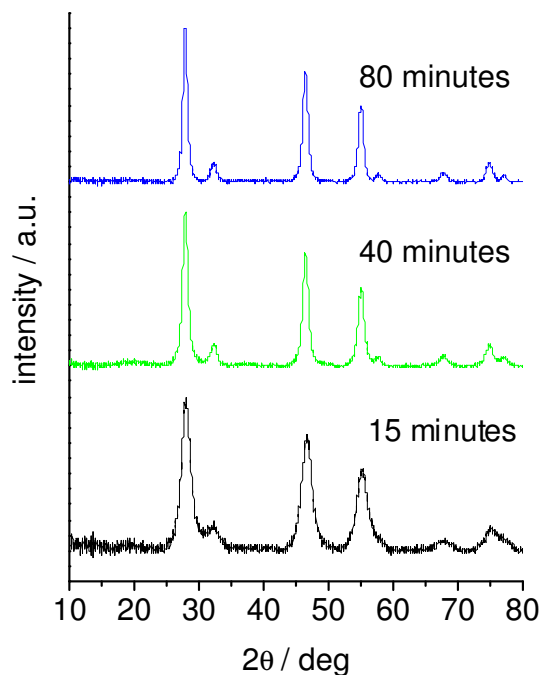


Figure 55 XRD-patterns of particles prepared at 220°C after different heating times (curves are shifted vertically for better visibility).

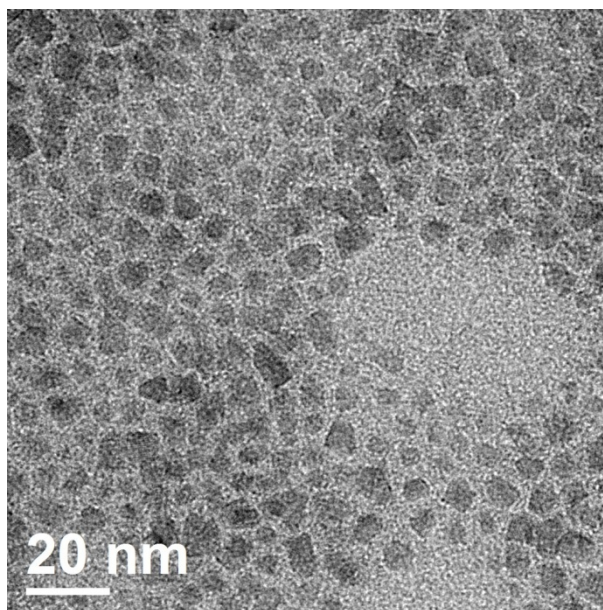


Figure 56. TEM image of CuInS₂ particles prepared at 220°C using oil bath for 15 min.

The TEM image in Figure 56 shows a representative overview of the nanoparticles obtained at 220 °C using conventional heating. The particles are of angled shape and the particle size is in the range between 5 and 10 nm. Compared to the particles prepared at 120°C (Figure 52) the size distribution is improved and also the shape is much more regular.

The same experiment at 220 °C target temperature was additionally undertaken using microwave irradiation. The heating profiles for these experiments are presented in Figure 53. In both cases reaction times of 15 and 60 min were applied using a heating profile similar to conventional heating. In addition, an experiment with very short reaction time of 90 s including 80 s ramping and 10 s heating at target temperature (high microwave power) was performed, as especially the fast heating ramp is considered to be an important asset of microwave chemistry.^[96,97,99] Figure 57 compares the XRD patterns of the particles from these experiments. The crystal modification of chalcopyrite type CuInS₂ is also obtained in all cases. The experiment (15 min heating) with a slower heating ramp (cf. Figure 4) – approximately the same heating rate was used in the oil-bath experiments - yields particles with a particle size of 3.5 nm. Using prolonged microwave irradiation for an additional 45 min leads to particles with a size of 6.5 nm. Interestingly, particles with a size of 3.3 nm are already obtained after 90 s heating at 220 °C. This demonstrates one of the distinct advantages of microwave chemistry, fast syntheses protocols by extremely fast heating to the desired temperatures.^[97,98,100]

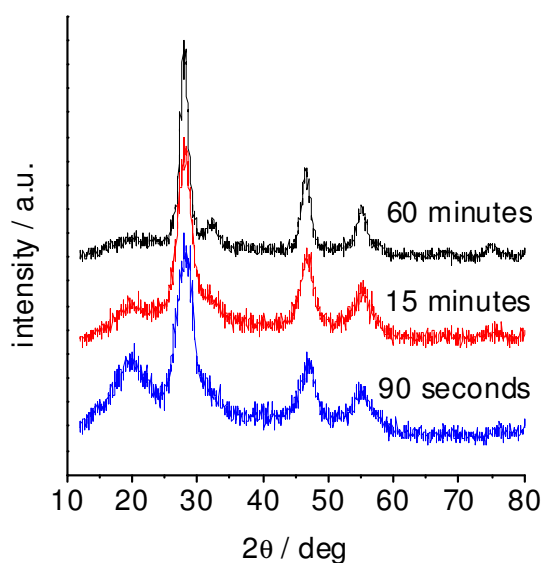


Figure 57. XRD patterns of the particles prepared using microwave heating at 220°C (curves are shifted vertically for better visibility).

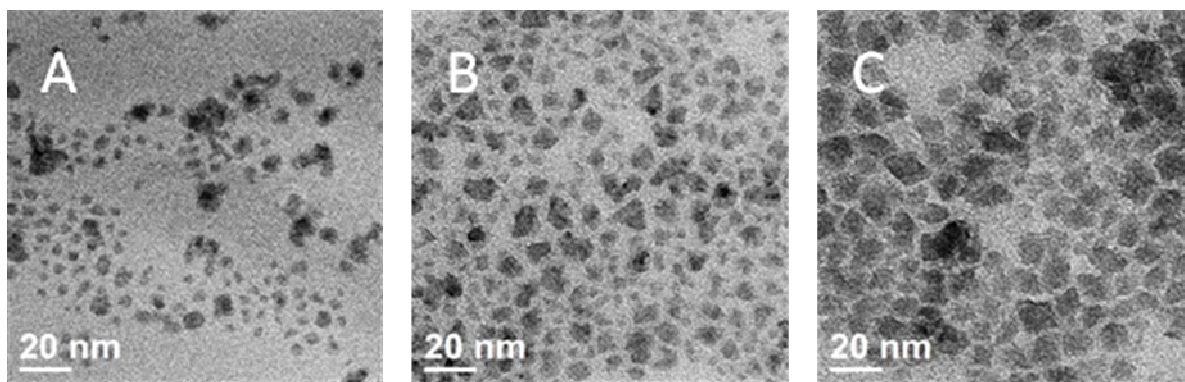


Figure 58. TEM images of the CuInS₂ nanoparticle samples prepared at 220°C using microwave irradiation: (A) 90 s, (B) 15 min, and (C) 60 min experiment.

In Figure 58, the TEM images of these samples differ significantly from each other. In contrast to the XRD-patterns, the shape and size distribution of the nanoparticles of the 90 s sample and the 15 min sample seems to be different. However, having a closer look both samples contain nanoparticles with a crystallite size of approximately 2-4 nm, but the 15 min samples show, in addition, a lot more agglomerates in the range of 6 to 15 nm. The particles obtained by the 60 min synthesis are very irregular and exhibit a broad size distribution with particles ranging in size from 5 to 20 nm. Comparing the TEM images in Figure 58B, the nanoparticles obtained with microwave irradiation at 15 min, and in Figure 56, the sample prepared using conventional heating, the particle size (2–3 nm compared to 5-6 nm) as well as the size distribution are quite different depending on the used heating. Therefore, an analysis of the above results may in fact imply the existence of a “microwave effect” in the preparation of these materials. However, as it is known that the geometry of the reaction vessel, the heating and cooling ramp, and stirring speed sometimes have a significant influence in microwave chemistry,^[100,102] a series of carefully executed control experiments was designed to minimize these effects.

5.2.4 Comparison of oilbath and microwave heating for the CuInS₂ nanoparticle generation under controlled reaction conditions

In order to accurately compare the results obtained by direct microwave heating with the outcome of a conventionally heated chemical transformation, we have recently demonstrated that the utilization of reaction vials made out of sintered silicon carbide

(SiC) ceramic in microwave reactors can mimic a conventionally heated autoclave experiment, while retaining the rapid heating (flash heating) and excellent process control features inherent to microwave chemistry.^[115] Since by employing a SiC vial any effects of the electromagnetic field on the reaction mixture can be eliminated, this technology makes it possible to effectively separate thermal from specific/nonthermal effects.^[115] As an additional control experiment, the CuInS₂ nanoparticle synthesis was also performed in a conventionally heated Pyrex vial with internal temperature control that allowed us to accurately mimic the heating profiles obtained in the microwave experiments.^[101] Internal temperature control using fiber-optic technology was used for both microwave and conventionally heated runs since recent evidence has demonstrated that monitoring reaction temperatures by conventional infrared sensors on the outside vessel wall is not an acceptable technique if an accurate temperature profile for comparison studies needs to be obtained.^[101,102,112] Since oleylamine is a solvent of comparatively low microwave absorptivity,^[103] the pure solvent alone cannot be heated to high temperatures (>200 °C) under microwave conditions. In contrast, the reaction mixture can be easily heated to 220 °C within 2 min, indicating that the precursor-solvent complex will absorb most of the microwave energy (“selective heating”). Control experiments between microwave and conventional heating (SiC vials) were performed on a 3 mL scale using Pyrex and SiC vials in a microwave reactor under otherwise completely identical reaction conditions. The heating profiles were carefully adjusted by variation of microwave power to minimize differences resulting from a thermal effect as shown in Figure 10A. In addition, a control experiment using a pre-heated oil bath (bath temperature 220 °C) was performed, leading to a similar heating profile. In all cases the desired final temperature was 220°C and the overall heating period (including ramp and hold time) was 15 minutes. In Figure 10B, the corresponding XRD patterns are shown. The same reflections can be seen in all three samples and also the primary crystallite size of around 5.4 nm is in all cases identical. In order to exclude any experimental artefacts, these series of microwave and oilbath experiments were performed twice, leading to identical results.

¹¹² (a) Kremsner, J. M.; Kappe, C. O. *J. Org. Chem.* **2006**, *71*, 4651. (b) Hosseini, M.; Stiasni, N.; Barbieri, V.; Kappe, C. O. *J. Org. Chem.* **2007**, *72*, 1417. (c) Nüchter, M.; Ondruschka, B.; Bonrath, W.; Gum, A. *Green Chem.* **2004**, *6*, 128. (d) Leadbeater, N. E.; Pillsbury, S. J.; Shanahan, E.; Williams, V. A. *Tetrahedron* **2005**, *61*, 3565.

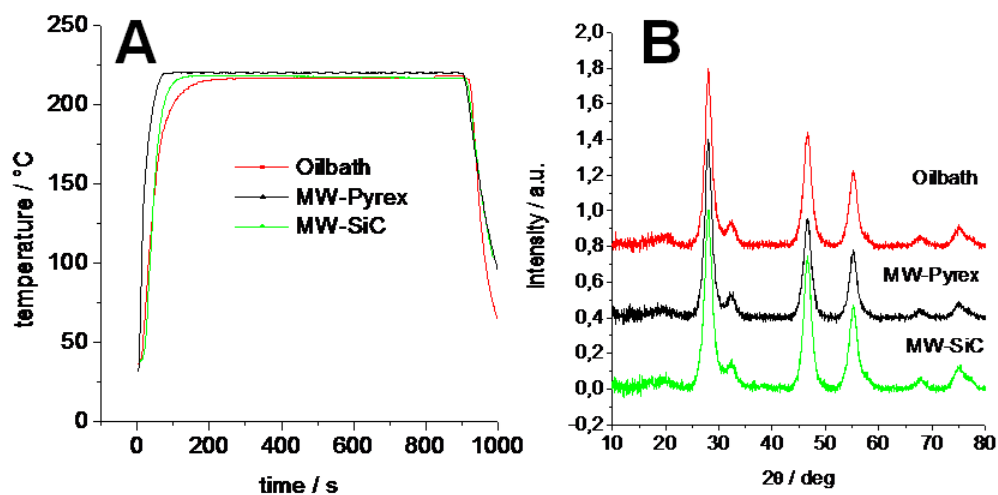


Figure 59. Heating profiles of the control experiments (A), XRD-patterns of the experiments obtained after 900 s (15 min) overall reaction time (B).

From the TEM images, depicted in Figure 60 similar nanoparticle shapes and size distributions in the range between 5 and 10 nm can be seen for samples obtained from the three types of experiments. The only differences stem from different particle concentration in the images. Also the SAED inserts confirm the XRD-results showing the diffraction rings of non-oriented nanocrystalline CuInS₂.

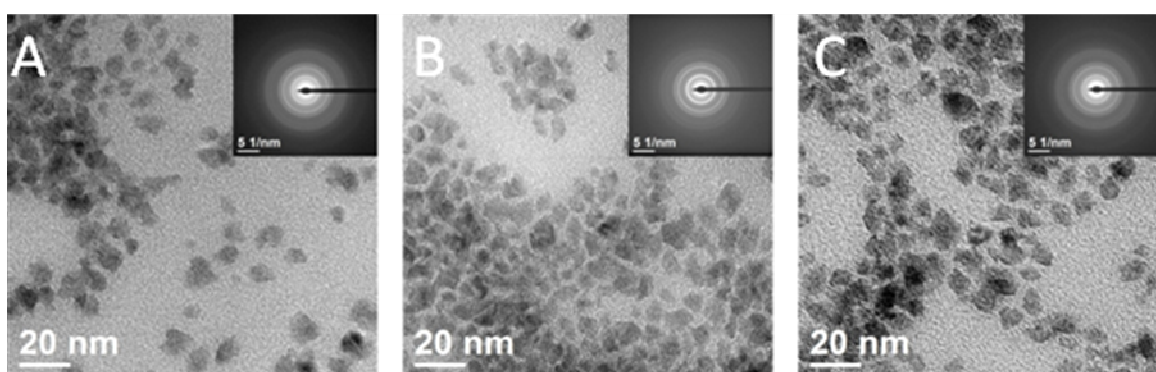


Figure 60. Comparison of TEM images and SAED pattern (insert) of the CuInS₂ nanoparticles synthesized at 220 °C of the (A) MW-Pyrex, (B) MW-SiC, (C) Oilbath experiments.

Thus, both TEM and XRD-experiments cannot identify significant differences between the two heating modes. This fact was confirmed by optical absorption measurements, shown in Figure 61. Weak absorption of the nanoparticles already starts at a wavelength of around 850 nm. However, a significant increase in absorption can be observed around 500 nm, which is similar to several literature reports.^[113,114]

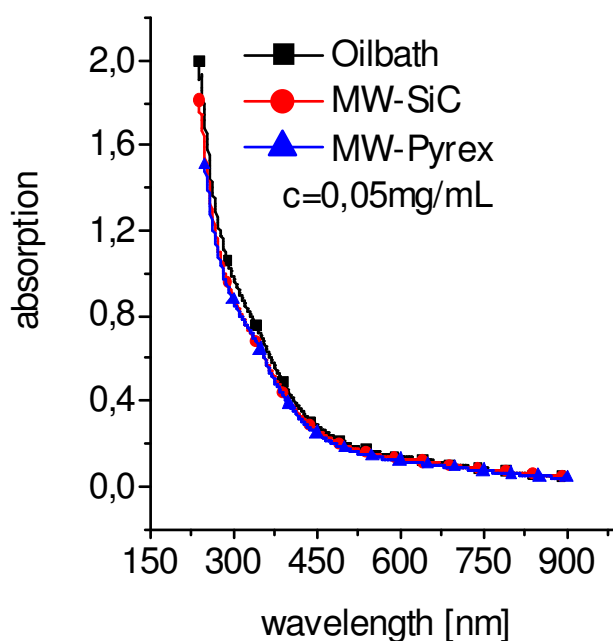


Figure 61. UV-Vis spectra of the CuInS₂ samples synthesized at 220 °C.

The only small difference which was observed is the fact that the microwave sample has a somewhat higher amount of capping ligand, detected by thermogravimetric analysis shown in Figure 62. A mass loss due to the evaporation of the capping oleylamine of 30.7% in the case of the SiC sample, an almost identical value of 30.3% in the case of the oilbath sample and a slightly higher value of 34.7% for the Pyrex – sample was detected. The increased content of capping agent is also visible in the emission spectra of the samples, depicted in Figure 63.

¹¹³ Castro, S. L.; Bailey, S. G.; Raffaele, R. P.; Banger, K. K.; Hepp, A. F. *J.Phys.Chem.B* **2004**, *108*, 12429.

¹¹⁴ Chen, Y.; He, X.; Zhao, X.; Song, M.; Gu, X. *Mater. Sci. Eng. B* **2007**, *139*, 88.

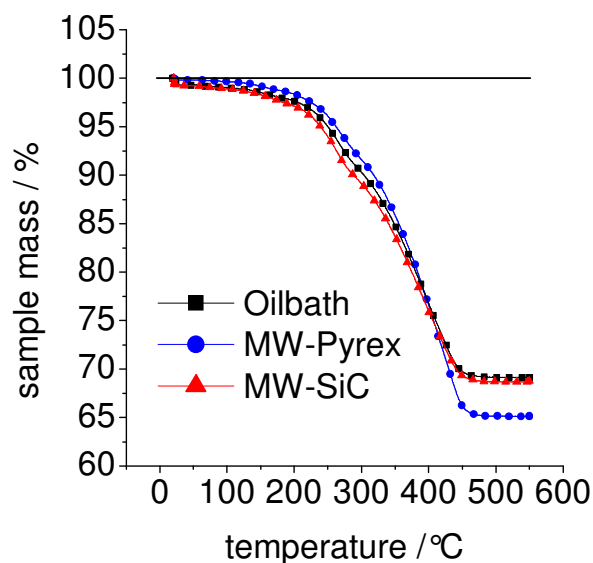


Figure 62. TGA experiments of the CuInS₂ samples synthesized at 220 °C.

An excitation wavelength of 355 nm was used for the oilbath sample, leading to an emission with a maximum at 425 nm. For the SiC and the Pyrex samples an excitation wavelength of 357 nm was applied, giving maxima in the emission intensity at 428 nm for SiC and 430 nm for the Pyrex sample. Currently, we have no explanation for this reproducible effect, but further experiments are planned.

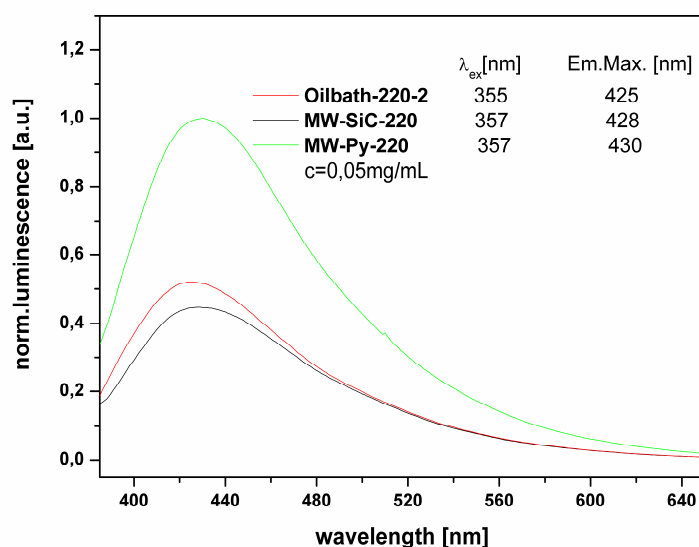


Figure 63. emission spectra of the samples in chloroform solution; c = 0.05 mg/mL.

5.2.5 Experimental Section

All chemicals were purchased from Sigma Aldrich in the following purities: InCl₃ (98%), CuI (99,999%), elemental sulfur (reagent grade) oleylamine (technical grade). All chemicals were used without further purification.

Caution: In the below described reaction, toxic and low volatile thiols can be evolved. All reactions must be undertaken under a fume hood and protection clothing must be used.

5.2.5.1 Microwave Instrumentation

Preliminary microwave synthesis experiments were carried out using a Biotage Initiator 8 EXP (2.5) single-mode cavity instrument producing controlled microwave irradiation at 2450 MHz (Biotage AB, Uppsala). Experiments were performed in sealed Pyrex microwave vials (0-400 W maximum power) using temperature control mode. Reaction times refer to hold times at the reaction temperature indicated, not to total irradiation times. The temperature was measured with an IR sensor on the outside of the reaction vessel. Advanced microwave experiments with internal reaction temperature monitoring were performed using a Monowave 300 single-mode microwave reactor from Anton Paar GmbH (Graz, Austria). The instrument uses a maximum of 850 W magnetron output power and can be operated at 300 °C reaction temperature and 30 bar pressure. The reaction temperature is monitored either by an external infrared sensor (IR) housed in the side-walls of the microwave cavity measuring the surface temperature of the reaction vessel, and/or by an internal fiber-optic (FO) temperature probe (ruby thermometer) protected by a borosilicate immersion well inserted directly into the reaction mixture.^[115] Microwave experiments were carried out either in 10 mL Pyrex vessels or in 10 mL silicon carbide (SiC) reaction vials with magnetic stirring. The use of SiC vials shields the contents of the vessel from the electromagnetic field and therefore simulates an oil bath experiment.^[115]

5.2.5.2 Synthesis of CuInS₂ Nanoparticles

Conventional synthesis: CuI (1.527 g, 8.00 mmol) and InCl₃ (1.772 g, 8.00 mmol, 1.0 equiv) were dissolved in oleylamine (80 mL) by heating the mixture to 170 °C for 30

¹¹⁵ Obermayer, D.; Gutmann, B.; Kappe, C. O. *Angew. Chem. Int. Ed.* **2009**, *48*, 8321.

min. After the solution was cooled down, a solution of sulfur (1.539 g, 48.00 mmol, 6 equiv) in oleylamine (20 mL), prepared by heating to 130°C, was added and the resulting mixture was heated to the desired target temperature for the appropriate time period (see main text) using an oil bath. The resulting solution was cooled to ambient conditions and the particles were precipitated by addition of methanol and separated by centrifugation. The particles were washed by suspending them in methanol, separated by centrifugation and dried under reduced pressure at ambient temperature.

Microwave synthesis: The precursor solutions were prepared following the same procedure as described above. Subsequently, a 20 mL Pyrex vessel equipped with a stir bar was charged with 8 mL of metal salts solution and 2 mL of sulfur solution. The vessel was sealed with a septum and the reaction mixture was exposed to microwave irradiation and held at a desired temperature for the appropriate time period (see main text). The work up procedure was performed as described above.

Comparison studies: Comparison experiments between microwave and conventional heating were carried out mixing 2.4 mL of metal salt solution with 0.6 mL of sulfur solution in either a Pyrex or SiC 10 mL reaction vessels equipped with a stir bar. The vessels were sealed with a septum and the reaction mixtures were either exposed to microwave irradiation (MW-Pyrex and MW-SiC) or immersed in a preheated oil bath at 220 °C for 15 min (Pyrex, Oilbath). After being cooled to room temperature the same work up and purification procedure as mentioned above for conventional synthesis afforded the nanoparticles.

5.2.5.3 Characterization techniques

Powder-X-ray diffraction (XRD) measurements were performed on a Siemens D-5005 powder-diffractometer (theta-theta geometry, Cu-K_α-radiation). The sample was placed on a silicon substrate and applied to a scan rate of 0.036 ° s⁻¹ to record the patterns in the 2θ range between 10 and 80°. The diameters of the crystallites were estimated according to the broadening of the diffraction peaks using the Scherrer relationship (equation 1):

$$D_{XRD} \approx \frac{K * \lambda}{\Delta(2\theta) * \cos \theta} \quad (5)$$

with $\Delta(2\theta)$ is the full width at half maximum (FWHM) of the peak in radians, θ is half of the scattering angle 2θ , λ the wavelength of the X-rays, and K is the shape factor (K = 0.9 for spherical particles). In this context it is very important to note that the Scherrer

relationship is only a good approximation for spherical crystals. The size is inversely proportional to the FWHM. For the calculation, the (112)-reflection at $2\theta = 28.4^\circ$ was used. The experimental line width was determined to be 0.12° at this 2θ - position by measuring a Si-reference standard (NIST 640c).

Transmission Electron Microscopy (TEM)-images were acquired on a Tecnai F 20 microscope (FEI Company) with a Schottky emitter, an UltraScanCCD camera and a Gatan GIF Quantum energy filter system. Selected area electron diffraction measurements were evaluated by determination of the diffraction center and measurement of the ring radii using the method and software plug-in described by Mitchell.^[116] TEM-samples for imaging were prepared from a dispersion of 0.04 mg/mL particles in chloroform by putting a drop of the dispersion on a Nickel-TEM-grid with a carbon film and evaporation of the solvent. UV/Vis spectra of nanoparticle solutions in chloroform (0.05 mg/mL) were measured with a Shimadzu UV-1800 spectrophotometer.

Thermogravimetric analysis (TGA) measurements were performed with a simultaneous thermal analyzer STA 449 C Jupiter from Netsch-Gerätebau GmbH (crucibles: aluminum) with a heating rate of $10^\circ\text{C}/\text{min}$ in a flow of He (50mL/min).

The growth of the CuInS₂ nanocrystals was studied by in situ time-resolved WAXS-measurements recorded at the Austrian SAXS beamline 5.2 L^[117] of the Italian synchrotron center, ELETTRA, Trieste, operated at 2 GeV. For the detection of the WAXS signals in the 2θ range of 25 to 32° a 1D gas detector was used. Fitting of the WAXS-peaks was done with Lorentz function. The primary particle size was estimated with the Scherrer equation.

The experimental set-up consisted of a reaction vessel, a peristaltic pump, tubes and a flow-through cell situated in the centre of the beam.^[118] The reaction was conducted in the reaction vessel equipped with a reflux condenser and a thermometer. The reaction mixture was stirred and heated by a magnetic stirrer/heater. To pump the solution

¹¹⁶ Mitchell, D.R.G. *Ultramicroscopy* **2008**, *108*, 367-374.

¹¹⁷ Amenitsch, H.; Bernstorff, S.; Kriechbaum, M.; Lombardo, D.; Mio, H.; Rappolt, M.; Laggner, P. *J. Appl. Crystallogr.* **1997**, *30*, 872.

¹¹⁸ Argen, P.; Linden, M.; Rosenholm, J. B.; Schwarzenbacher, R.; Kriechbaum, M.; Amenitsch, H.; Laggner, P.; Blanchard, J.; Schüth, F. *J. Phys. Chem. B* **1999**, *103*, 5943.

through the measuring cell, we used steel capillaries as tubes; only for a small distance directly at the peristaltic pump an elastic neoprene tube was used. The steel capillaries were isolated to reduce the temperature loss of the solution during pumping to the measuring cell. The measuring cell was heated to 80 °C and the flow rate was adjusted to 5 mL/min. The concentration of the nanoparticles in solution was 4.5 w/w%.

6 Energy Transfer

6.1 Introduction

In this chapter the interaction of ZnO nanoparticles with an amphiphilic block copolymer bearing platinum excimers was investigated. The acid functionalities located on the polymer here act as the functionality which enables simultaneous coordination of the dyes and particles. The following investigations mainly deal with an energy transfer taking place due to an overlap of nanoparticle emission and absorption of the dyes. A model describing the overall process was worked out and confirmed through different experiments. The second part deals with possible applications of this material combination for the detection of Cu²⁺ ions.

In recent years block copolymers have become a highly investigated topic within the scientific community due to possible applications in the field of drug delivery systems^[119], electronics^[120], or as surfactants for nanomaterials.^[121,122] Especially amphiphilic block copolymers, consisting of covalently linked hydrophilic and hydrophobic blocks, offer interesting properties concerning the design of nanostructures. This can be attributed to the fact that phase separation between the two (or even more) immiscible blocks can only occur on the nanoscale level.^[122] In this study ring opening metathesis polymerization was used as polymerization technique to prepare a defined block copolymer.^[123] As hydrophobic monomer *endo, exo*[2.2.1]bicyclo-hept-5-ene-2,3-dicarboxylic acid dimethylester was chosen and as hydrophilic building block *endo, exo*[2.2.1]bicyclo-hept-5-ene-2,3-dicarboxylic acid was used. During the synthesis the acid functionalities had to be protected with tert-butyl groups in order to ensure an efficient conversion by using the Grubbs catalyst of the third generation.

¹¹⁹ N. Nishiyama, K. Kataoka, *Adv. Polym. Sci.* **2006**, 193, 67

¹²⁰ A.C. Edrington, A.M. Urbas, P. DeRege, S. Chen, T.M. Swager, *Adv. Mater.* **2001**, 13, 421.

¹²¹ Cölfen, H. *Macromol. Rapid Commun.* **2001**, 22, 219

¹²² Niedermair, F. Thesis, Graz University of Technology, **2009**

¹²³ Riegler et al. *Macromol. Symp.* **2004**, 217, 231

Charged platinum complexes belong to another promising class of materials due to their interesting optical properties. Their absorption and emission spectra differ significantly in the solid state and in solution. This can be explained by the special packing behavior in the solid resulting in polynuclear species that exhibit red shifted emission compared to the mononuclear species.^[124] This “low-energy” emission can be observed even in concentrated solutions resulting from excimer formation. Excimers are excited dimers which are formed in solution through a diffusion-controlled process that results from the interaction of one molecule in the ground state with another identical molecule in its excited state.^[125] The positive charge can be used as some kind of electrostatic attractor for anionic, or more general, coordinating species. By using a block copolymer bearing functionalities suitable to coordinate to the platinum complex, accumulation of the dyes in the acidic groups on the polymer is expected, resulting in the formation of excimers. Indeed, an intense luminescence signal centered at 646 nm upon the addition of the polymer to the platinum complex was observed, whereas prior to the addition only very weak luminescence at 510-542 nm was detectable.

Semiconducting nanoparticles are interesting due to their size dependent optical and optoelectronic properties. This special behavior of nanoscaled materials in general can be explained by quantum mechanics.^[126] ZnO nanoparticles gained a lot of interest within the scientific community since the late 1980s^[127] due to promising properties interesting for various fields of research, including optoelectronic^[128], catalytic^[129] and imaging^[130] applications. ZnO nanoparticles have a sharp absorption edge in the UV – region centered at 325 nm. Especially their emission properties, consisting of two emission peaks, one originating from band edge emission at 372 nm and the other from trap states on the surface at 512 nm, offer promising material combinations with platinum excimers. Based on the high surface to volume ratio, nanoparticles in general need a stabilizing sphere which prevents or at least suppresses agglomeration.

¹²⁴ Lu, W.; Chan, C.W.; Zhu, N.; Che, C.-M.; Li, C.; Hui, Z. *J. Am. Chem. Soc.* **2004**, 126, 7639

¹²⁵ Williams, J.A.G.; Develay, S.; Rochester, D. L.; Murphy, L. *Coord. Chem. Rev.* **2008**, 252, 2596–2611

¹²⁶ Weller, H. *Angew. Chem. Int. Ed. Engl.* **1993**, 32, 41

¹²⁷ Koch, U.; Fojtic, A.; Weller, H.; Henglein, A. *Chem Phys Lett* **1985**, 122, 507

¹²⁸ Krebs, F.C.; Thomann, Y.; Thomann, R.; Andreasen, J.W. *Nanotechnology* **2008**, 19, 424013

¹²⁹ Schimpf, S.; Lucas, M.; Mohr, C.; Rodemerck, U.; Brückner, A.; Radnik, J.; Hofmeister, H.; Claus, P. *Catalysis Today* **2002**, 72, 63

¹³⁰ Xiong, H.M.; Xu, Y.; Ren, Q.G.; Xia, Y.-Y. *J. Am. Chem. Soc.* **2008**, 130, 7522

Stabilizers used during the synthesis not only allow defined particle size distributions and shapes but also have a great influence concerning the electronic and optical properties. Moreover, the ability of the nanoparticle surface to coordinate to various molecules with polar headgroups gives rise to additional interesting material combinations.

6.2 Results and Discussion

6.2.1 Synthesis of the platinum dye

The charged platinum complex **2** was synthesized at our institute and is described in detail elsewhere.^[122] The mononuclear platinum(II) precursor **1** was first reacted with silver trifluoroacetate to detach the chloride ion and subsequently converted with 1,10-phenanthroline to the corresponding cationic platinum complex. Generally, solubility of cationic platinum complexes is very low.^[122] The introduction of the hexyloxy group in the cyclometalating ligand was accomplished to improve the solubility of the charged complex.

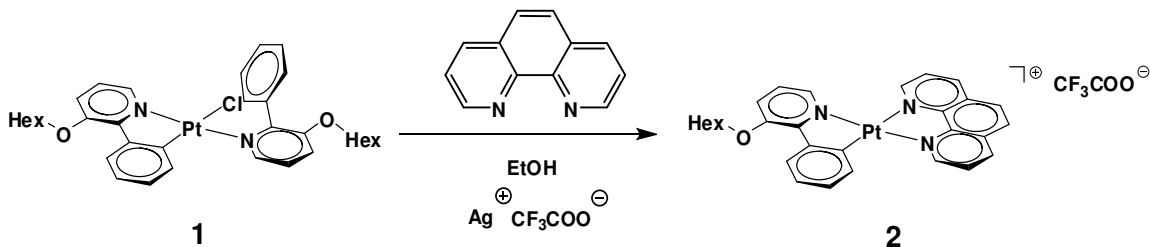


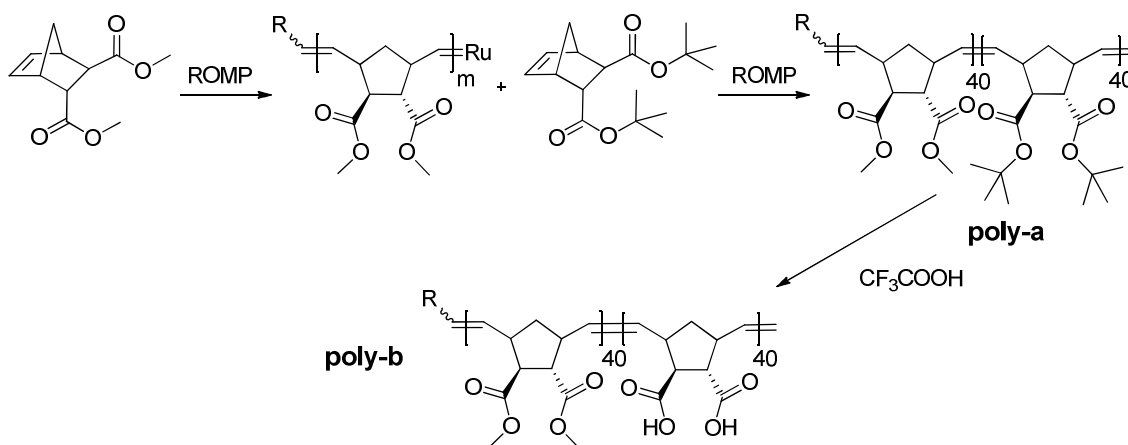
Figure 64. Synthesis of the charged platinum complex (**2**).

6.2.2 Synthesis of the Polyelectrolyte

The synthesis of the amphiphilic block copolymer is described in detail elsewhere.^[131] In short, the polymer was synthesized by ring opening metathesis polymerization using the Grubbs catalyst of the third generation. First of all, as hydrophobic part of the polymer *endo, exo*[2.2.1]bicyclo-hept-5-ene-2,3- dicarboxylic acid dimethylester was converted, and after complete consumption, in a second step, the hydrophilic building

¹³¹ Stubenrauch, K. Ph.D. *Theses*, Graz University of Technology 2007

block of the polymer, *endo*, *exo*[2.2.1]bicyclo-hept-5-ene-2,3-dicarboxylic acid was incorporated. Finally, the tert-butyl protecting groups, which ensure a controlled polymerization, were cleaved using trifluoro-acetic acid, yielding polymer poly-b. For the following measurements building blocks of 40 monomer units were used.



Scheme 1. Synthesis of block copolymer poly-b.

6.2.3 Synthesis of ZnO nanoparticles

Koch et al.^[132] were the first that used a colloidal method for the preparation of ZnO nanoparticles. This was done by hydrolysis of various zinc salts in alcoholic solutions by adding bases. The growth of the nanoparticles was later on studied by Spanhel with $\text{Zn}(\text{OAc})_2 \cdot 2\text{H}_2\text{O}$ as zinc source and LiOH as base with ethanol acting as solvent.^[133] With this basic method in hands, many variations were investigated.^[134,135] Different alcohols were used for the synthesis, but MeOH is probably the best in terms of the polarity. The methyl group is the smallest possible organic rest on the alcoholic functionality. Therefore, bulkier organic rests, e.g. ethyl or isopropyl, reduce the polarity and as a consequence the solubility of the inorganic salts. However, ensuring the solubility of the inorganic components is not the only task of the solvent. By using different alcohols in some cases also the shape of the particles can be regulated because

¹³² Koch, U.; Fojtic, A.; Weller, H.; Henglein, A. *Chem.Phys.Lett.* **1985**, 122, 507

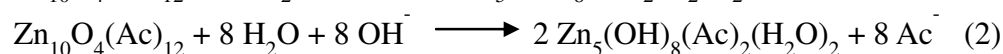
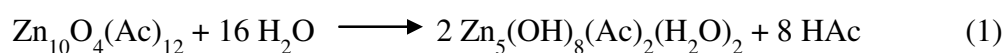
¹³³ Spanhel, L.; Anderson, M.A. *J.Am.Chem.Soc.* **1991**, 113, 2826

¹³⁴ Meulenkamp, E.A. *J.Phys. Chem. B* **1998**, 102, 5566

¹³⁵ Sakohora, S.; Tickanan, L.D.; Anderson, M.A. *J.Phys.Chem.* **1992**, 96, 11086

the alcohol also acts as a ligand. For example, the formation of ZnO nanorods is favored in ethanol, whereas in methanolic solutions particles are formed.^[136]

In this work nanoparticles with a diameter of about 5 nm were synthesized according to a modified literature protocol from Dazhi et al. using $\text{Zn}(\text{OAc})_2 \cdot 2\text{H}_2\text{O}$, KOH, and methanol as solvent.^[137] Meulenkamp was able to show that beside the desired ZnO nanoparticles also a second phase appears called zinc hydroxyl double salt, $\text{Zn}_5(\text{OH})_8(\text{Ac})_2 \cdot 2\text{H}_2\text{O}$.^[134] According to Spanhel the formation of this byproduct can be suppressed by concentrating the reaction solution to 10% of the initial volume by solvent evaporation at 40°C.^[138] This was explained by the following reactions:



$\text{Zn}_{10}\text{O}_4(\text{Ac})_{12}$ is the precursor which leads to the ZnO nanoparticle formation. The solvent evaporation increases the concentration of HAc and Ac^- and therefore shifts the equilibrium of reaction (1) and (2) to the side of the ZnO precursor.

To get pure ZnO nanoparticles several purification steps are necessary. The first is the so called precipitation-redispersion procedure which was first introduced by Meulenkamp.^[134] The crude reaction product is diluted with hexane with a volume ratio of 5:1. Hexane is a non-polar solvent with a polarity index of 0.1, which is low compared to the polar solvent methanol with a polarity index of 5.1. But due to the low miscibility of hexane and methanol the nanoparticles do not precipitate. Therefore, isopropanol was further added with a volume ratio of hexane:methanol:isopropanol of 5:1:1 to ensure the miscibility of methanol and hexane. After the addition, white ZnO nanoparticles precipitate immediately. To ensure a full precipitation the particles are allowed to settle down over night at 0°C. After centrifugation the supernatant is decanted and the particles can be redispersed in methanol. Through this procedure the main impurity, KAc, is removed with an efficiency of 95%, as was shown by atomic absorption spectroscopy (AAS).^[137]

¹³⁶ Pacholski, C.; Kornowski, A.; Weller, H. *Angew.Chem.Int.Ed.* **2002**, 41, 1188

¹³⁷ Dazhi, S.; Minhao, W.; Luyi, S.; Yuntao, L.; Nobuo, M.; Hung-Jue, S. *J.Sol-Gel Sci.Technol.* **2007**, 43, 237

¹³⁸ Spanhel, L. *J.Sol-Gel Sci.Technol.* **2006**, 39, 7

6.2.3.1 Characterization of ZnO nanoparticles

A part of the precipitated ZnO nanoparticles was dried and the crystal modification was identified by XRD measurements. The resulting pattern is depicted in Figure 65. The observed crystal modification is Wurtzite. The corresponding Miller indices for the peaks were assigned and are also shown in Figure 65. The average primary crystallite size according to the Scherrer equation is 5.5 nm.

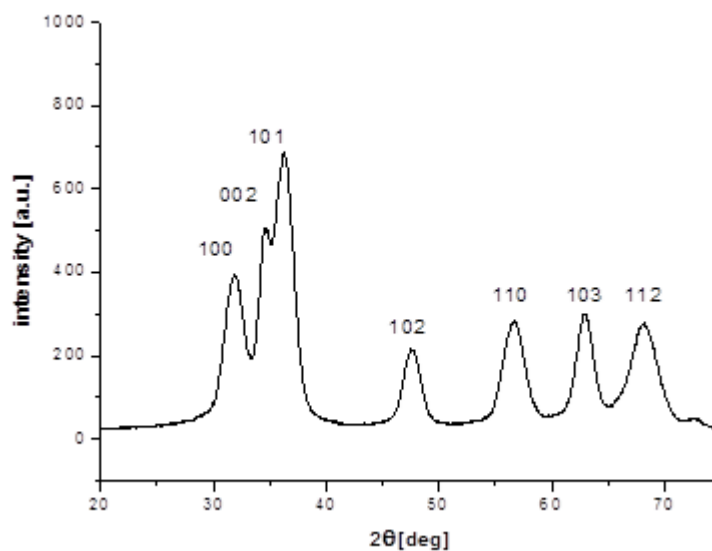


Figure 65. XRD pattern of ZnO nanoparticles with corresponding miller indices.

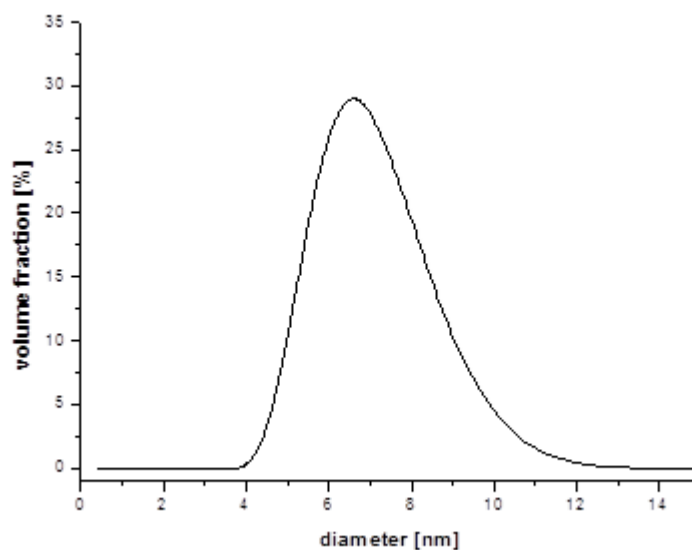


Figure 66. Dynamic light scattering results of ZnO nanoparticles in MeOH.

The size estimated by the Scherrer equation matches the results from dynamic light scattering (Figure 66), directly measured from the reaction solution quite well with a diameter of 6.5 nm. The optical properties will be discussed in Chapter 5.2.4.2.

6.2.4 Photophysical characterization

6.2.4.1 Combination of platinum dye and block copolymer

In Figure 67 the absorption spectrum of the charged platinum complex is depicted. In methanol solution, the complex shows several intense absorption bands at $\lambda < 400$ nm with high extinction coefficients ranging from about 8000 to 47000 $\text{cm}^{-1} \text{M}^{-1}$, which are assigned to intraligand transitions (IL) of the 1,10-phenanthroline and 3-hexyloxy-2-phenylpyridine ligands.^[122] In addition, the complex exhibits a broad and structureless band ranging from 409 to 482 nm with extinction coefficients of 300 to 5100 $\text{cm}^{-1} \text{M}^{-1}$. This broad absorption is assigned to a transition from a 5d-orbital of the platinum to the π^* orbital of the phenanthroline ligand.

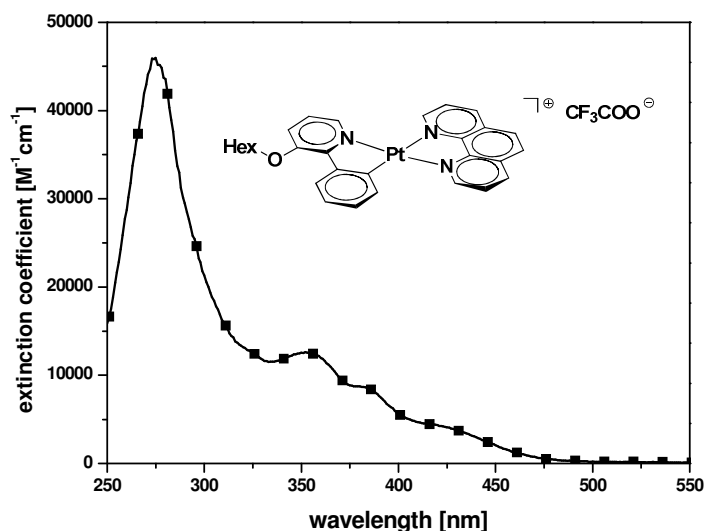


Figure 67. Absorption spectrum of a methanol solution of the platinum dye ($c = 1.375 \cdot 10^{-6} \text{ mol/L}$).

In Figure 68 a comparison between the absorption spectra of a pure platinum complex solution in methanol and a solution where also polymer was added is shown. The

combination of both materials results in an additional absorption in the area from 475 to 575 nm.

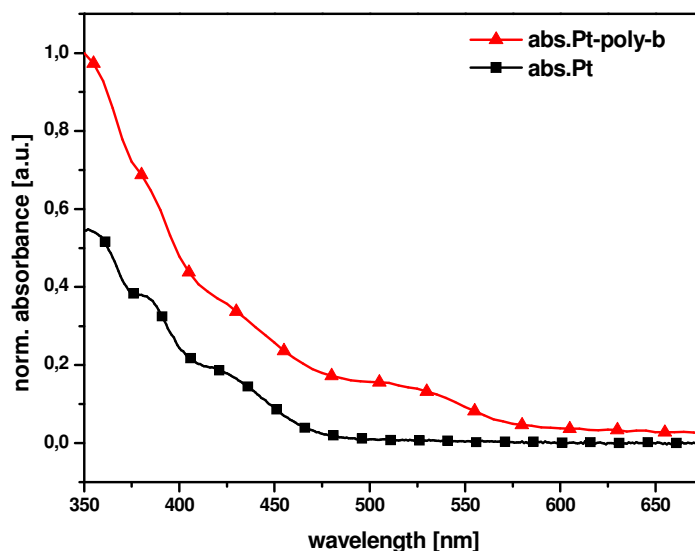


Figure 68. Comparison of absorption of a methanol solution of the pure platinum complex and in a mixture with the block copolymer, poly-b.

The corresponding emission spectra of pure platinum complex, compared to the one of the platinum-poly-b-combination, are shown in Figure 69. Significant differences can be observed. In the case of Pt-poly-b an intense and very broad luminescence signal peaking around 644 nm can be observed, the pure platinum complex solution is not luminescent due to radiationless deexcitation processes.

It is worth mentioning that such platinum complexes tend to form aggregates, stabilized by platinum-platinum interactions, which result in significant red shifts relative to the mononuclear emission spectra.^[124] The square planarity of platinum chromophores results in intermolecular stacking, aggregation, and excimer/dimer formation in concentrated solutions as well as in the solid state.^[139,140,122] This is the reason for the differences between diluted solution, more concentrated solution and solid-state luminescence spectra of platinum complexes.^[141]

¹³⁹ Farelly, S. J.; Rochester, D. L.; Thompson, A. L.; Howard, J. A. K.; and Williams, J. A. G. *Inorg. Chem.* **2005**, *44*, 9690.

¹⁴⁰ Ma, B.; Li, J.; Djurovich, P.I.; Yousufuddin, M.; Bau, R.; Thompson, M.E. *J. Am. Chem. Soc.* **2005**, *127*, 28.

¹⁴¹ Ionkin, A. S.; Marshall, W. J.; Wang, Y. *Organometallics* **2005**, *24*, 619.

A schematic illustration which describes the origins of these differences is given in Scheme 2. The blue-green line represents the polymer and the green symbols represent the acid-groups. After adding the complex to the polymer the platinum-dyes coordinate to the acid groups and, if they are in close proximity, exhibit a fluorescence signal due to the aforementioned excimer formation. Those excimers are represented by yellow squares. The molecules which have no neighbor within a certain space limit, are, like the dyes in solution, not fluorescent (turquoise squares).

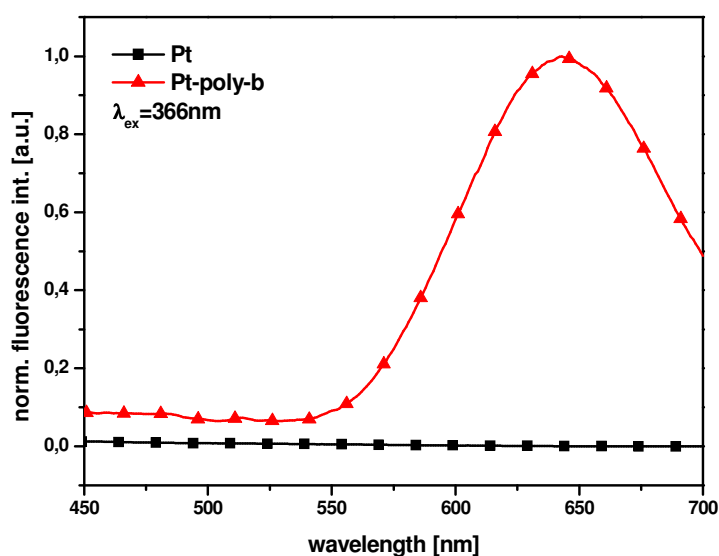
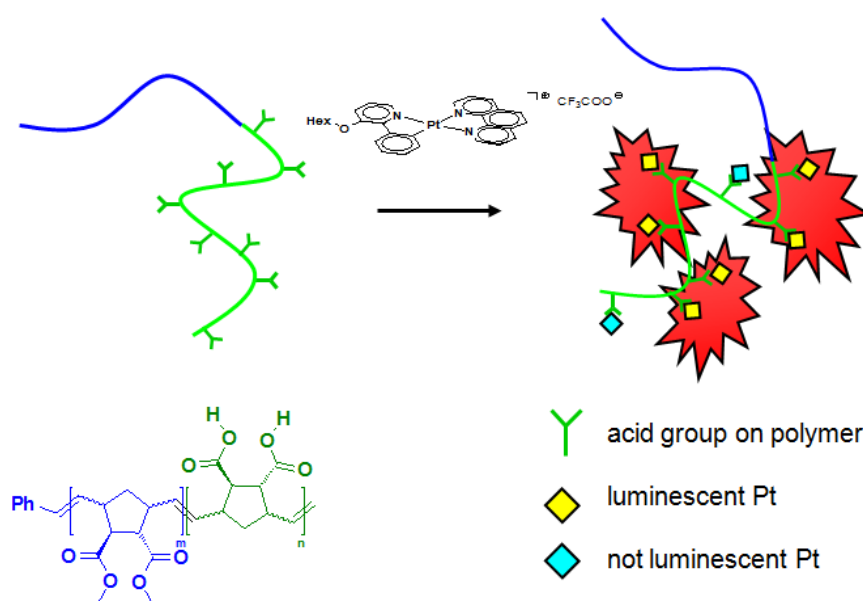


Figure 69. Comparison of emission spectra of a methanol solution of the pure platinum complex and in a mixture with the block copolymer; $\lambda_{\text{ex}} = 366$ nm.



Scheme 2. Schematic illustration of the platinum complex coordination to the polymer.

In Figure 70 a typical titration experiment is depicted, where platinum complex was added step-by-step to 500 μL of the polymer. The excitation wavelength in each case was 535 nm. This addition leads to the formation of excimers and therefore results in the rising peak at 650 nm.

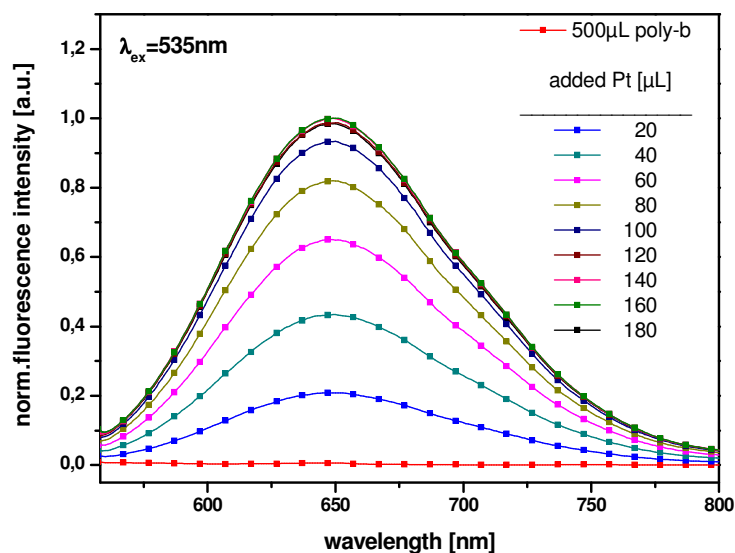


Figure 70. Comparison of emission spectra of a methanol solution of the block-copolymer with increasing amounts of platinum; $\lambda_{\text{ex}} = 535$ nm.

In Figure 71 the same results are shown but in this case the fluorescence intensity at a wavelength of 650 nm is plotted against the volume of platinum on the lower x-axis. The intensity reaches a certain maximum at about 160 μL which corresponds to 13 platinum molecules per polymer, as shown on the upper x-axis. This implies that only a small fraction of the theoretically available 80 acid groups per polymer chain coordinate to the complex.

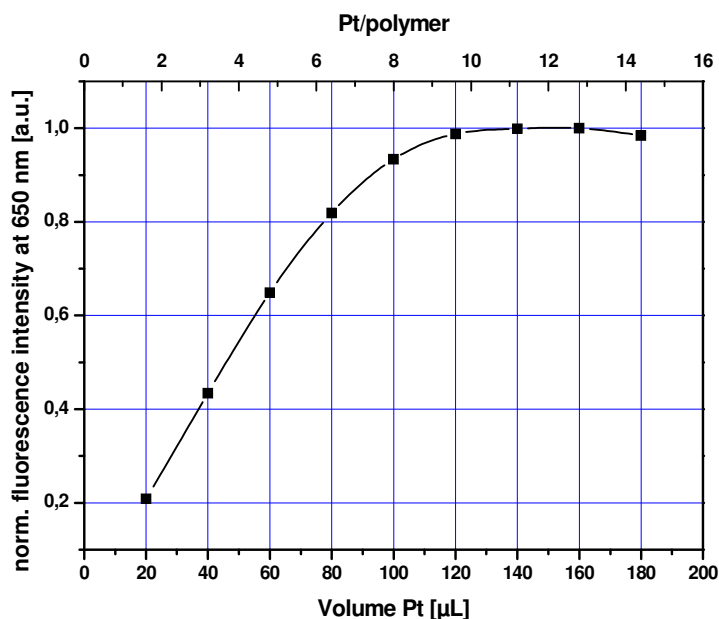


Figure 71. Increase of emission intensity at 650 nm with increasing amount of platinum.

Dynamic light scattering (DLS) measurements in MeOH ($c=0.12$ mg/mL) showed that the polymer exhibits an average size diameter of 140 nm (see Table 12). The theoretical size of a polymer chain is 52.1 nm. This means that aggregates are present so that it can be assumed that not all of the acid groups are available for the coordination of the platinum dye. Besides, considering the size of the complex also steric arguments can be used to explain the rather poor coordination yield.

Table 12. Dynamic light scattering measurements of poly-b in MeOH; $c=0.12$ mg/mL.

measurement number	diameter [nm]	PDI_{DLS}
1	133	0.237
2	146	0.251
3	141	0.243

6.2.4.2 ZnO nanoparticles and polyelectrolyte

In Figure 72 the absorption (black line) and emission (red line) spectra of ZnO nanoparticles in methanol are shown. The absorption onset is at 350 nm with a first maximum at 325 nm. The black curve shows that the particle emission consists of two parts. First, the nanoparticles exhibit a small emission signal centered around 372 nm, corresponding to an energy of 3.33 eV. It was assigned to the near band edge emission of the particles by Kahn et al.^[142] The high intensity region in the visible range centered

around 512 nm, corresponding to an energy of 2.42 eV, was attributed to single ionized oxygen vacancies. It arises from the recombination of deep trapped holes and electrons from an energy level which is slightly below the conduction band.

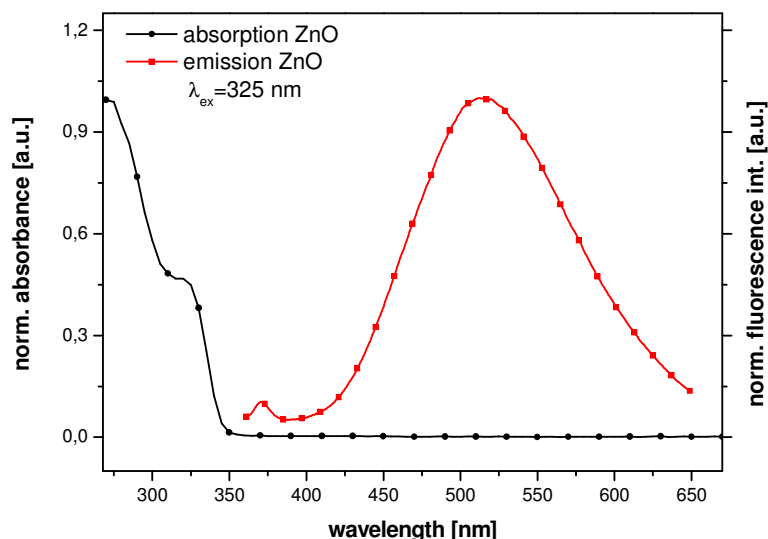


Figure 72. Absorption and emission from a ZnO nanoparticle solution in MeOH;
 $c = 0.03$ mg/mL.

It is a known fact that molecules with polar head groups are able to coordinate to nanoparticle surfaces. Typical examples are alkyl amines^[142], alkyl thiols^[143], or carboxylic acids.^[144] In the present work the affinity of ZnO nanoparticles to the carboxylic acid groups of the block copolymer (poly-b) was used for coordination.

This process was investigated by recording emission spectra upon the addition of increasing amounts of the polymer to the nanoparticle solution. To 500 μ L ZnO solution with a concentration of 0.03 mg/mL the polymer solution with a concentration of 0.1 mg/mL was added in 100 μ L steps. The corresponding emission spectra were recorded using an excitation wavelength of 332 nm and are depicted in Figure 73. The response of the two afore mentioned emission signals to the polymer is different. While the defect peak decreases in intensity the band edge peak slightly rises.

¹⁴² Kahn, M.L.; Monge, M.; Colliere, V.; Senocq, F.; Maisonnat, A.; Chaudret, B. *Adv.Funct.Mater.* **2005**, 15, 458

¹⁴³ Pesika, N.S.; Hu, Z.; Stebe, K.J.; Searson, P.C. *J.Phys.Chem.B* **2002**, 106, 6985

¹⁴⁴ Sakohara, S.; Ishida, M.; Anderson, M.A. *J.Phys.Chem.B* **1998**, 102, 10169

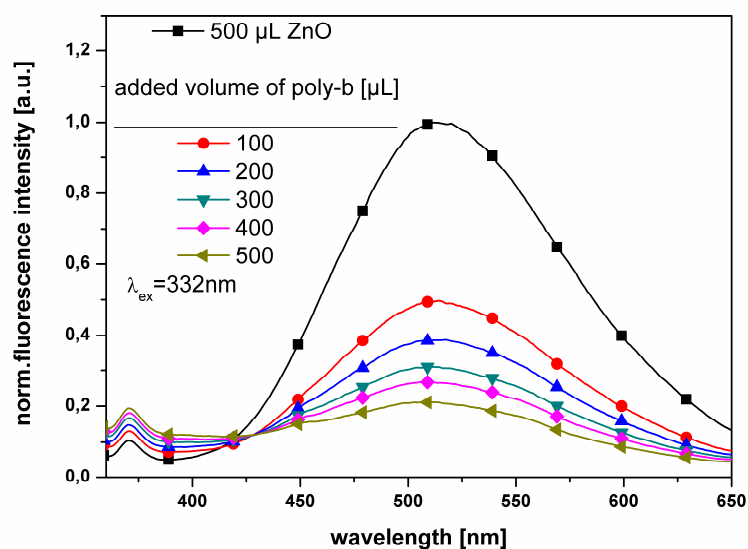
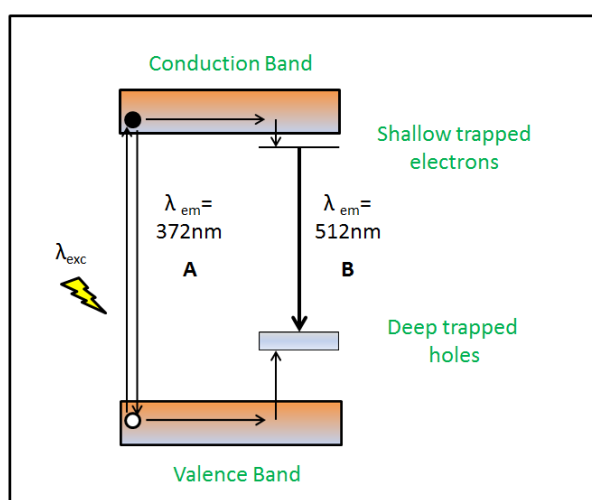


Figure 73. Changes in nanoparticle emission behavior upon the addition of poly-b;
 $\lambda_{\text{ex}} = 332 \text{ nm}$; $c(\text{poly-b})$: 0.1 mg/mL; $c(\text{ZnO}) = 0.03 \text{ mg/mL}$.

These observations are summarized and explained in Scheme 3. The addition of polyacids, or in general substances able to coordinate to the particle surface, lead to an occupation of defect sites. The probability of transitions is proportional to the number of available energy states. As a consequence, reducing the number of states makes the transition A (near band edge emission) more probable, which means that a rise in intensity can be observed, whereas the transition B (emission from trap states) decreases in intensity. So these findings indicate a coordination of the polymer to the nanoparticle surface.



Scheme 3. Possible emission mechanisms of ZnO nanoparticles.

6.2.4.3 ZnO nanoparticles and Pt-dye with copolymer

So far, the experiments show that the platinum dyes and the ZnO nanoparticles are able to coordinate to the polymer. Therefore, in the next step the attention was focused on the question, what happens if both types of material are offered to the polymer. This is of particular interest because, as shown in Figure 74 the emission of the ZnO nanoparticles overlaps with the absorption of the platinum excimers which were formed during the coordination to the polymer. Due to this overlap the used system is a candidate for an energy transfer from the ZnO nanoparticles to the platinum dyes.

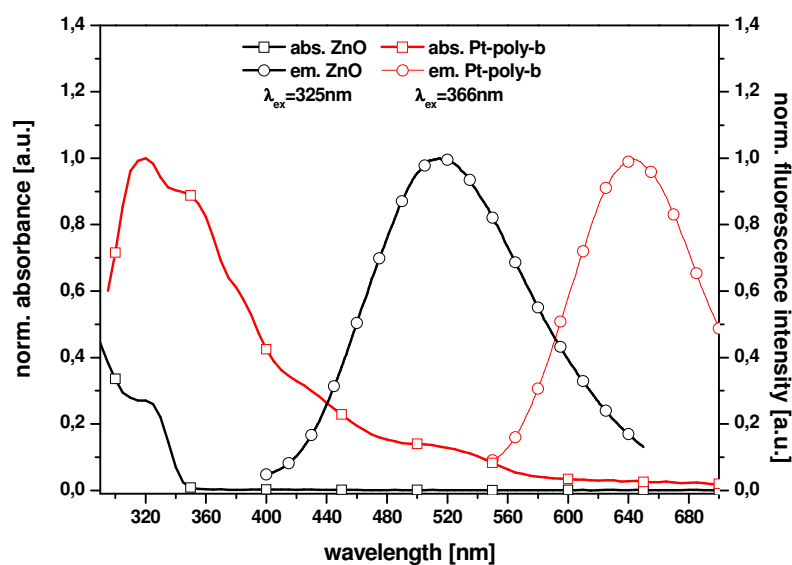


Figure 74. Comparison of absorption and emission spectra of ZnO ($\lambda_{\text{ex}} = 325$ nm) and Pt-poly-b ($\lambda_{\text{ex}} = 366$ nm).

To investigate if an energy transfer occurs, ZnO nanoparticles were added to the block copolymer, which previously has been saturated with platinum complex. The sample was excited at 325 nm, which corresponds to the absorption maximum of the nanoparticles. The results are shown in Figure 75. Comparison of emission spectra of a methanol solution of Pt-poly-b with increasing amounts of ZnO; $\lambda_{\text{ex}} = 325$ nm; see inset for concentrations. (the emission intensity of the platinum dye - polymer combination was set to 1). As can be seen, the emission intensity corresponding to the platinum excimer initially increases reaches a maximum at about 40 μL and decreases again after that. Furthermore, it is worth mentioning that no or only a weak signal from the particle emission can be seen, even at a large excess of 400 μL of nanoparticles.

Figure 76 again shows the fluorescence intensity at 636 nm plotted against the volume of nanoparticles. In this type of plot it is clearly shown that the excimer emission intensity is increased over 300%.

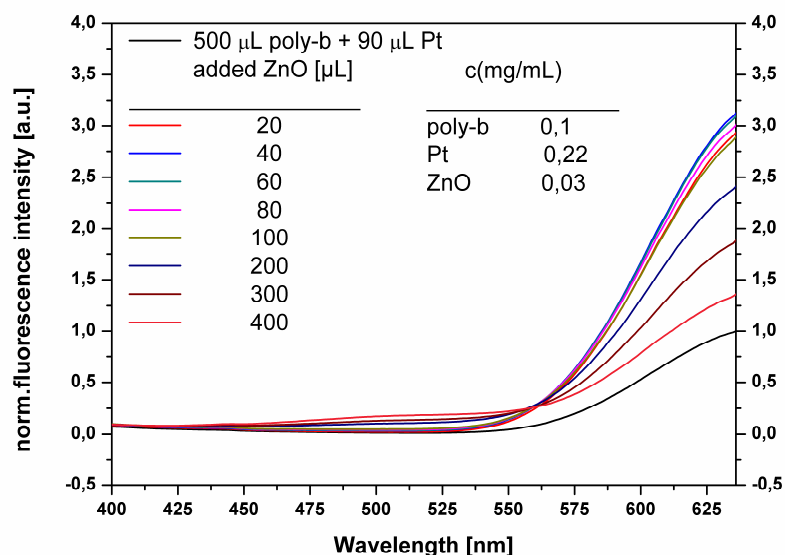


Figure 75. Comparison of emission spectra of a methanol solution of Pt-poly-b with increasing amounts of ZnO; $\lambda_{\text{ex}} = 325 \text{ nm}$; see inset for concentrations.

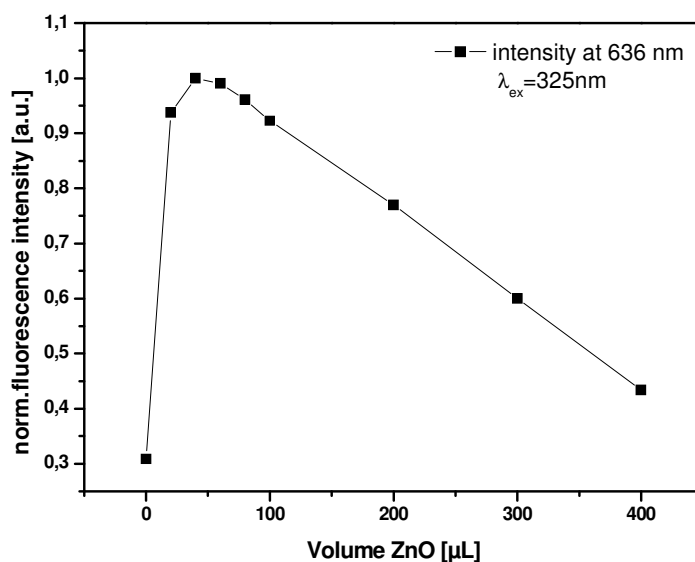
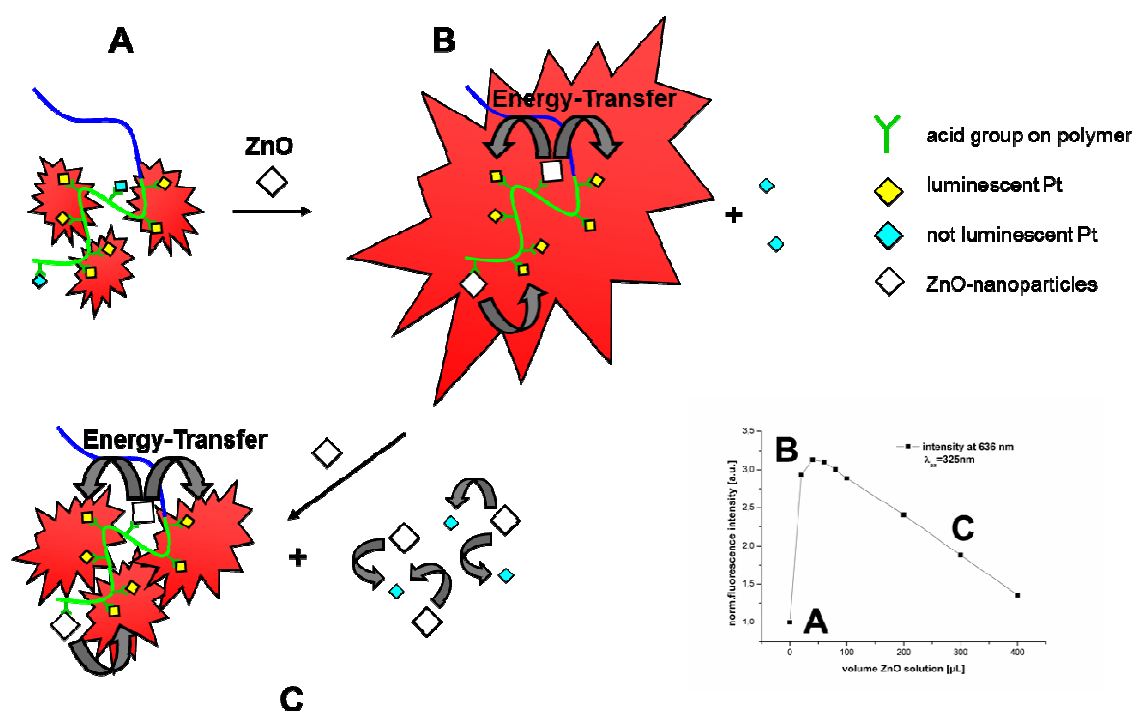


Figure 76. Increase of emission intensity at 636 nm with increasing amount of ZnO.

The increase of emission intensity is a strong evidence of the occurring energy transfer. The overall process is illustrated in Scheme 4. In this scheme the expected processes are shown together with the characteristic points of the intensity - volume plot. Point A, as described previously, shows the polymer, saturated with platinum complexes. In the

next step the nanoparticles were added, which partially substitute platinum from the polymer. This leads to a close proximity of ZnO nanoparticles and platinum excimers, allowing an energy transfer to occur, as can be seen by the rise of the emission intensity. At some point the optimal amount of nanoparticles adjacent to the platinum dye on the polymer is reached, which corresponds to point B. Through further addition of particles to the system, no more free coordination locations on the polymer are left and these particles are therefore in solution, like the substituted platinum dyes. Of course, these particles in solution also absorb light and therefore less energy is left for the particles on the polymer to transfer energy to the dyes on the polymer. As a consequence, the emission intensity decreases. Because the particles in solution also absorb light, one would assume that these particles also emit light in the typical emission region of the particles. The observations showed that this does not happen, or more precisely, only with a very low intensity. This could mean, that there is also an energy transfer in solution, with the difference that the dyes in solution do not emit light because they cannot form excimers, but lose this energy in a non-radiative way. To confirm this theory some points of the argumentation have to be verified. At first, another experiment showing the coordination of the particles to the polymer was performed.



Scheme 4. Schematic illustration of the processes involved in the energy transfer.

In this experiment the platinum complex was added to a solution consisting of polymer and nanoparticles (Figure 77). The resulting solution was excited with a wavelength of 325 nm, the absorption maximum of the particles. Independent of the amount of platinum, no excimer emission is visible in the region of 636 nm. The only observable effect is the decrease of emission intensity from the nanoparticles. Due to the irregular decrease of the intensity, one can get first hints towards an energy transfer from the particles to the dyes. So, this experiment allows the deduction that there are no free sites left on the polymer due to the coordination of the particles to the acid-groups because otherwise the platinum complexes would have formed excimers.

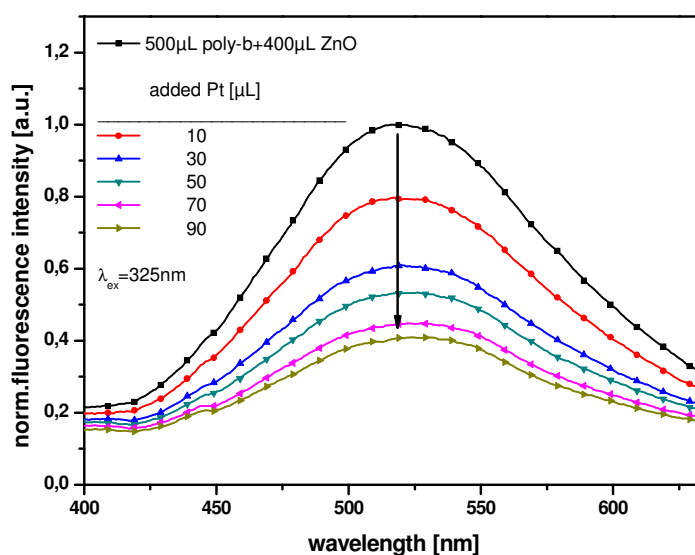


Figure 77. Comparison of emission spectra of a methanol solution of block copolymer and ZnO with increasing amounts of platinum; $\lambda_{\text{ex}} = 325 \text{ nm}$; $c(\text{Pt})$: 0.22 mg/mL; $c(\text{poly-b})$: 0.1 mg/mL; $c(\text{ZnO}) = 0.03 \text{ mg/mL}$.

Finally the quenching of the ZnO nanoparticle emission by the platinum dye has to be discussed. In general, different cases in which an excited molecule M^* can be de-excited by a quenching molecule Q can be identified.

If there is no large excess of Q and the approach of M^* and Q is possible during the excited state lifetime, the principles of dynamic quenching are valid. This process is often called collisional quenching, because it assumes that the de-excitation occurs

through collisions between emitter and quencher. This case is described within the kinetic model introduced by Stern and Volmer.^[145]

$$\frac{I_0}{I} = 1 + K_{SV} [Q] \quad (9)$$

I_0 ...emission intensity of the luminescent material in the absence of the quenching molecule

I ... emission intensity of the luminescent material in the presence of the quenching molecule

K_{SV} ...Stern-Volmer constant

$[Q]$...concentration of quencher

The ratio of I_0/I is plotted against the quencher concentration. If the variation is found to be linear, the slope gives the Stern-Volmer constant.

If there is a large excess of Q, the probability that M^* and Q meet within the lifetime of the excited state of Q is significant. This case is relevant for static quenching. The model of static quenching is appropriate to use if M^* and Q form a non-fluorescent complex. Considering that the platinum dye is positively charged with trifluoroacetate as counterion a certain tendency to stick to the nanoparticle surface due to interactions with either defect sites or the surface coordinated acetate ions cannot be excluded. According to a model, introduced by Perrin^[146] the luminescence signal is quenched completely if Q is located inside a certain sphere of volume V_q surrounding the fluorophore M. This sphere is also called the sphere of effective quenching. A quencher molecule Q outside this sphere has no effect at all. This is the reason why the intensity of fluorescence is decreasing through the addition of Q, but the fluorescence decay after pulse excitation is unaffected, in contrast to dynamic quenching. The model leads to the following equation:

$$\frac{I_0}{I} = e^{V_q N_a [Q]} \quad (10)$$

Contradictory to dynamic quenching a plot of intensity ratio against the concentration of Q in this case leads to an upwards curvature. However, at low concentrations the right

¹⁴⁵ Turro, N.J. *Modern Molecular Photochemistry*, Benjamin, W.A., New York, **1978**

¹⁴⁶ Birks, J.B. *Photophysics of aromatic molecules*, Wiley-Interscience, New York, **1970**

side of equation 10 can be approximated through $1 + V_q N_a [Q]$ and therefore also leads to a linear dependence.

To proof the quenching of the nanoparticle emission, the platinum dye ($c = 0.22$ mg/mL) was added successively to 500 μL of ZnO nanoparticle solution ($c = 0.03$ mg/mL). The normalized luminescence signal at 525 nm after excitation of 325 nm upon the addition is depicted in Figure 78 (black line). The curve shows a steep decrease in intensity at small volumes which flattens out at higher volumes. It should be noted that the volume is proportional to the concentration of the quencher. According to this result one would assume that static quenching occurs in this case. However, up to now a second effect was neglected: the dilution of the initial solution. The red curve in Figure 78 shows the response of the luminescence upon the addition of the solvent methanol. In this case the intensity decreases due to dilution.

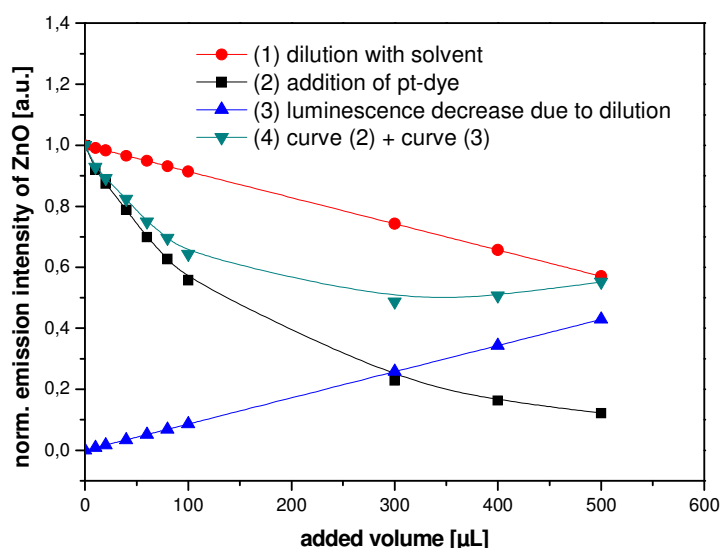


Figure 78. Emission intensity decrease of ZnO nanoparticles by dilution and quenching.

As a consequence curve (2) has to be interpreted as a combination of both effects. To assess the region that is dominated by quenching the dilution effect has to be subtracted from the quenching curve. Since both, dilution and quenching are pointing towards lower intensities a simple mathematical procedure was applied to better visualize this subtraction. The blue curve shows the emission intensity loss at a certain volume of added solvent. Addition of this curve to the black curve leads to the green curve in Figure 78, which passes through a minimum at a volume of 300 μL . This means that from this point the effect of dilution dominates the decrease in emission intensity.

Consequently, the models of dynamic or static quenching must not be applied over the whole region but only to the region on the left from the minimum.

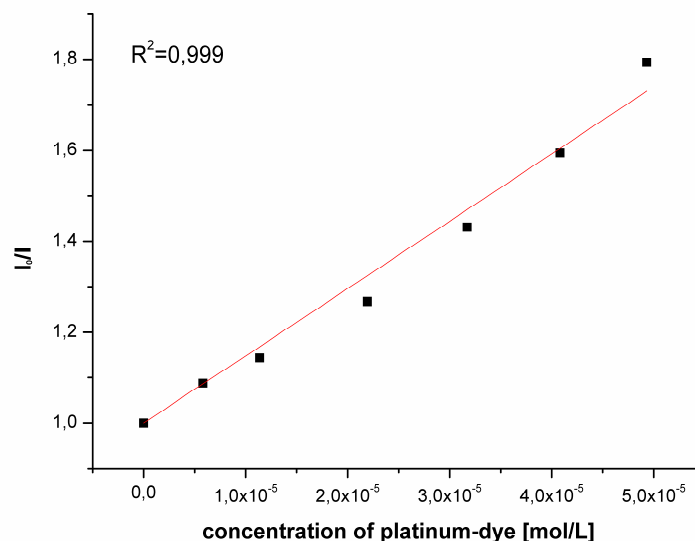


Figure 79. Plot of intensity ratio versus concentration of the platinum-dye.

The plot of intensity ratio against the concentration of the platinum-dye is depicted in Figure 79. The obtained relation is linear with a R^2 -value of 0.999. Up to this point it is clear that the emission of the nanoparticles is quenched by the platinum-dye, but the exact nature of this process remains unclear. Both, dynamic and static quenching are possible. Through lifetime measurements after pulse excitation the process could be assigned to one of them.

Additionally, it could be that the emission decreases through an energy transfer. As depicted in Figure 80 the emission of the nanoparticles also has a small region of overlap with the absorption of the platinum complex between 400 and 480 nm. However, to sum up, it was clearly demonstrated that the emission of the particles decreases upon the addition of the platinum dye in solution, although the involved processes cannot be clarified by simple emission measurements.

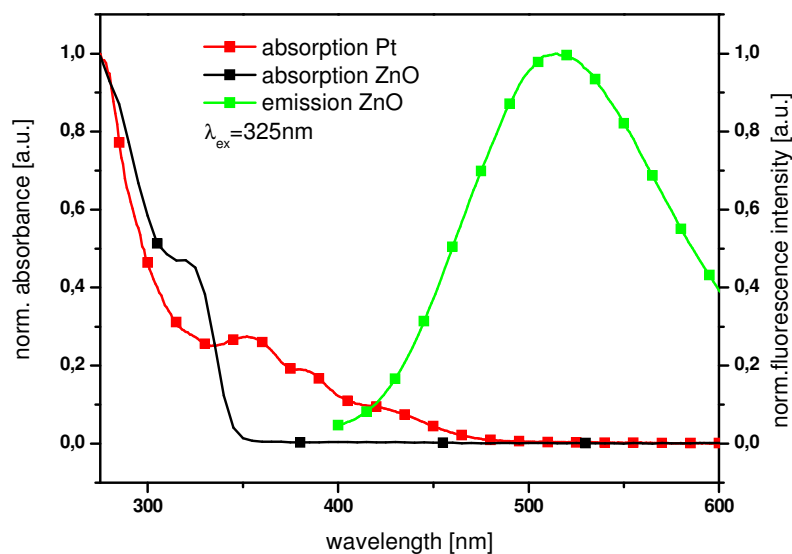


Figure 80. Comparison of absorption and emission spectra of ZnO ($\lambda_{\text{ex}} = 325 \text{ nm}$) and Pt-complex.

6.2.4.4 Influence of polymer concentration

As was shown in Figure 73, the presence of the polymer leads to a decrease of the nanoparticle emission through the coordination of acid groups to trap states on the nanoparticle surface. Therefore it can be expected that the ratio of polymer to nanoparticle has a dramatic effect on the efficiency of the energy transfer.

For this reason 500 μL of polymer solutions with concentrations between 0.1 and 1.0 mg/mL were saturated with platinum dyes. The maximum in excimer emission intensity was reached after the addition of 60 μL for the polymer solution with a concentration of 0.1 mg/mL, 110 μL for 0.5 mg/mL and finally 160 μL for 1 mg/mL. In the next step ZnO nanoparticles with a concentration of 0.03 mg/mL were successively added until the maximum in the emission intensity was passed. The possible intensity increase of these experiments is depicted in Figure 81. From this simple experiments it was observed that a relative low concentration of 0.1 mg/mL is superior compared to 0.5 and 1 mg/mL. No significant difference can be observed between the two higher concentrations.

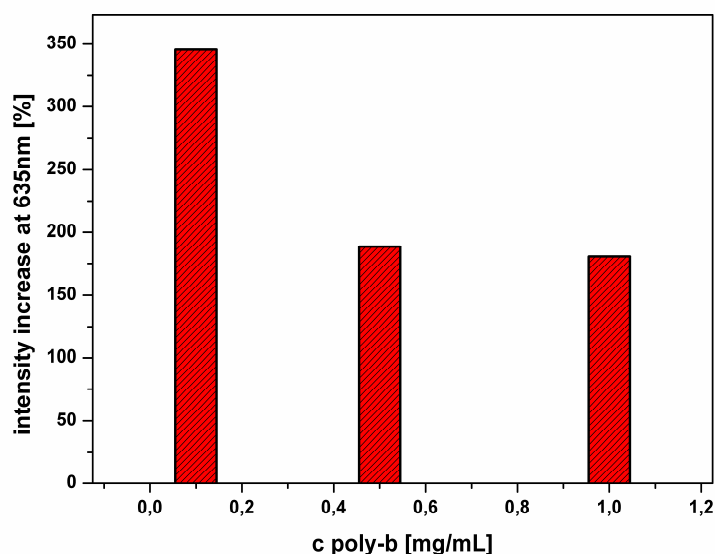


Figure 81. Influence of the increase of excimer emission intensity at 635 nm on the polymer concentration; $\lambda_{\text{ex}} = 325$ nm, $c(\text{Pt}) = 0.15$ mg/mL, $c(\text{ZnO}) = 0.06$ mg/mL.

In Figure 82 the average of the absolute emission intensities at 635 nm as well as the corresponding standard deviations after the addition of ZnO nanoparticles, determined by three measurements, are plotted against the polymer concentration. It was observed, that the intensity is proportional to the polymer concentration, which is evident due to higher excimer concentration in solution. However, the values are more reproducible by using polymer solutions of higher concentration.

To sum up, the energy transfer will be more efficient if the low concentration regime is approached, although the absolute intensity values are significantly lower due to a decreased excimer concentration. The efficiency of the transfer can be explained by the ratio of polymer to particle concentration. Higher polymer concentrations decrease the nanoparticle emission as was explained in chapter 6.2.4.2. For this reason less energy is left to be transferred to the platinum-complex, resulting in a less pronounced energy transfer. On the other hand, if the low concentration regime is approached, the standard deviation of the measurements will increase.

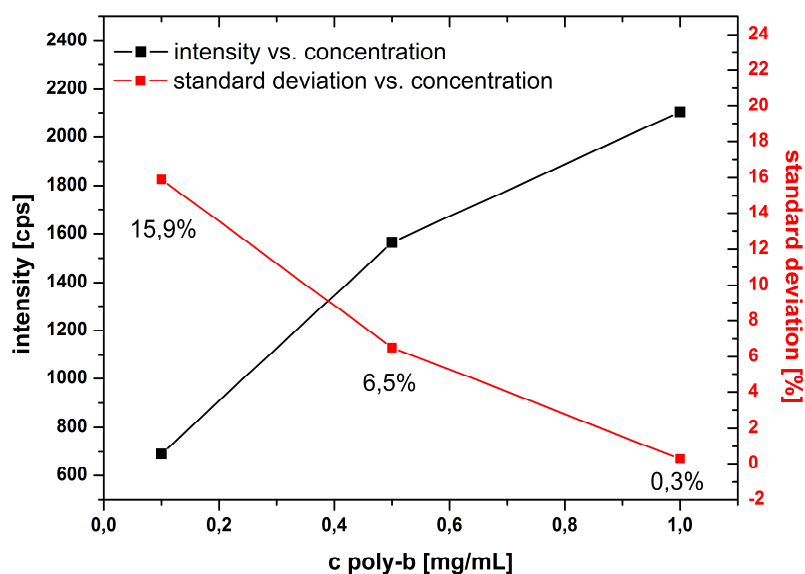


Figure 82. Absolute emission intensity (black curve) and standard deviation (red curve) as a function of the polymer concentration; $\lambda_{\text{ex}} = 325 \text{ nm}$, $c(\text{Pt}) = 0.15 \text{ mg/mL}$, $c(\text{ZnO}) = 0.06 \text{ mg/mL}$.

6.2.4.5 Influence of KOH

ZnO nanoparticles, used for the experiments were taken directly from the reaction solution. Due to the fact that the yield of the reaction is lower than 100% also minor concentration of the base KOH are still present in the reaction solution. Because it is expected that the polymer poly-b is sensible towards variations in the pH-value the influence of KOH was investigated. Differences in the aggregation properties of poly-b by the addition of nanoparticle solution and a solution of KOH, dissolved with a concentration of 0.056 mg/mL in methanol were investigated by DLS and photoluminescence measurements. The concentration of the KOH is the same as in the nanoparticle solution by assuming a yield of 50%. The results of the DLS measurements are depicted in Figure 83.

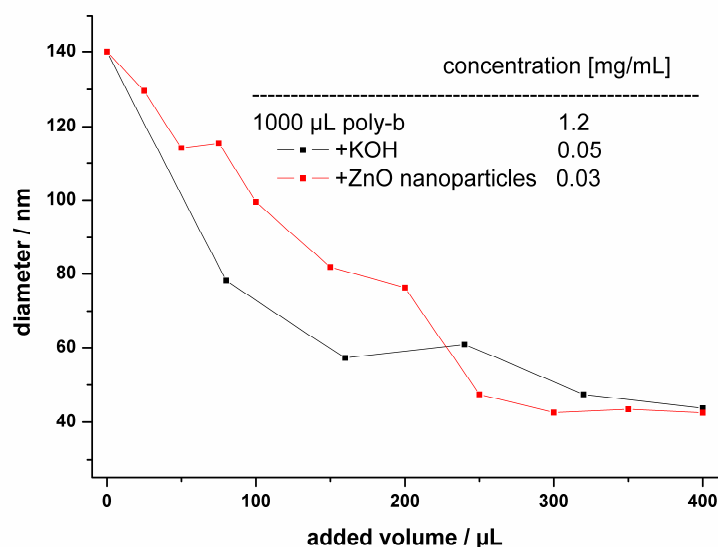


Figure 83. DLS experiments of the titration of poly-b with KOH and ZnO nanoparticles.

As previously described (chapter 1.2.4.1) poly-b is agglomerated with an average agglomeration size of around 140 nm. The final size of the polymer, after the addition of 400 μL of KOH with a concentration of 0.05 respectively 400 μL of ZnO nanoparticles with a concentration of 0.03 mg/mL, is around 45 nm. This corresponds quite well with the theoretical size of 52 nm, calculated by the addition of the length of 80 monomer units. Therefore in both cases the agglomerates are cracked. In the case of KOH this is probably achieved through the repulsive electrostatic interaction of the deprotonated acid groups. The addition of ZnO nanoparticles yields bigger structures compared to KOH up to a volume of 200 μL . This might be due to the coordination of the polymer to the particles resulting in linked structures. Further addition leads to the fully deprotonated polymer form and reduces thereby the coordination ability of the polymer. To investigate the influence of KOH on the platinum excimer emission intensity, the KOH solution with a concentration of 0.05 mg/mL was added step by step to 500 μL of the polymer solution ($c = 1.2$ mg/mL) that was saturated with 100 μL of the platinum dye solution ($c = 0.15$ mg/mL). The excitation wavelength was, as in the case of the ZnO nanoparticles, 325 nm, and the emission intensity at 635 nm was measured. The results are depicted in Figure 84.

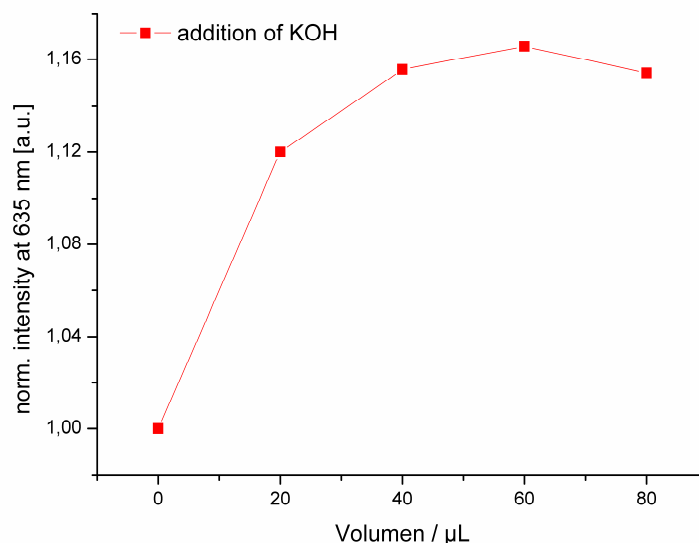


Figure 84. Signal increase of excimer emission upon the addition of KOH.

In this case as well, the excimer emission intensity increases upon the addition of KOH. But the maximum obtainable signal increase is limited to around 16%, which is compared to >300% rather low. This increase might be attributed to the breaking of polymer aggregates, ensuring more coordination of platinum dyes on the polymer. However, to sum up this point, also the KOH which is present in the used nanoparticle solutions increases the excimer emission intensity. But the increase is rather low (16%) and may be attributed to improved excimer formation on the polymer. The rise of 300% in the signal intensity can only be explained by the energy transfer occurring between the defect emission of the particles overlapping with the excimer absorption of the platinum dyes.

6.3 ZnO nanoparticle based sensing of Cu(II)-ions

The interesting optical properties of ZnO nanoparticles, like the strong fluorescence signal, the large Stokes shift and their response to external stimuli make their application as fluorescent reporters possible. But also the combination of the block copolymer, poly-b, and the platinum-dye is expected to work as a sensing material combination, useful in the detection of known fluorescence quenchers like Cu^{2+} ions. Cu^{2+} is a significant environmental pollutant and an essential trace element in biological systems. Therefore the selective and sensitive detection of Cu^{2+} is of high interest.^[147] In this chapter both systems and combinations are tested regarding their response to Cu^{2+} ions.

Therefore, in the first experiment the luminescent platinum excimers situated on the polymer chain, obtained through the addition of 100 μL of the platinum complex with a concentration of 0.165 mg/mL to 500 μL of the polymer with a concentration of 0.11 mg/mL, were mixed with a $\text{Cu}(\text{OAc})_2$ solution in methanol with a concentration of 0.535 mg/mL which was successively added. The excimers were excited at 366 nm which corresponds to the absorption maximum and the response of the emission was detected. As depicted in Figure 85 already after 10 μL of copper solution the luminescence signal decreased to around 18% of its initial value. After 20 μL it is completely quenched.

In Scheme 5 the two possible reasons for this observation are shown. On the one hand it is possible that the platinum dyes (yellow squares for excimers and turquoise for single dyes) are simply substituted by the copper ions. On the other hand Cu^{2+} is a well-known and efficient fluorescence quencher due to its paramagnetic properties.^[147] Most probable, the observed decrease of the intensity may be attributed to a combination of both mechanisms. Especially the involved substitution mechanism makes the potential sensor application not selective because also other ions are able to substitute the platinum dyes on the polymer. Therefore an alternative strategy was followed.

¹⁴⁷ Shang, L.; Dong, S. *J.Mater.Chem.* **2008**, 18, 4636

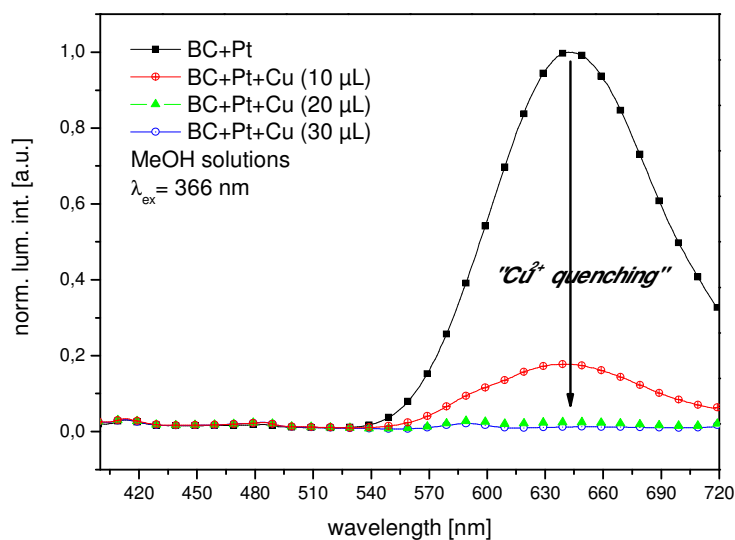
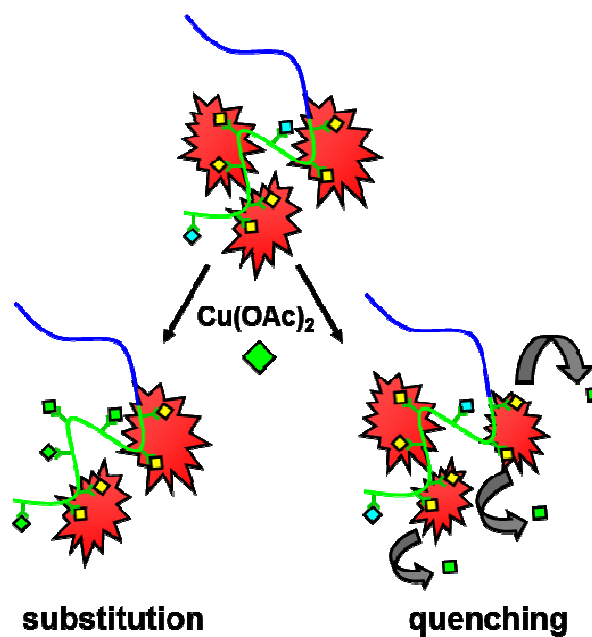


Figure 85. Comparison of emission spectra of a methanol solution of the Pt-poly-b with increasing amounts of Cu^{2+} (0.535mg/mL); $\lambda_{\text{ex}} = 366\text{nm}$, $c(\text{poly-b}) = 0.11\text{mg/mL}$, $c(\text{Pt}) = 0.165\text{mg/mL}$.



Scheme 5. Schematic mechanisms of the quenching process.

As shown in Figure 86 the copper ions also quench the emission of ZnO nanoparticles. In the case of Cu^{2+} - addition both emission signals, described in chapter 6.2.4.2, decrease. This indicates an energy or electron transfer from the particles to the copper ions.

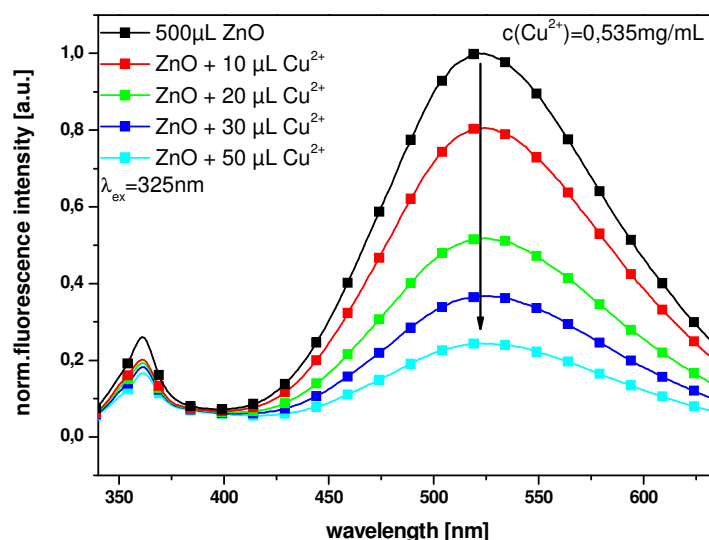


Figure 86. Comparison of emission spectra of a methanol solution of ZnO with increasing amounts of Cu^{2+} ; $\lambda_{\text{ex}} = 325\text{nm}$, $c(\text{ZnO}) = 0.03\text{ mg/mL}$.

As shown in Figure 87, addition of 100 μL of polymer solution prior to copper ions leads to a more pronounced emission signal decrease. This improved response is valid mainly in the low concentration regime of copper ions.

For better visibility the intensity of the trap emission at a wavelength of 512 nm for both experiments is plotted against the volume of copper solution in Figure 88(left). As can be seen the slope in the case of the combination of nanoparticles and block – copolymer is much steeper in the low concentration regime. Approaching higher copper contents the response of both systems assimilates. This observation is confirmed in the two corresponding Stern-Volmer plots on the right side of Figure 88. The Stern-Volmer constant is with 103200 L/mol in the case of the nanoparticle polymer combination significant bigger compared to 59200 L/mol, obtained by using only ZnO.

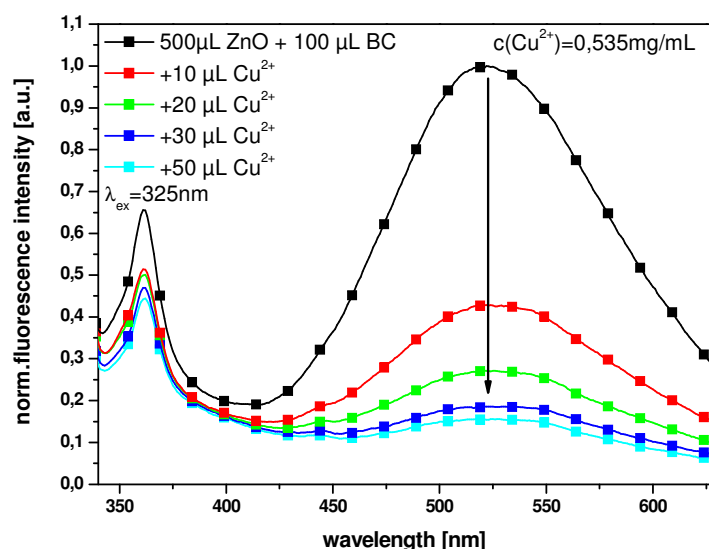


Figure 87. Comparison of emission spectra of a methanol solution of ZnO with poly-b and increasing amounts of Cu^{2+} ; $\lambda_{\text{ex}} = 325\text{nm}$; $c(\text{ZnO}) = 0.03\text{ mg/mL}$; $c(\text{poly-b}) = 0.11\text{ mg/mL}$.

This observation may be explained by the following argumentation. The block copolymer coordinates to the particle surface, but some acid groups are free and able to coordinate to the added copper ions. It is already known from previous reports that Cu^{2+} ions tend to coordinate to free carboxylic groups.^[148] This situation ensures a close contact of the emitting particles and the quenching reagent. As is known for a long time from the theory of luminescence quenching the efficiency of the process is distance dependent^[149], making the setup of the experiment 2 advantageous.

¹⁴⁸ Shang, L.; Dong, S. *J.Mater.Chem.* **2008**, 18, 4636

¹⁴⁹ Rice, S.A. *Diffusion-Limited Reactions*, Comprehensive Chemical Kinetics, Vol. 25, edited by C. H. Bamford, C. F. H. Tipper, and R. G. Compton, Elsevier, Amsterdam, **1985**

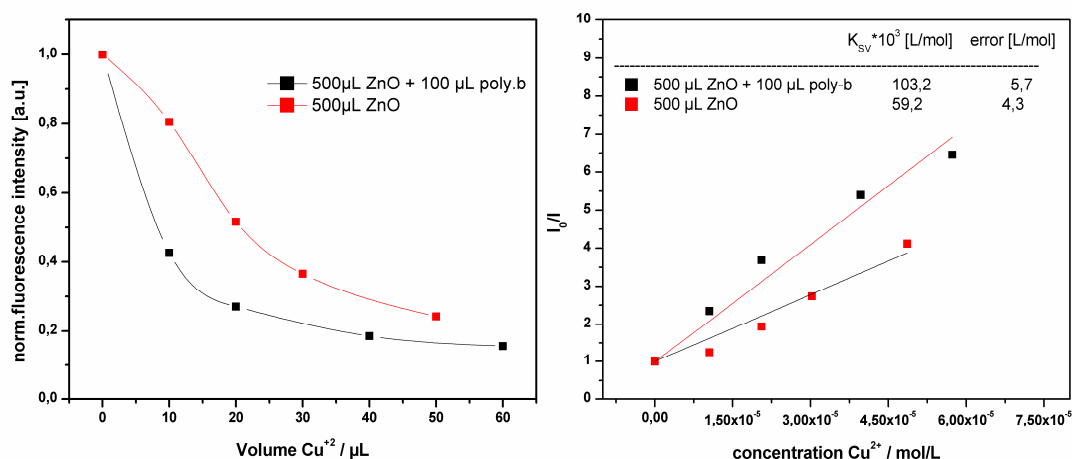


Figure 88. Comparison of the decrease in emission intensity at 512 nm with increasing amount of Cu^{2+} .

This assumption was supported by the following experiments. After the addition of 50 μL of Cu^{2+} solution ($c=0.535$ mg/mL) to both solutions, TMEDA (tetramethylethylenediamine) was added. TMEDA is a well-known complexing agent, suitable for coordination to Cu^{2+} ions. Figure 89 shows that the solution containing ZnO nanoparticles and the polymer poly-b responds with a steep decrease in emission intensity, as discussed previously. The addition of TMEDA results in only a minor signal increase, whereas the solution without the polymer significantly recovers a part of its initial value, by increasing from 16.3% of the initial signal after the addition of copper to 57.5% after 10 μL of TMEDA. A possible reason for the different reversibility of the two systems is that in the case of the solution containing nanoparticles and polymer the copper ions coordinate to the free acid groups on the polymer. So in this case the formation of a TMEDA complex makes a decomplexation from the acid groups necessary. The equilibrium of this reaction depends on the different complex stabilities. On the other hand complexation of copper ions in solution is a process which happens easily and fast, making a recovery of the signal within a small period of time possible.

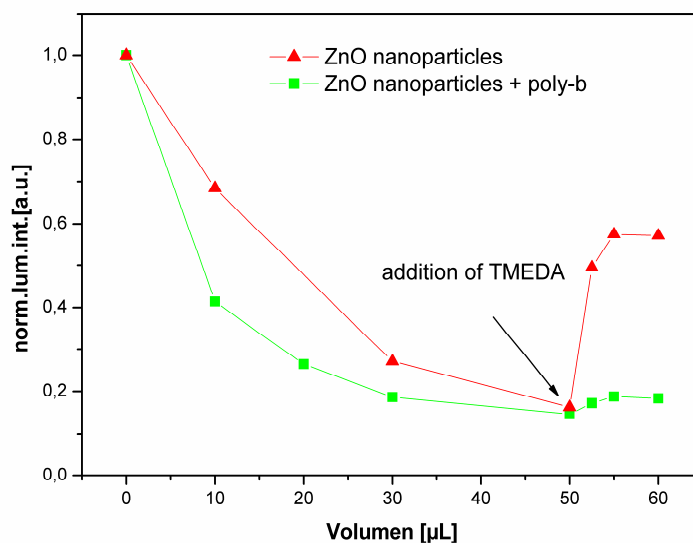


Figure 89. Comparison of emission spectra of a methanol solution of ZnO with and without poly-b and increasing amounts of Cu^{2+} ; $\lambda_{\text{ex}} = 325\text{nm}$; $c(\text{ZnO}) = 0.03\text{ mg/mL}$; $c(\text{poly-b}) = 0.11\text{mg/mL}$.

To get a feeling of the systems sensitivity, in Figure 90 the normalized fluorescence intensity of the ZnO nanoparticles (left y-axis) is again plotted against the volume of copper ions. On the right y-axis the volume of copper ions is correlated with the volume. As can be seen a low content of copper of 3.8 ppm leads to a reduction of 50% of emission intensity. 10% of the emission intensity are lost if 0.5 ppm of copper ions are present in the measuring system. The U.S. Environmental Agency (EPA) has set the limit of copper concentration in drinking water to be 1.3 ppm.^[150] Even this rather low concentration regime is accessible due to the high sensitivity of the investigated system.

¹⁵⁰ Jung, H.S.; Kwon, P.S.; Lee, J.W.; Kim, J.I.; Hong, C.S.; Kim, J.W.; Yan, S.; Lee, J.Y.; Lee, J.H.; Joo, T.; Kim, J.S. *J.Am.Chem.Soc.* **2009**, 131 2008

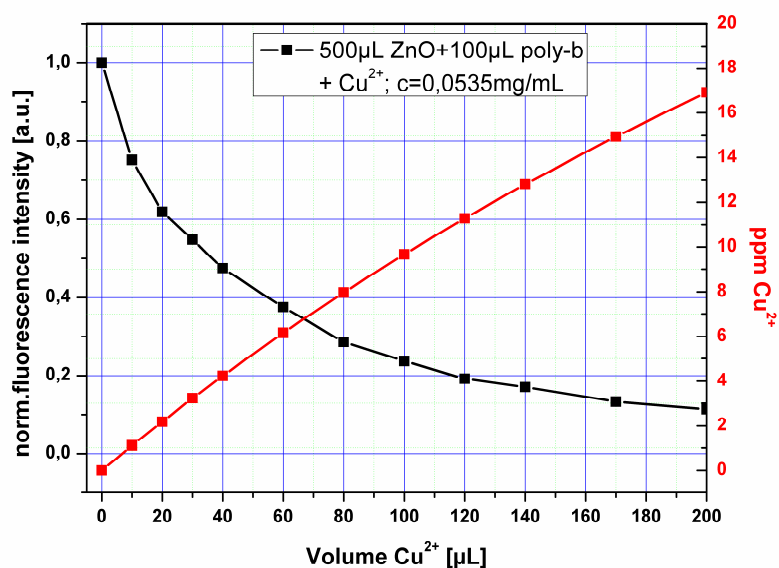


Figure 90. Comparison of the decrease in emission intensity at 512 nm with increasing amount of Cu^{2+} ; $\lambda_{\text{ex}} = 325$ nm.

6.4 Experimental

All chemicals were purchased from Sigma Aldrich in the purest form available and used for syntheses without further purification.

The charged Pt-complex and the block copolymer (poly-b) were prepared according to the literature.^[122,131]

6.4.1 Synthesis of ZnO nanoparticles

Colloidal ZnO nanoparticles were prepared by a modified literature protocol by hydrolyzing zinc acetate dehydrate in basic methanol solution.^[137] In a typical reaction procedure 224.1 mg of KOH (4 mmol; 0.5 eq) were dissolved in 37.5 mL MeOH with stirring at refluxing at 60°C. Meanwhile 438.8 mg of $\text{Zn}(\text{OAc})_2 \cdot 2 \text{H}_2\text{O}$ (2 mmol; 1 eq) were dissolved by stirring in 12.5 mL MeOH. Subsequently, the zinc solution was added into the basic methanol solution. This starting sol was aged for 60 minutes at 60°C. The resulting solution was concentrated by solvent evaporation to about 10% of the initial volume. Through the addition of 25 mL hexane and 5 mL isopropanol the nanoparticles were precipitated. The mixture was kept at 0°C over night to allow full precipitation and settling down of the particles. The supernatant was decanted.^[137] The resulting particles readily redisperse in MeOH. For the XRD characterization the precipitation redispersion procedure was repeated three times. The dynamic light

scattering and optical measurements were made with solutions directly from the reaction mixture after appropriate dilution.

6.4.2 Characterization techniques

Powder-X-ray diffraction (XRD) measurements were performed on a Siemens D-5005 powder-diffractometer (theta-theta geometry, Cu-K α -radiation). The sample was placed on a silicon substrate and applied to a scan rate of 0.036 ° s⁻¹ to record the patterns in the 2 θ range between 10 and 80°. The diameters of the crystallites were estimated according to the broadening of the diffraction peaks using the Scherrer relationship (equation 5).

Particle sizes were determined by dynamic light scattering (DLS) using the Malvern ZetaSizer NanoZS equipped with a 633 nm laser. Measurements were performed at 20°C.^[122]

UV-Visible absorption spectra were recorded on a Cary 50 Bio UV-Visible Spectrophotometer, fluorescence spectra on a Hitachi F-7000 fluorescence spectrometer (www.inula.at) equipped with a red-sensitive photomultiplier R 928 from Hamamatsu (www.hamamatsu.com). The emission spectra were not corrected for the sensitivity of the PMT.^[122]

7 Summary

Chapter 2, 3 and 4 of this work were concerned with the synthesis and characterization of polymers for the use in solar cells. The aim of chapter 2 was the synthesis of block copolymers which enable a better contact of inorganic nanoparticles and conjugated polymers, which is an important issue in hybrid solar cells. Two main strategies, depicted in Figure 91, were followed to achieve this aim. The first made use of the fact that polythiophenes, synthesized by following the GRIM polymerization, can easily be end group modified. Two different end groups, vinyl and allyl, were introduced at the chain end. The idea was to connect the thiophene block via these end groups to a polynorbornene-block, synthesized by ROMP. Unfortunately, both end groups did not yield the desired end products. The use of an oligothiophene with an allyl end group, made an exact analysis of the formed products via MALDI-TOF MS possible.

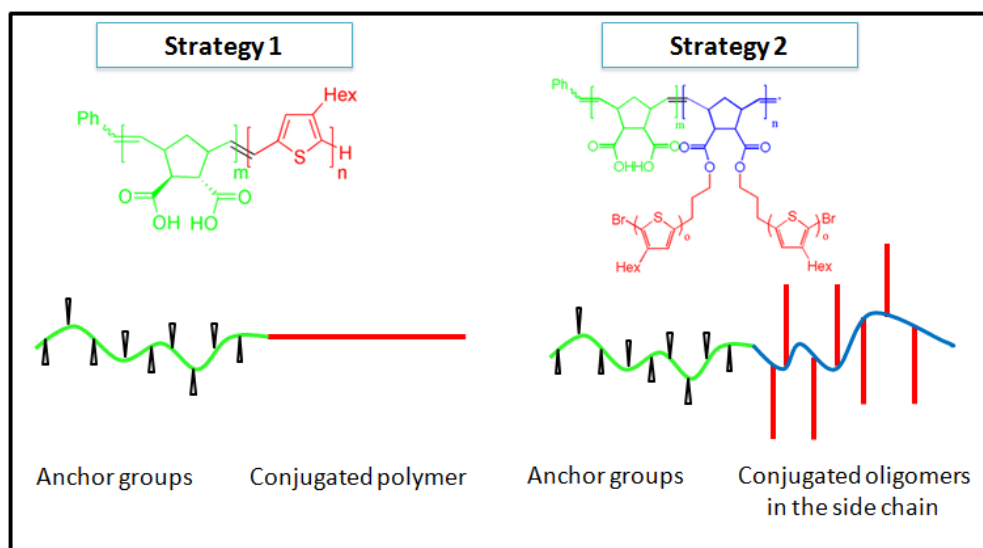


Figure 91. Main strategies for the synthesis of block copolymers for the use in solar cells

By these measurements it was shown that the used Grubbs catalyst of the third generation primary modified the end group of the oligothiophene. Instead of the allyl group an aldehyde functionality or a hydrogen atom was found at the chain end. The aldehyde was probably introduced by an isomerization of the double bond, followed by an oxidation in the presence of oxygen (see Figure 92).

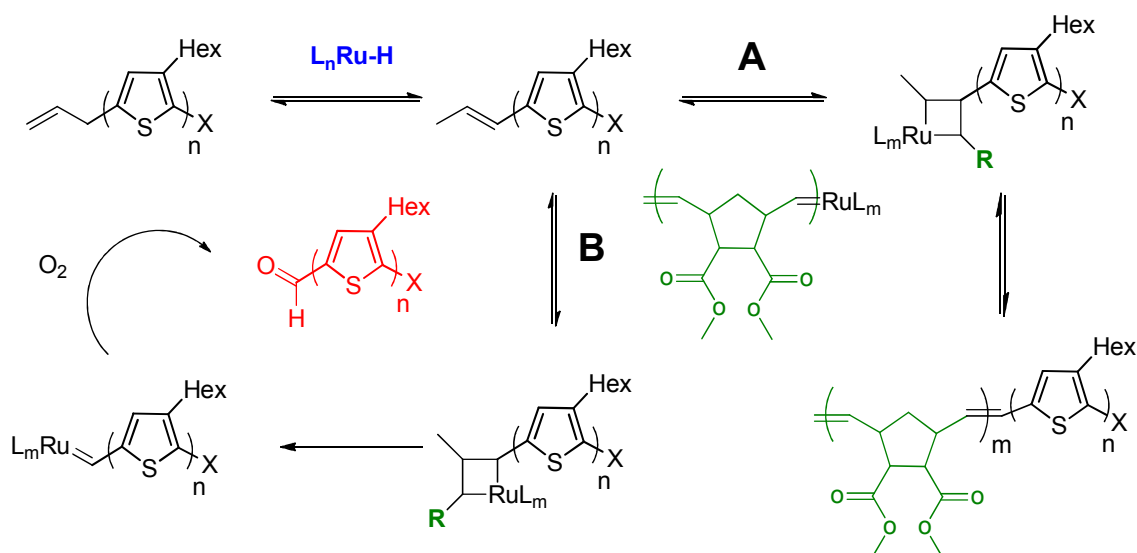


Figure 92. Possible formation mechanism of the aldehyde functionality.

The isomerization probably took place through the interaction of the allylic double bond with a ruthenium-hydride complex, which was formed by a reaction of the Grubbs catalyst with methanol, present in small amounts from the precipitation of the oligothiophene. In the next step an unchanged Grubbs catalyst, located at the chain end of the poly(norbornene) can coordinate to this newly formed double bond. This can happen in two possible orientations, shown in Figure 92 as path A and path B. For a successive block copolymer formation the two polymer chains have to follow path A, meaning that they rearrange in a way which gives rise to high steric demands, making this orientation unfavorable. Following path B, the polymers are oriented in a way that the chains are pointing towards other directions. This favored orientation leads to a binding of the ruthenium initiator to the end group of the polythiophene. The final step of the reaction is the addition of oxygen to the ruthenium-carbon double bond which leads to the final product with aldehyde end groups. This final step was also observed for several occasions in literature reports. However, currently an explanation about the reaction mechanisms resulting in the cleavage of the end group cannot be provided.

As strategy 1 was not able to produce the desired products, strategy 2 was followed consecutively. The synthesis was done by a hydroboration of the allylic end group on an oligothiophene, resulting in an alcohol functionality at the chain-end. The following esterification with *endo, exo*[2.2.1]bicyclo-hept-5-ene-2,3, dicarboxylic acidchloride introduces a polymerizable group, suitable for ring opening metathesis polymerization (ROMP). In the final polymerization step, this monomer was used to build up a

homopolymer, and through the polymerization with *endo*, *exo*[2.2.1]bicyclo-hept-5-ene-2,3-di-tert-butyl-dicarboxylate as comonomer, a block copolymer was synthesized.

The idea behind chapter 3 was to reduce the crystallization tendency of F8T2, an often used conjugated polymer in the fabrication of solar cells. The motivation of this work was based on a literature report by Lim et al. who described the sensitivity of solar cells with F8T2 as the donor phase and PCBM as the acceptor material regarding thermal treatments. They were able to show that annealing temperatures, higher than 70°C favor the formation of quite bulky polymer clusters. As the current density of solar cells is highly dependent on the interface area between the donor and the acceptor material, cells annealed at higher temperatures resulted in devices with comparably low power output. However, for systems where the acceptor phase is formed in-situ, by the decomposition of precursor materials in an annealing step, the reduction of the temperature would result in devices with poor performance. Therefore, the side-chain of the polymer was modified in a way, which reduces the tendency of crystallization. Two strategies were followed, which are depicted schematically in Figure 93.

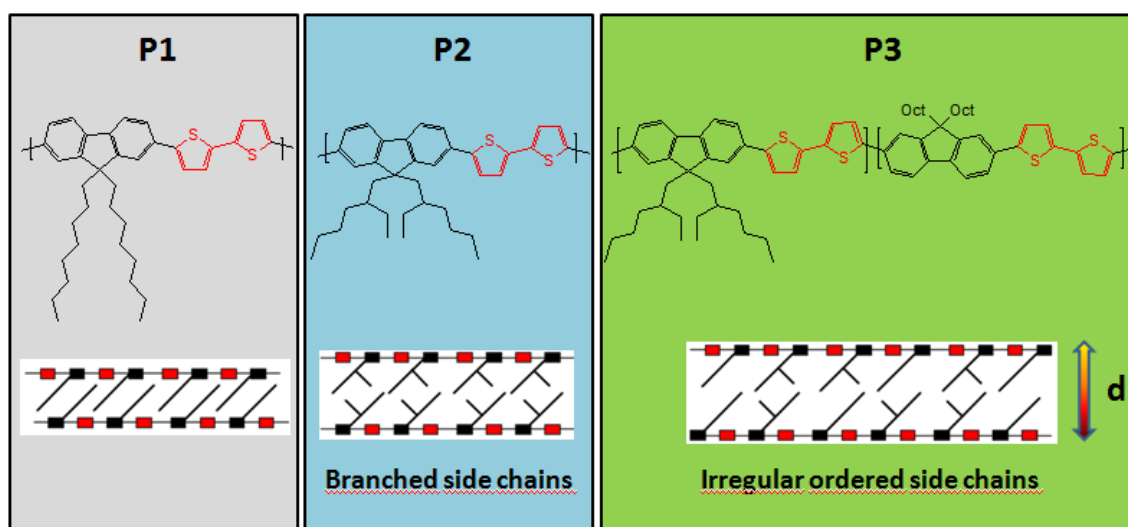


Figure 93. Chemical structures and schematic depiction of the strategies to increase the interplanar distance.

The first makes use of the fact that the introduction of branched alkyl chains leads to an increase of the interplanar distance of neighboring polymer chains, which should result in a more amorphous polymer. The second strategy also increases the interplanar distance, but in this case the regularity of the side chains was disturbed. This was done by using different fluorene units with octyl side-chains in one case and the branched 2-

ethylhexyl side-chains in the other. The statistic incorporation of these two in the main chain should result in a polymer with reduced crystallization tendency. The synthesized polymers were analyzed by ^1H - NMR and GPC measurements. To get informations about the thermal properties DSC measurements were performed. By these measurements it was shown that F8T2 exhibits, in accordance with the literature, liquid crystalline behavior. The polymer undergoes a glass transition at a temperature of 110°C , which is followed by a cold crystallization at a temperature of 159°C . In the higher temperature range two transitions, typical for liquid crystalline polymers can be observed. The first occurs at a temperature of 249°C and can be attributed to a transition from the solid state to the mesophase. The transition to the isotropic phase occurs at a temperature of 323°C .

In contrast, the polymer with the branched side chains only showed a glass transition temperature at 113°C , indicating a highly amorphous polymer. The third polymer, with octyl and 2-ethylhexyl side-chains which were incorporated in a statistic manner in the main chain shows, in addition to the glass transition which occurs at a temperature of 111°C , complex melting behavior in the temperature range between 300°C and 350°C . Two exothermic peaks can be observed. The first one occurs at a temperature of 303°C and the second one, more pronounced than the first, occurs at 347°C . Currently, an explanation concerning this difference cannot be provided. However, the main aim of reducing the crystallization behavior was achieved, shown by the non-existing liquid-crystalline transitions. In addition the tendency of crystallization of conjugated polymers can be investigated by absorption measurements. In general, polymer molecules which tend to agglomerate exhibit absorption spectra which do not differ significantly in solution and in film form. This can be explained by intermolecular π -stacking that already occurs in solution. This is in contrast to polymers with bulky side chains (**P2**) or irregular ordered substituents (**P3**). The absorption spectra of the polymers **P1-P3** are depicted in Figure 94. As expected, the onset of the absorption spectra of the films from polymers **P2** and **P3** is red-shifted compared to their solution spectra, which indicates the π -stacking which only occurs in the films. Compared to these polymers, the onset of polymer **P1** remains unchanged.

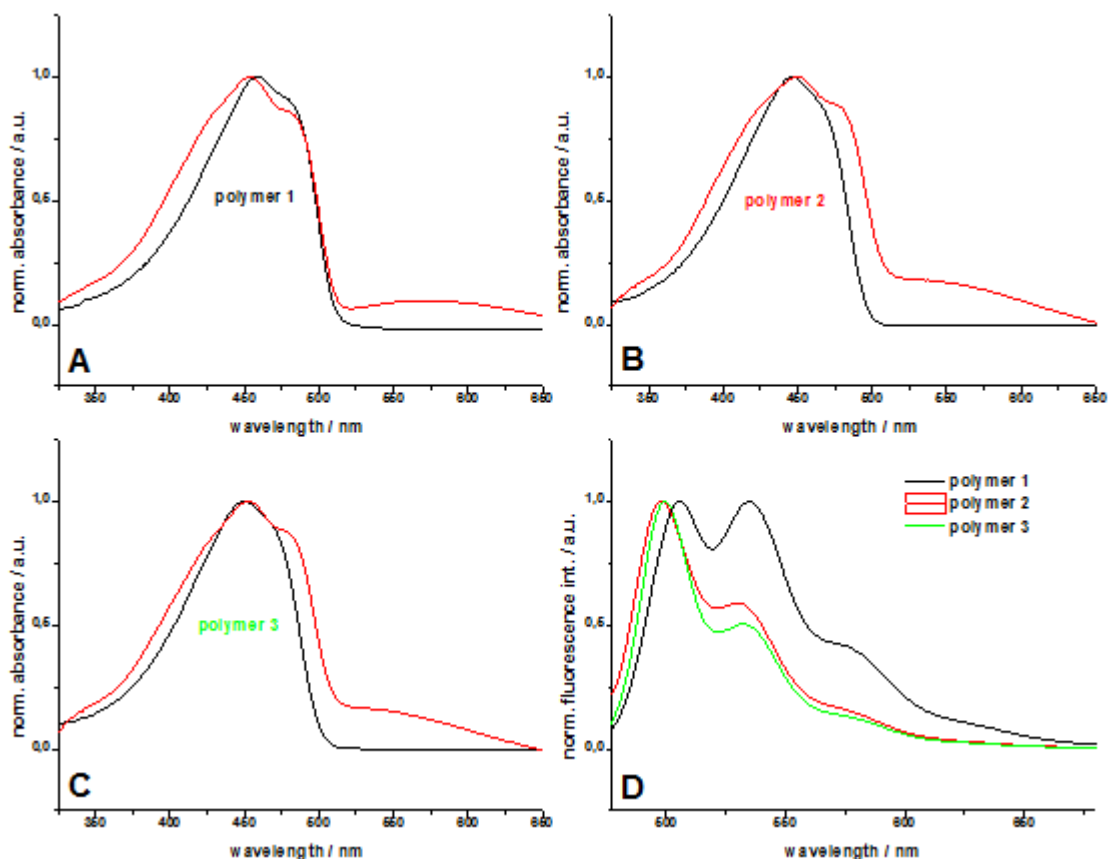


Figure 94. Summary of absorption spectra in chloroform solution ($c = 0.008$ mg/mL; black lines) and of films cast from chloroform solution ($c = 7$ mg/mL; red lines) of **P1** (A), **P2** (B) and **P3** (C); D: emission spectra of the polymers in chloroform solutions ($c = 0.004$ mg/mL; $\lambda_{\text{ex}} = 450$ nm).

So both methods confirm the success of the two different strategies to decrease the crystallization tendency.

In chapter 4 another important topic concerning polymers for organic solar cells was discussed, namely the purity of the materials. Solar cells with F8T2/PCBM as the active layer were fabricated as schematically shown in Figure 95. The polymer, F8T2, was synthesized by Suzuki-polycondensation using $\text{Pd}[\text{P}(\text{Ph})_3]_4$ as the catalyst. It was already known from literature that palladium residues are present in the resulting polymers. The amounts differ greatly, depending on the used work-up procedures. Following the standard procedure from literature F8T2 with a palladium content of 1200 ppm (**P4**) was synthesized. A certain fraction of this polymer was treated with *N,N,N'*-trimethylethane-1,2-diamine, immobilized on polystyrene. This compound is a commercial available metal scavenger which reduced the palladium content to 400 ppm

(P5). These two polymers, together with a commercial one from Sigma Aldrich, with 5600 ppm palladium (P6), were used for the fabrication of solar cells with the intention to study the influence of the palladium content on the performance of the cells.

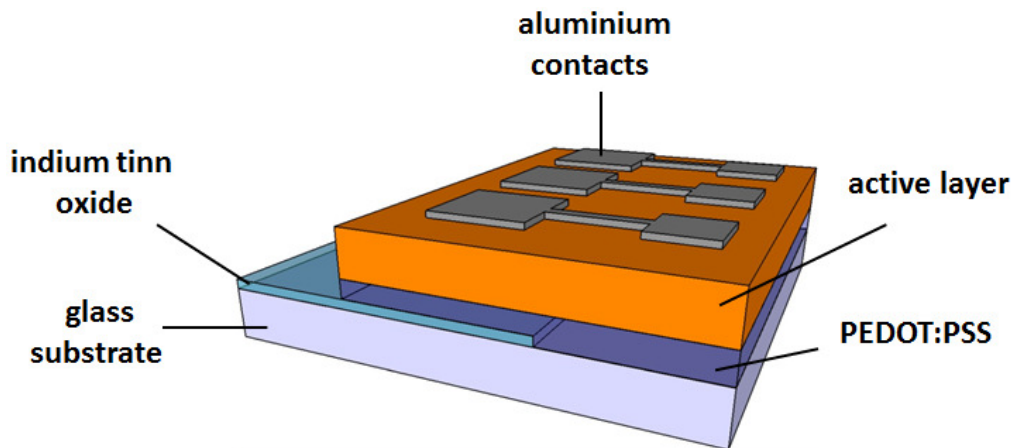


Figure 95. Scheme of the prepared hybrid solar cells.

It was already known from literature that the presence of impurities leads to a reduction of the V_{OC} in solar cells, because these can act as trap states, meaning that energy levels below the LUMO level of the acceptor are formed, which reduce the effective band gap. Moreover, also the current density is negatively influenced by these traps, because competing recombination processes get more probably.

For the three investigated polymers the trend of reduced V_{OC} with increasing palladium content was confirmed. However, regarding the current density a serious comparison can only be made between P4 and P5 due to the fact that this parameter is also strongly influenced by the molecular weight of the polymers which gives rise to different morphology of the films. As P4 and P5 have the same molecular weight with about 56.000 g/mol and P6 is with 20.000 g/mol significant shorter, it has to be discussed separately. It was shown that P6, on average, was the polymer with the highest current densities, probably owing to a different morphology in the film. However, the comparison between P4 and P5 confirmed the expected trend of decreasing current densities with increasing palladium content. In addition, measurements of the V_{OC} , at different illumination intensity, were performed. In principle, by plotting the open circuit voltage on the y-axis and the light intensity on the x-axis, information about the trap density in the investigated solar cells is provided by the slope of the lines. In accordance with the theory it was shown that increasing the palladium content leads to more trap states.

Chapter 5 deals with the synthesis and characterization of CuInS₂ nanoparticles, which are a promising material for the use in hybrid solar cells. Strong emphasis was placed on a comparison of the classical oilbath heating method with microwave assisted heating of the reaction solution. Based on the versatility, the oleylamine route was chosen for the synthesis with CuI, InCl₃ and elemental sulfur as the sulfur source.

The formation of CuInS₂ nanoparticles using the oleylamine route already starts at quite low temperatures of 115 to 120 °C. This temperature range is far below commonly applied reaction temperatures. Both a microwave and an oil bath heating method lead at a temperature of 120 °C to small particles (approx. 2 to 3 nm) with irregular shape and broad size distribution. By applying higher temperatures, these quality criterions can be improved. Using microwave irradiation it is possible to obtain nanoparticles of 3 to 4 nm with a reaction time of only 90 s. Although preliminary comparison experiments between microwave and conventional heating under apparently "similar" conditions performed at 120 °C and 220 °C have provided slightly different results in the obtained CuInS₂ nanoparticles, carefully executed control experiments ensuring identical heating and cooling profiles, stirring rates and reactor geometries clearly demonstrate that for the preparation of CuInS₂ nanoparticles described herein no differences between conventional and microwave heating could be observed. The nanoparticles obtained by the three control experiments have the same crystal phase, primary crystallite size, shape and size distribution and show no significant differences in absorption behavior.

In chapter 6 the interaction of ZnO nanoparticles with a platinum dye (Figure 96 (left)) mediated by the presence of an amphiphilic block copolymer (Figure 96 (right)), poly-[*endo,exo*[2.2.1]bicyclo-hept-5-ene-2,3-dicarboxylic acid dimethylester)-*b*-(*endo,exo*[2.2.1]bicyclo-hept-5-ene-2,3-dicarboxylic acid) was investigated. The acid block is able to coordinate to the nanoparticles as well as to the Pt complex. The Pt-dye shows an intense luminescence peaking at 650 nm in the solid state due to aggregation and the formation of Pt-Pt interactions, whereas in solution it is not luminescent. However, adding the block copolymer to the dye solution gives rise to the typical Pt luminescence. This is due to the coordination of the cationic complex to the acid groups on the polymer resulting in close proximity of the dyes. The absorption peak of this dye/polymer mixture fits the emission of ZnO nanoparticles, so that an energy transfer would be possible. Indeed, an increase of about 300% in the emission intensity of the Pt-complex can be seen after nanoparticle addition.

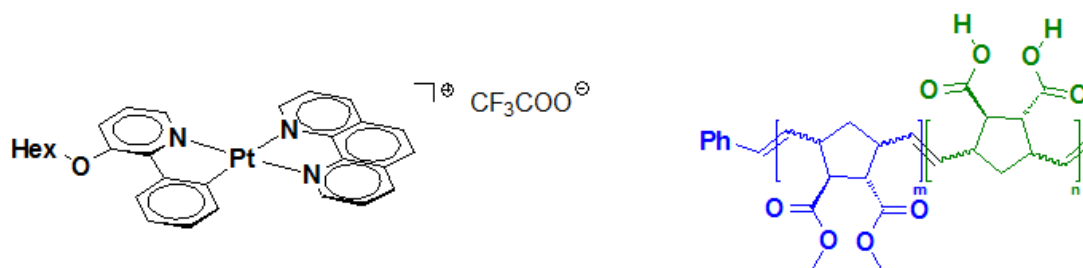


Figure 96. Chemical structures of the platinum dye (left) and the amphiphilic block copolymer (right)

A complete model, describing the overall process was worked out and confirmed by different experiments, including optical measurements and DLS investigations. Moreover, factors which determine the efficiency of the process were evaluated. In the second part of chapter 6 this material combination was used as sensing system for the detection of Cu^{2+} ions. Although the sensitivity of the system would be sufficient, the selectivity is quite poor based on the competing replacement of platinum dyes, coordinated to the acid block, by the analyte ions. However, the superior performance in the sensing of Cu^{2+} ions of an alternative system, consisting of ZnO nanoparticles, coordinated to the block copolymer (poly-b), was demonstrated. Even a rather low copper content of 0.5 ppm can be detected by the investigated system.

8 Summary

8.1 List of Tables

Table 1. Chemical shift of the possible coupling products in polythiophenes with chloroform as solvent.....	39
Table 2. GPC results of P1 and P2 with THF as solvent.....	43
Table 3. GPC results of P3 and BC1-BC3	46
Table 4. Comparison of front orbitals and band gaps of poly(9,9-dioctylfluorenes), F8T2 and F8TT.	66
Table 5. GPC data of the polymers P1-P3 in THF as solvent.	71
Table 6. Summary of the absorption and emission data of the polymers P1-P3	75
Table 7. Pd-content of the polymers P4-P6	82
Table 8. Solar cell parameters.	84
Table 9. Solar cell parameters of cells with PEDOT/PSS intermediate layer.	84
Table 10. Comparison of solar cell parameters for the different polymers.	85
Table 11. Obtained slopes from the measurements.	88
Table 12. Dynamic light scattering measurements of poly-b in MeOH; c=0.12 mg/mL.	121

8.2 List of Figures

Figure 1. Overview of the world energy demand and prediction for the future. ^[1]	11
Figure 2. Principle processes involved in the generation of photocurrent. ^[5] (red blocks: D is the donor material, A is the acceptor material)	13
Figure 3. Photon flux of the sun (AM 1.5) as a function of the wavelength. The integrated photon flux is shown on the right y-axis together with the maximum obtainable current densities. ^[1]	14
Figure 4. Schematic illustration of bulk heterojunction (showing a gradient) and bilayer architecture.....	16
Figure 5. Current – voltage characteristic of a solar cell. ^[5]	17
Figure 6. Energy diagram of a donor and acceptor material and the corresponding parameters.....	18

Figure 7. Equivalent circuit of a solar cell. ^[16]	19
Figure 8. Kinetic considerations during the growth of nanoparticles. ^[1]	22
Figure 9. Polymers with increased planarization. ^[23,24,25]	25
Figure 10. Chemical structure of PEDOT.....	25
Figure 11. Strategy 1 for the coupling of nanoparticles to a conductive block.	29
Figure 12. Strategy 2 for the coupling of nanoparticles to a conductive block.	30
Figure 13. Possible coupling products of substituted thiophene.....	31
Figure 14. Possible products from the reaction of a with the Grignard reagent.....	33
Figure 15. Mechanism of the polymerization.	34
Figure 16. Schematic reaction scheme of the end group-functionalization.....	35
Figure 17. Synthesis of P3AT according to McCullough.....	36
Figure 18. Synthesis of P3HT according to Rieke.....	37
Figure 19. Reaction scheme of the bromination of 3-hexylthiophene.....	38
Figure 20. Reaction scheme of the polymerization.	38
Figure 21. ¹ H NMR of poly(3-hexylthiophene).....	40
Figure 22. MALDI-TOF results from P2 (left) and P1 (right).....	41
Figure 23. Possible reactions leading to the observed side products.	42
Figure 24. Reaction scheme for the synthesis of the block copolymers BC1-BC3	45
Figure 25. Reaction scheme for the synthesis of the block copolymers BC4-BC6	46
Figure 26. ¹ H - NMR spectrum of P4	47
Figure 27. MALDI-TOF MS measurement of BC6	48
Figure 28. Reaction products.	48
Figure 29. Possible formation mechanism of the aldehyde functionality.....	49
Figure 30. Synthesis of comblike block copolymers.	51
Figure 31. MS results of P5	52
Figure 32. FTIR spectra of P5 , P6 and 5	53
Figure 33. Comparison of characteristic regions from BC7 and BC8	54
Figure 34. Absorption and emission spectra of BC7 and BC8	55
Figure 35. Chemical structures of F8T2 and F8TT.	65
Figure 36. Interaction of front orbitals in donor-acceptor systems.....	66
Figure 37. Chemical structures and schematic illustration of the strategies to increase the interplanar distance.	68
Figure 38. Schematic representation of the catalytic cycle involved in Suzuki-type reactions.	69

Figure 39. Synthesis scheme for polymers P1 and P2	69
Figure 40. Synthesis scheme for polymer P3	70
Figure 41. DSC curve of P1	72
Figure 42. DSC curve of P2	72
Figure 43. DSC curve of P3	73
Figure 44. Summary of absorption spectra in chloroform solution ($c = 0.008$ mg/mL; black lines) and of films cast from chloroform solution ($c = 7$ mg/mL; red lines) of P1 (A), P2 (B) and P3 (C); D: emission spectra of the polymers in chloroform solutions ($c = 0.004$ mg/mL; $\lambda_{\text{ex}} = 450$ nm).	74
Figure 45. Schematic summary of the processes, involved in the formation of free charge carriers.....	79
Figure 46. Schematic illustration of the palladium scavenger.....	81
Figure 47. Schematic illustration of the prepared hybrid solar cells.	82
Figure 48. Overview of the used materials.	83
Figure 49. Plots of light intensity versus open circuit voltage of the polymers P4 (red), P5 (green) and P6 (black) together with the corresponding linear fits (black lines).....	87
Figure 50. Wide angle X-ray scattering curves and corresponding Lorentz fits at selected temperatures (A) and primary crystallite size and temperature versus reaction time (B).	95
Figure 51. XRD-patterns of particles prepared at 120°C after different heating times (curves are shifted vertically for better visibility). The peaks are in good agreement with the reference file for chalcopyrite type CuInS_2 (ICSD – 42127– sharp lines at the bottom).....	96
Figure 52. TEM image of CuInS_2 nanoparticles (A) prepared at 120 °C using conventional heating for 20 h and (B) microwave irradiation for 60 min.	97
Figure 53. Heating profile of the microwave experiments at 120 °C and at 220 °C.	98
Figure 54. XRD patterns of CuInS_2 nanoparticles prepared using microwave heating at 120°C times (curves are shifted vertically for better visibility).....	99
Figure 55 XRD-patterns of particles prepared at 220°C after different heating times (curves are shifted vertically for better visibility).	100
Figure 56. TEM image of CuInS_2 particles prepared at 220°C using oil bath for 15 min.	100
Figure 57. XRD patterns of the particles prepared using microwave heating at 220°C (curves are shifted vertically for better visibility).	101

- Figure 58.** TEM images of the CuInS₂ nanoparticle samples prepared at 220°C using microwave irradiation: (A) 90 s, (B) 15 min, and (C) 60 min experiment. 102
- Figure 59.** Heating profiles of the control experiments (A), XRD-patterns of the experiments obtained after 900 s (15 min) overall reaction time (B). 104
- Figure 60.** Comparison of TEM images and SAED pattern (insert) of the CuInS₂ nanoparticles synthesized at 220 °C of the (A) MW-Pyrex, (B) MW-SiC, (C) Oilbath experiments. 104
- Figure 61.** UV-Vis spectra of the CuInS₂ samples synthesized at 220 °C. 105
- Figure 62.** TGA experiments of the CuInS₂ samples synthesized at 220 °C. 106
- Figure 63.** emission spectra of the samples in chloroform solution; c = 0.05 mg/mL. 106
- Figure 64.** Synthesis of the charged platinum complex (**2**). 113
- Figure 65.** XRD pattern of ZnO nanoparticles with corresponding miller indices. 116
- Figure 66.** Dynamic light scattering results of ZnO nanoparticles in MeOH. 116
- Figure 67.** Absorption spectrum of a methanol solution of the platinum dye (c = 1.375*10⁻⁶ mol/L). 117
- Figure 68.** Comparison of absorption of a methanol solution of the pure platinum complex and in a mixture with the block copolymer, poly-b. 118
- Figure 69.** Comparison of emission spectra of a methanol solution of the pure platinum complex and in a mixture with the block copolymer; λ_{ex} = 366 nm. 119
- Figure 70.** Comparison of emission spectra of a methanol solution of the block-copolymer with increasing amounts of platinum; λ_{ex} = 535 nm. 120
- Figure 71.** Increase of emission intensity at 650 nm with increasing amount of platinum. 121
- Figure 72.** Absorption and emission from a ZnO nanoparticle solution in MeOH; c = 0.03 mg/mL. 122
- Figure 73.** Changes in nanoparticle emission behavior upon the addition of poly-b; λ_{ex} = 332 nm; c(poly-b): 0.1 mg/mL; c(ZnO) = 0.03 mg/mL. 123
- Figure 74.** Comparison of absorption and emission spectra of ZnO (λ_{ex} = 325 nm) and Pt-poly-b (λ_{ex} = 366 nm). 124
- Figure 75.** Comparison of emission spectra of a methanol solution of Pt-poly-b with increasing amounts of ZnO; λ_{ex} = 325 nm; see inset for concentrations. 125
- Figure 76.** Increase of emission intensity at 636 nm with increasing amount of ZnO. 125

Figure 77. Comparison of emission spectra of a methanol solution of block copolymer and ZnO with increasing amounts of platinum; $\lambda_{\text{ex}} = 325 \text{ nm}$; $c(\text{Pt})$: 0.22 mg/mL; $c(\text{poly-b})$: 0.1 mg/mL; $c(\text{ZnO}) = 0.03 \text{ mg/mL}$	127
Figure 78. Emission intensity decrease of ZnO nanoparticles by dilution and quenching.	129
Figure 79. Plot of intensity ratio versus concentration of the platinum-dye.....	130
Figure 80. Comparison of absorption and emission spectra of ZnO ($\lambda_{\text{ex}} = 325 \text{ nm}$) and Pt-complex.	131
Figure 81. Influence of the increase of excimer emission intensity at 635 nm on the polymer concentration; $\lambda_{\text{ex}} = 325 \text{ nm}$, $c(\text{Pt}) = 0.15 \text{ mg/mL}$, $c(\text{ZnO}) = 0.06 \text{ mg/mL}$	132
Figure 82. Absolute emission intensity (black curve) and standard deviation (red curve) as a function of the polymer concentration; $\lambda_{\text{ex}} = 325 \text{ nm}$, $c(\text{Pt}) = 0.15 \text{ mg/mL}$, $c(\text{ZnO}) = 0.06 \text{ mg/mL}$	133
Figure 83. DLS experiments of the titration of poly-b with KOH and ZnO nanoparticles.	134
Figure 84. Signal increase of excimer emission upon the addition of KOH.	135
Figure 85. Comparison of emission spectra of a methanol solution of the Pt-poly-b with increasing amounts of Cu^{2+} (0.535mg/mL); $\lambda_{\text{ex}} = 366\text{nm}$, $c(\text{poly-b}) = 0.11\text{mg/mL}$, $c(\text{Pt}) = 0.165\text{mg/mL}$	137
Figure 86. Comparison of emission spectra of a methanol solution of ZnO with increasing amounts of Cu^{2+} ; $\lambda_{\text{ex}} = 325\text{nm}$, $c(\text{ZnO}) = 0.03 \text{ mg/mL}$	138
Figure 87. Comparison of emission spectra of a methanol solution of ZnO with poly-b and increasing amounts of Cu^{2+} ; $\lambda_{\text{ex}} = 325\text{nm}$; $c(\text{ZnO}) = 0.03 \text{ mg/mL}$; $c(\text{poly-b}) = 0.11\text{mg/mL}$	139
Figure 88. Comparison of the decrease in emission intensity at 512 nm with increasing amount of Cu^{2+}	140
Figure 89. Comparison of emission spectra of a methanol solution of ZnO with and without poly-b and increasing amounts of Cu^{2+} ; $\lambda_{\text{ex}} = 325\text{nm}$; $c(\text{ZnO}) = 0.03 \text{ mg/mL}$; $c(\text{poly-b}) = 0.11\text{mg/mL}$	141
Figure 90. Comparison of the decrease in emission intensity at 512 nm with increasing amount of Cu^{2+} ; $\lambda_{\text{ex}} = 325 \text{ nm}$	142
Figure 91. Main strategies for the synthesis of block copolymers for the use in solar cells	144
Figure 92. Possible formation mechanism of the aldehyde functionality.....	145

Figure 93. Chemical structures and schematic depiction of the strategies to increase the interplanar distance.	146
Figure 94. Summary of absorption spectra in chloroform solution ($c = 0.008$ mg/mL; black lines) and of films cast from chloroform solution ($c = 7$ mg/mL; red lines) of P1 (A), P2 (B) and P3 (C); D: emission spectra of the polymers in chloroform solutions ($c = 0.004$ mg/mL; $\lambda_{\text{ex}} = 450$ nm).	148
Figure 95. Scheme of the prepared hybrid solar cells.....	149
Figure 96. Chemical structures of the platinum dye (left) and the amphiphilic block copolymer (right)	151

8.3 *List of Publications*

Papers

2011

Investigation of the Formation of CuInS₂ Nanoparticles by the Oleylamine Route: Comparison of Microwave-Assisted and Conventional Syntheses - Pein, A.; Baghbanzadeh, M.; Rath, T.; Haas, W.; Maier, E.; Amenitsch, H.; Hofer, F.; Kappe, O.; Trimmel, G.; *Inorganic chemistry*, 2011, 50 1, 193 – 200.

Synthesis and characterization of alternating fluorene-thiophene copolymers bearing ethylene glycol side-chains – Ziegler, E.; Pein, A.; Fischereeder, A., Trimmel, G.; *Monatshefte für Chemie = Chemical monthly*, 2011, 142, 193.

The Stoichiometry of Single Nanoparticles of Copper Zinc Tin Selenide - Haas, W.; Rath, T.; Pein, A.; Rattenberger, J.; Trimmel, G.; Hofer, F.; *Chemical communications*, 2011, 47, 2050-2052.

2007

Europium-containing polymers as humidity-sensing materials - Knall, A.-C.; Pein, A.; Noormofidi, N.; Stelzer, F.; Slugovc, C. ; *Polymer preprints* 2007, 48 , 575 – 576.

Oral Presentations

2009

Hybrid Photovoltaic Cells via a Novel Direct Route - Maier, E.; Edler, M.; Fischereeder, A.; Fradler, C.; Haas, W.; Hofer, F.; Larissegger, S.; Mauthner, G.; Meischler, D.; Pein, A.; Rath, T.; Saf, R.; Santis Alvarez, A.; Trattnig, R.; Stelzer, F.; List, E.; Trimmel, G.; *NAWI Graz Workshop* 2009.

2008

Energy transfer from ZnO nanoparticles to a platinum dye mediated by a block copolymer - Pein, A.; Niedermair, F.; Stubenrauch, K.; Slugovc, C.; Trimmel, G.; *Nanomaterials. Playa del Carmen*, 2008.

Preparation, Characterization and Applications of Europium-Containing Copolymers - Knall, A.-C.; Pein, A.; Noormofidi, N.; Tscherner, M.; Stelzer, F.; Slugovc, C.; .1st Joint Austrian & Slovenian Polymer Meeting ASPM 2008 and 9th Austrian Polymer Meeting, 2008.

ROM-polymerizable Europium complexes and their application in sensing layers - Knall, A.-C.; Pein, A.; Noormofidi, N.; Tscherner, M.; Stelzer, F.; Slugovc, C.; 5. WACÖ (5. Workshop Anorganische Chemie in Österreich), 2008.

2007

Europium-containing polymers as humidity-sensing materials - Knall, A.-C.; Pein, A.; Noormofidi, N.; Stelzer, F.; Slugovc, C.; American Chemical Society, 234rd National Meeting & Exposition, Boston, 2007.

Posters

2009

Energy Transfer from ZnO Nanoparticles to a Platinum Dye Mediated by the Presence of a Block copolymer - Pein, A.; Niedermair, F.; Stubenrauch, K.; Slugovc, C.; Trimmel, G.; European Polymer Congress 2009 (EPF09), Graz, 2009.

End group-functionalization of Poly(3-alkylthiophene)s - Ziegler, E. E.; Pein, A.; Saf, R.; Trimmel, G.; European Polymer Congress 2009 (EPF09), Graz, 2009.

Organic-inorganic semiconductor blends for photovoltaic applications - Rath, T.; Maier, E.; Edler, M.; Fischereeder, A.; Larissegger, S.; Pein, A.; Haas, W.; Mauthner, G.; Hofer, F.; List, E.; Trimmel, G.; Nano and Photonics 2009, Mauterndorf, 2009.

Organic-inorganic semiconductor blends for photovoltaic applications - Larissegger, S.; Rath, T.; Maier, E.; Edler, M.; Fischereeder, A.; Pein, A.; Haas, W.; Hofer, F.; List, E.; Trimmel, G.; Mauthner, G.; 24th European Photovoltaic Solar Energy Conference, Hamburg, 2009.

2008

Lifetime-Based Optical Humidity Measurements Using Europium-Containing Materials - Knall, A.-C.; Pein, A.; Noormofidi, N.; Tscherner, M.; Konrad, C.; Ribitsch, V.; Uray, G.; Stelzer, F.; Slugovc, C.; Eurotrode IX, Dublin, 2008.

Synthesis and Characterization of comblike block – copolymers containing oligothiophenes in the side chain - Pein, A.; Saf, R.; Trimmel, G.; Fpi8, Graz, 2008.

Electroactive organic materials and hybrid materials for photovoltaic applications - Maier, E.; Trimmel, G.; Rath, T.; Pein, A.; Kremser, G.; Saf, R.; Stelzer, F.; International Symposium TOWARDS ORGANIC PHOTOVOLTAICS, Linz, 2008.

Synthesis and Characterization of ZnO-Nanoparticles and their interaction with a platinum dye mediated by a block copolymer - Pein, A.; Kremser, G.; Niedermair, F.; Wappel, J.; Slugovc, C.; Trimmel, G.; Particles 2008, Orlando, 2008.

Luminescent Metal Complexes as Building Blocks for Ring Opening Metathesis Polymerisation - Noormofidi, N.; Pein, A.; Knall, A.-C.; Slugovc, C.; Zing, Organometallics at the Centre, Cancun, 2008.

Synthesis and Characterization of block copolymers containing poly(thiophene) and poly(norbornene) blocks - Pein, A.; Saf, R.; Trimmel, G.; 1st Joint Austrian & Slovenian Polymer Meeting ASPM 2008, Graz, 2008.

2007

ROM Polymers as Scaffold for Phosphorescent Transition Metal Complexes - Noormofidi, N.; Pein, A.; Knall, A.-C.; Slugovc, C.; EPF 2007 European Polymer Congress, Portoroz, 2007.

Polymerisable Phosphorescent Transition Metal Complexes - Noormofidi, N.; Pein, A.; Knall, A.-C.; Slugovc, C.; 10th Conference on Methods and Applications of Fluorescence, Salzburg, 2007.

Optical humidity sensor materials based on europium - Knall, A.-C.; Pein, A.; Noormofidi, N.; Tscherner, M.; Konrad, C.; Ribitsch, V.; Uray, G.; Stelzer, F.; Slugovc, C.; 10th Conference on Methods and Applications of Fluorescence. Salzburg, 2007.

Phosphorescent Transition Metal Complexes as Building Blocks for Ring Opening Metathesis Polymerisation - Noormofidi, N.; Pein, A.; Knall, A.-C.; Slugovc, C.; 3rd STIPOMAT Workshop. Les Diablerets, 2007.

2006

Polymeric Europium Complexes – Synthetic Approach by Using 1,3,5-Triazin Based Ligands - Pein, A.; Slugovc, C.; 8th Austrian Polymer Meeting. Linz, 2006.

8.4 *Curriculum Vitae*

Personal Details

Name	Andreas Pein
Address	Perlsdorf 95a 8341 Paldau
Mail	pein@tugraz.at
Date of birth	12.01.1980
Citizenship	Austria

Education and Qualifications

1986 – 1990	Elementary school in St.Stefan im Rosental
1990 – 1998	Secondary school in BG/BRG Kirchengasse, Graz
1998 – 1999	Military service in Leibnitz, St.Michael and Feldbach
1999 – 2007	Graz University of Technology – Technical Chemistry June 2007: diploma examination with excellent success Diploma thesis: “Synthesis and characterization of a photoluminescent, polymerisable europium complex”
2007 – 2011	PhD thesis at Graz University of Technology; PhD supervisor: Assoc. Prof. DI Dr. Gregor Trimmel PhD thesis: “Synthesis and characterization of materials for optoelectronic devices”